SOLAR FLARE SOFT X-RAY IRRADIANCE AND ITS IMPACT ON THE EARTH'S UPPER ATMOSPHERE

A

DISSERTATION

Presented to the Faculty

of the University of Alaska Fairbanks

in Partial Fulfillment of the Requirements

for the Degree of

DOCTOR OF PHILOSOPHY

By

Erica M. Rodgers, B.S., M.S.

Fairbanks, Alaska

December 2007

SOLAR FLARE SOFT X-RAY IRRADIANCE AND

ITS IMPACT ON THE EARTH'S UPPER ATMOSPHERE

By

Erica M. Rodgers

RECOMMENDED:

Advisory Committee Chair

Chair, Department of Physics

APPROVED:

Dean, College of Natural Science and Mathematics

Dean of the Graduate School

Nov 9, 2007

Date

Abstract

Solar flares dramatically enhance the soft X-ray region of the solar spectrum. The enhancement is more significant than previously thought, and the solar soft X-ray instruments aboard the Thermosphere Ionosphere Mesosphere Energetics Dynamics (TIMED) and Solar Radiation and Climate Experiment (SORCE) satellites have observed more flares than expected. This dissertation presents a state-of-the-art analysis used to determine flare spectra from TIMED and SORCE solar observations. A relationship is established between Geostationary Operational Environmental Satellite (GOES) flare 0.1-0.8 nm irradiances and XPS flare 0.1-2 and 0.1-7 nm irradiances. Solar flares primarily enhance the soft X-ray irradiance in the 0.1-2 nm range, and rapidly modify the energy input to the lower thermosphere. Most of the excess flare 0.1-2 nm irradiance comes from 1-2 nm. Thus, flares deposit a large amount of their energy between 100-110 km. One of the key effects of this energy deposition is to modify nitric oxide (NO), which plays an important role in the energy balance of the thermosphere as it is a source of radiative cooling through infrared emissions. The density of NO is highly variable as a function of time and latitude, and reaches a maximum in the same altitude region where the flare irradiance is absorbed. This dissertation also presents valid comparisons between Student Nitric Oxide Explorer (SNOE) satellite NO observations and those predicted by a photochemical thermospheric model to provide a better understanding of low latitude flare enhanced NO column density. Large flares can deposit the same amount of 0.1-2 and 0.1-7 nm energy to the thermosphere during a relatively short time as the Sun normally deposits in one day. The NO column density doubles as the daily integrated energy to the thermosphere doubles.

Table of Contents

Page

Page

Page

List of Figures

Page

Page

Page

Page

List of Tables

Page

Dedication

For Mark

Chapter 1 Introduction

A quantitative understanding of the energy deposited from solar flares into the Earth's upper atmosphere is required to determine their terrestrial impacts. A method to determine solar flare spectra is described in this dissertation. These spectra were used to determine the soft X-ray energy input to the thermosphere during a flare. Of particular importance is that the energy from solar flare enhanced soft X-ray irradiance is absorbed in the same upper atmosphere altitude region where peak nitric oxide (NO) production occurs. This dissertation describes the impact of solar flares on the density of NO in the thermosphere and answers two questions: 1) What is the solar soft X-ray energy deposition into Earth's lower thermosphere during a solar flare and how does it vary as a function of altitude; and 2) What is the effect of this energy input on the NO density in the Earth's lower thermosphere? The first research question is answered through the analysis of solar observations using instruments aboard the Thermosphere Ionosphere Mesosphere Energetics Dynamics (TIMED) and Solar Radiation and Climate Experiment (SORCE) satellites. The second research question is answered through the analysis of thermospheric NO observations from an instrument aboard the Student Nitric Oxide Explorer (SNOE) satellite.

Chapter 1 provides a discussion of the Sun and its energy output, particularly soft X-ray irradiance and solar flares, and the impact of soft X-rays on the Earth's upper atmosphere, particularly thermospheric NO. Chapter 2 describes the TIMED and SORCE solar observing instruments, their calibrations, and their observations of solar flares. Chapter 3 describes the solar flare spectral analysis, including a model and retrieved solar flare spectra. Chapter 4 describes SNOE NO density observations of a solar flare, predicted NO density of the flare from a photochemical model and analysis of other flares observed by SNOE. Chapter 5 concludes this dissertation with a summary of results and applications for future research.

1.1. Solar Interior

The Sun is a large mass of plasma that formed 4.5 billion years ago. It is composed mostly of hydrogen and helium, and provides approximately 1366 Wm^{-2} of radiant flux

at the Earth through nuclear fusion in its core [Lang, 2001]. Figure 1.1 identifies the three regions of the Sun's interior, from the center outward, as the core, the radiative zone, and the convective zone, with corresponding thicknesses of 174, 322, and 200 Mm, respectively. The hot, dense core of the Sun makes up 25% of the solar interior radius. Energy released there is transported to the surface through the radiative and convective zones, which respectively comprise the other 46% and 29% of the solar interior radius. Energy is transported within the radiative zone through collisions of charged particles with gamma rays that are created in the core. Approximately 170 thousand years after it is released from the core, the energy reaches the convective zone where material convection currents take about a week to finish transporting the energy radially to the solar atmosphere [Lang, 2001; Benestad, 2002].

The boundary between the radiative and convective zones is called the tachocline. Below the tachocline, the rotation of the solar interior is thought to be mostly uniform. Above the tachocline the rotation is non-uniform, resulting in different latitude regions rotating at different rates (differential rotation). The solar rotation period is latitude dependent as the Sun rotates faster at the equator and slower at the poles. This period is 27.27 days at ±16° latitude, approximately 25 days at the equator, and approximately 33 days at high latitudes [Lang, 2001]. At the tachocline it is believed that a strong magnetic field is periodically strengthened and weakened due to a solar dynamo possibly driven by differential rotation and convection [Aschwanden, 2005]. The solar magnetic field is complex and displays an approximate 11-year cycle, over which time the total magnetic flux through the tachocline reaches a maximum during the cycle's peak and then decreases to a minimum. This cycle is defined by a reversal of the dipolar magnetic polarity approximately every eleven years. Thus, a full magnetic cycle, called a Hale cycle, has a period of about 22 years after which time the original magnetic configuration is restored [Hale and Nicholson, 1938]. Solar magnetic fields are generated inside of the Sun and permeate all regions of the solar atmosphere [Lang, 2001]. The solar magnetic field controls the dynamics in magnetic active regions that vary with the solar magnetic cycle.

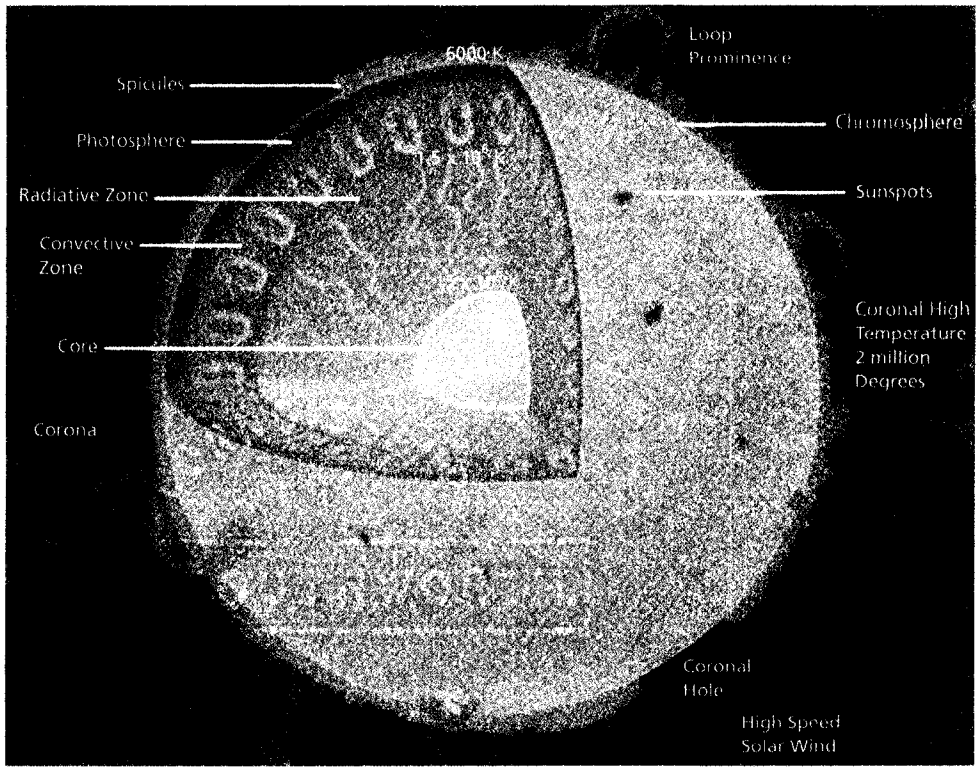

Figure 1.1 The interior and atmosphere of the Sun. The interior of the Sun is divided into three regions: the core, radiative zone, and convective zone, with corresponding thicknesses of 174, 322 and 200 Mm, respectively. The solar atmosphere includes the photosphere, chromosphere, transition region, and the corona, with corresponding thicknesses of 0.35, 2.5, 0.15, and 1600 Mm, respectively. Energy generated in the core through nuclear fusion is carried through the radiative and convective zones to the solar atmosphere, where it radiates at different wavelengths in different altitudes due to the temperature-density-altitude structure of the atmosphere. Figure from Lang [2001].

1.2. Solar Atmosphere

The solar atmosphere begins at the edge of the convective zone and includes, in order of ascending altitude, the photosphere, the chromosphere, the transition region and the corona. Figure 1.1 identified the atmosphere regions of the Sun as well as other atmospheric features such as, sunspots, prominences, and spicules, which are defined in Sections 1.2.1 and 1.2.2. The temperature and mass density structures of the atmosphere vary significantly with altitude. The solar atmospheric temperature is coolest in the photosphere with an effective temperature of 5762 K and a minimum temperature of about 4400 K at the bottom of the chromosphere. The temperature slowly increases with altitude through the chromosphere to approximately 10,000 K, and then jumps by two orders of magnitude in the transition region and into the low corona. The solar atmosphere is least dense in the corona and most dense in the photosphere. The mass density varies inversely with the temperature, as it is at a maximum in the photosphere and steadily declines through the chromosphere, then drops by more than an order of magnitude in the transition region and into the low corona. The temperature-density-altitude structure of the solar atmosphere is shown in Figure 1.2.

1.2.1. Photosphere

The photosphere is approximately 0.35 Mm thick and has an effective temperature of 5762 K. The base of this region is the visible "surface" of the Sun. This region is considered the "surface" because beyond it the solar atmosphere gas is transparent (optically thin), and below it the solar interior gases are highly opaque (optically thick). Therefore, the gases in the photosphere appear to form a distinct edge as the vertical optical depth approaches one. In actuality, the solar atmosphere extends past Earth and has no gas to solid surface. The photosphere is constantly changing through the temporal development of features such as granulation and sunspots. Granulation is the visible textured photospheric pattern that is created by convective motions beneath the photosphere. Sunspots are, by comparison, dark and contain a temporary concentration of strong magnetic fields that are thousands of times more intense than Earth's surface

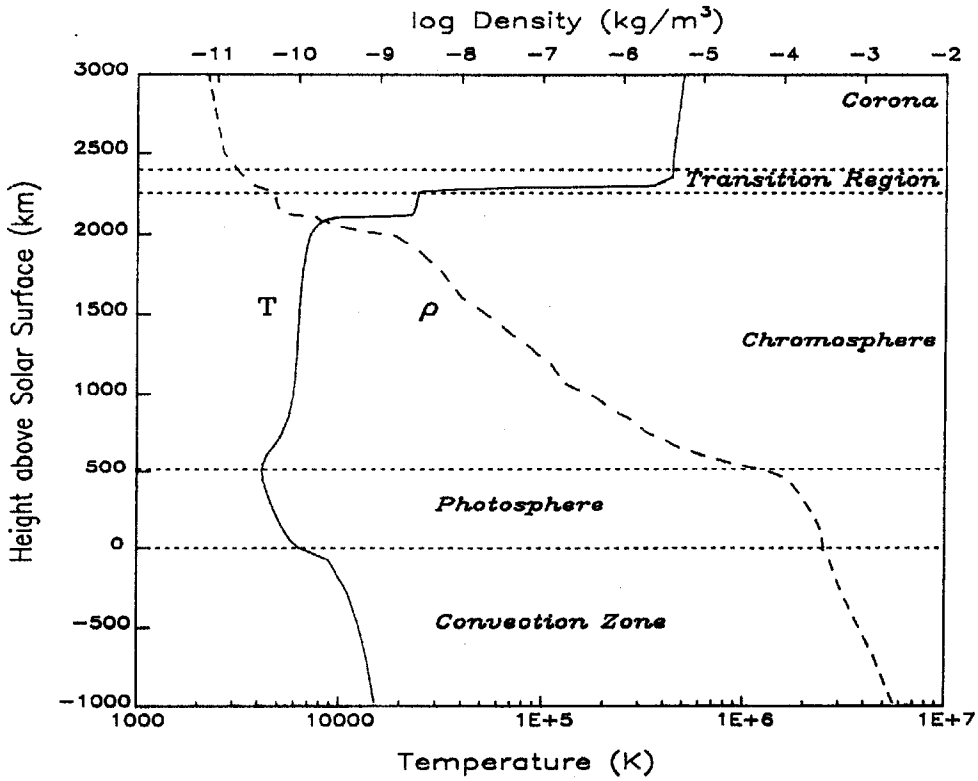

Figure 1.2 The temperature-density-altitude structure of the solar atmosphere. The surface of the Sun lies at the base of the photosphere and is defined in Section 1.2.1. The photosphere has an effective temperature of 5762 K [Aschwanden, 2005]. The minimum temperature of the solar atmosphere, about 4400 K, occurs between the photosphere and chromosphere. The temperature then slowly increases through the chromosphere to approximately 10,000 K and then jumps by two orders of magnitude in the transition region and into the low corona. The solar atmosphere is least dense in the corona and most dense in the photosphere. Figure from Lean [1991].

magnetic field. They appear as dark spots on the photosphere because they are cooler than their surroundings [Lang, 2001]. Figure 1.3a shows an image of the photosphere in visible light taken at the Catania Astrophysical Observatory at 0922 universal time (UT) on 9 September 1997. Three large groups of sunspots are apparent, but the granulation pattern is not easily seen in this image. Sunspots are thought to be formed when buoyant magnetic flux tubes rise through the convection zone to the photosphere and emerge as bipolar sunspot pairs [Aschwanden, 2005]. Figure 1.4 shows an illustration of such a flux tube as described in Schrijver and Zwaan [2000]. The number and latitude of sunspots vary over the 11-year solar magnetic cycle. The sunspot number increases and decreases with solar activity, thus defining the activity. Numerous sunspots define an increase in solar activity because the rate of buoyant flux tubes increases as the tachocline field strengthens [Aschwanden, 2005]. As the solar cycle progresses from minimum to maximum activity, the differential rotation in the tachocline shears the emerging magnetic fields from a poloidal field to a toroidal field, causing sunspot formation locations to migrate from mid-latitudes toward the equator as the solar activity increases [Lang, 2001; Aschwanden, 2005]. Sunspot lifetimes range from hours to months depending on their size, which can range from 1-50 Mm [Lang, 2001]. Magnetized regions in, around, and above sunspots are called active regions.

1.2.2. Chromosphere

The chromosphere is the 2.5 Mm thick partially ionized region of the solar atmosphere above the photosphere where the temperature reaches 10,000 K. This region is less dense than the photosphere and is not observable in visible light due to the bright background of photospheric light. The chromosphere can be viewed at specific visible wavelengths for which the heated gas emits prominent spectral lines such as 656.3 nm (red H-α line), 587.6 nm (yellow He line), 393.4 nm (violet Ca H line), and 396.8 nm (violet Ca K line) [Lang, 2001]. Many chromospheric features are apparent when observed at the Hα wavelength. Prominences and filaments are loops of cooler gas that arch above the photosphere and are suspended by magnetic fields. Dark regions are

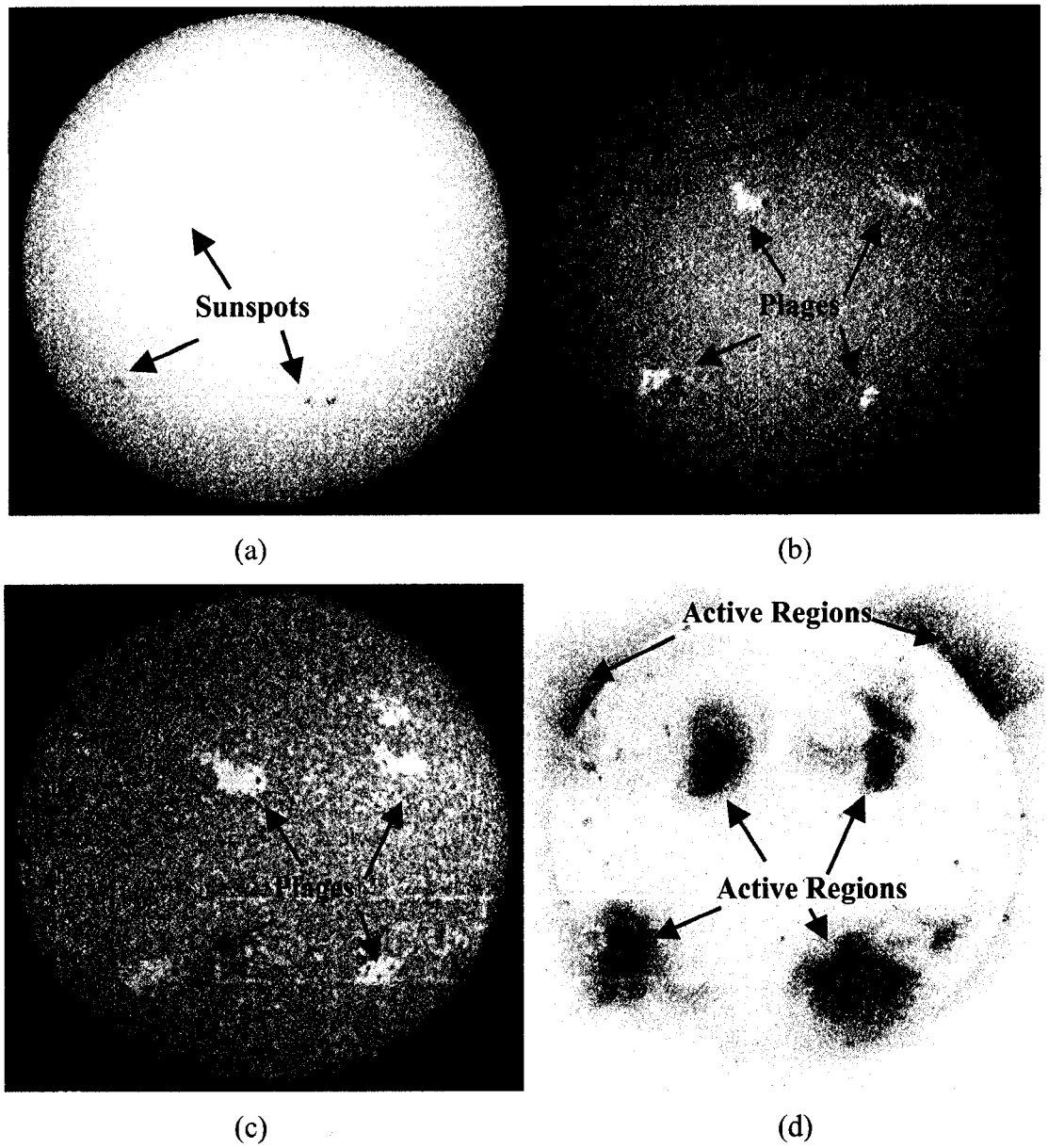

Figure 1.3 Similar solar images in different wavelengths to expose different regions of the solar atmosphere. (a) Sunspots in the photosphere as seen in visible light. (b) & (c) Plages, prominences, and filaments in the chromosphere as seen at (b) 656.3 nm (Hα) and (c) 393.4 nm (Ca K). (d) Active regions in the corona as seen in 0.3-4.5 nm (soft X-rays).

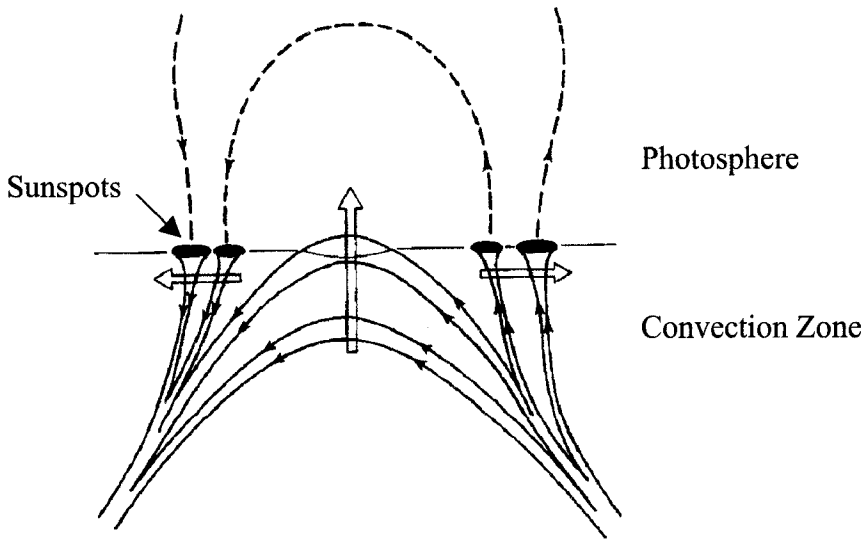

Figure 1.4 Buoyant magnetic flux tubes rise through the convection zone to the photosphere and emerge as bipolar sunspot pairs forming active regions. The flux tubes continue to rise through the chromosphere, the transition region, and into the corona. Figure from Schrijver and Zwaan [2000].

created by sunspots extending from the photosphere. Bright regions called plages are located near sunspots in places of strong magnetic fields. And, spicules are narrow, spike-like structures concentrated around the boundaries of the photospheric granulation patterns. Figure 1.3b showed an image of the chromosphere in Hα taken at the Kanzelhoehe Solar Observatory at 0642 UT on 10 September 1997. As the image showed, plages are located above the sunspots in Figure 1.3a and dark regions are located in the plages. Filaments and prominences are also identified in the northern solar hemisphere. Spicules were pictorially identified in Figure 1.1.

When viewed in the Ca H and Ca K lines, the chromosphere shows a network of strong magnetic fields that appear as bright spots above sunspots and other areas of strong magnetism. One example is the network that traces out boundaries of the large scale photospheric granulation patterns, called supergranulation cells, that move across the photosphere, carrying the magnetic fields with them [Lang, 2001; Hanslmeier, 2002]. Figure 1.3c showed another image of the chromosphere in 393.4 nm (Ca K) taken at the National Solar Observatory at 1419 UT on 10 September 1997. This image also showed plages are located above the sunspots in Figure 1.3a and dark regions are located in the plages. The other smaller bright regions trace out the network of strong magnetic fields that correspond with the regular granulation pattern in the photosphere.

1.2.3. Transition Region and Corona

The transition region is a thin (0.1 Mm) region between the chromosphere and the corona. Here, solar atmospheric plasma becomes fully ionized as the temperature increases by two orders of magnitude and the mass density decreases by two orders of magnitude over the thickness of this region [Lang, 2001; Hanslmeier, 2002]. The mechanism for this dramatic temperature increase is not well understood. The corona, which lies beyond the transition region, is the hottest (10 MK) region of the solar atmosphere and has the lowest mass density ($1x10^{-12}$ kg m^{-3}). The corona is very faint and can only be viewed in visible wavelengths during a total solar eclipse when the brighter parts of the Sun are blocked by the moon. The solar corona is the halo above the solar limb in Figure 1.5. This image was taken from Oranjestad, Aruba during the

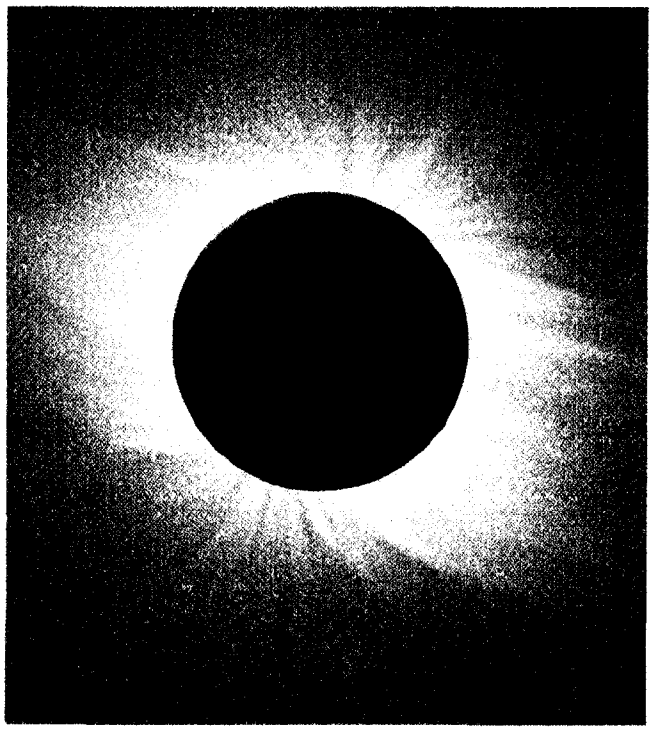

Figure 1.5 The solar corona viewed in visible wavelengths during the total solar eclipse of 26 February 1998 taken from Oranjestad, Aruba. The solar corona is seen as a halo around the solar limb as the brighter parts of the Sun are blocked by the moon. The structure of the corona is observable due to Thomson scattering of visible light by free electrons in the solar corona. The electrons are confined to follow along magnetic field lines but cannot move across them. Thus, the shape of the corona reflects that of the coronal magnetic field lines [Lang, 2001; Aschwanden, 2005]. Figure courtesy of Fred Espenak as shown in Lang [2001].

total solar eclipse of 26 February 1998. The structure of the corona is observable due to Thomson scattering of visible light by free electrons in the solar corona. The electrons are confined to follow along magnetic field lines but cannot move across them. Thus, the shape of the corona reflects that of the coronal magnetic field lines [Lang, 2001; Aschwanden, 2005].

The solar corona can be divided into three types of regions that vary in temperature and size according to the 11-year solar magnetic cycle: coronal holes, quiet regions, and magnetically active regions. Coronal holes describe regions of open magnetic field lines that are generally concentrated in the northern and southern solar polar regions. Coronal holes have temperatures of $T \leq 1$ MK and are cooler than the other areas of the corona because they do not contain hot, dense, plasma trapped in closed magnetic field lines. It is through these regions that heated plasma escapes the corona and is channeled outward as the fast solar wind [Aschwanden, 2005]. Quiet-Sun regions emit at temperatures in the range of $T \approx 1$-3 MK and include all regions of closed magnetic field lines that do not map downward to active regions and generally correspond to minimal magnetic activity.

Active regions emit at temperatures in the range of $T \approx 2$-8 MK and make up a small percentage of the total solar surface, but most of the activity is concentrated here. They extend from the photosphere to the corona, and develop in areas of strong magnetic fields [Lang, 2001; Aschwanden, 2005]. Active regions, and thus sunspots, usually appear in clusters of opposite magnetic polarity with closed magnetic field lines between them. Figure 1.3d showed an image of the corona taken in soft X-ray wavelengths (0.3-4.5 nm) by the Soft X-Ray Telescope (SXT) aboard the Yohkoh satellite on 10 September 1997. Active regions appear above plages and dark regions in the chromosphere, which are above sunspots in the photosphere. Active regions also appear on the limb above prominences in the chromosphere.

Active regions are larger and more numerous with increased solar magnetic activity during the 11-year solar magnetic cycle, and have lifetimes of hours to months depending on the magnetic activity. The permanent magnetic activity in active regions can lead to dynamical processes such as plasma heating, solar flares, and coronal mass

ejections (CMEs), which are eruptions of mass ejected from the corona usually during large solar flare events [Aschwanden, 2005]. Active regions enclose coronal loops that follow magnetic field lines between opposite magnetic polarity regions with footprints embedded in the photosphere. Figure 1.4 illustrated a magnetic flux tube rising from the photosphere to the corona to form an active region. As the flux tube reaches the corona, the magnetic pressure dominates over thermal pressure and magnetically confines the plasma to the loop structure. Therefore, coronal loops contain hot, dense plasma that emits soft X-ray (0.1-30 nm) and extreme ultraviolet (EUV) radiation at 30-120 nm. Figure 1.6 is an image of several coronal loops extending from the low corona to hundreds of millions of meters above the photosphere taken by the Transition Region and Coronal Explorer (TRACE) telescope at 17.1 nm.

1.3. Solar Irradiance

Solar irradiance is defined as the energy emitted or number of photons emitted per unit area per time. Both definitions are used interchangeably and common units of solar irradiance are either W m^{-2} (wavelength bin)$^{-1}$ or photon s^{-1} cm^{-2} (wavelength bin)$^{-1}$, where the wavelength bin can be any defined size. The Sun emits radiation in all wavelength ranges, from radio waves to soft X-rays, and also emits hard X-rays and γ-rays during energetic processes such as solar flares. Different wavelengths are emitted from different altitudes within the solar atmosphere, depending on the temperature at that altitude (see Figure 1.2). There are more highly ionized atoms in the hotter corona than in the lower, cooler regions of the solar atmosphere. Highly ionized atoms have higher energy states and as a result, emit shorter wavelength radiation. Therefore, visible wavelength radiation is emitted in the photosphere, EUV radiation is emitted in the chromosphere, and soft X-rays are emitted in the corona. Figure 1.7 shows the solar irradiance spectrum from soft X-rays to infrared (IR) wavelengths, and the region of the solar atmosphere that emits the radiation. The solar irradiance spectrum is dominated by continuum emissions defined by a blackbody radiation curve for all radiation longward of approximately 135 nm, as shown in Figure 1.7. The peak of this blackbody curve is near 0.5 μm, and the curve represents an effective temperature of 5762 K

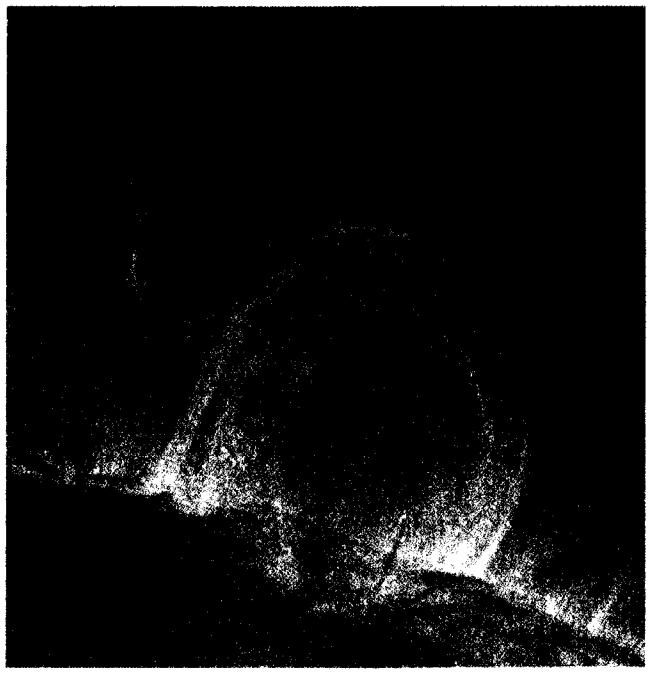

Figure 1.6 Several coronal loops extending from the low corona to hundreds of millions of meters above the photosphere. These coronal loops are filled with heated plasma that is near 1 MK. This image was taken with the Transition Region and Coronal Explorer (TRACE) on 6 November 1999 through emissions at 17.1 nm. Figure courtesy of Markus J. Aschwanden, the TRACE Consortium, the Lockheed Martin Solar and Astrophysics Laboratory (LMSAL) and the National Aeronautics and Space Administration (NASA) as shown in Lang [2001].

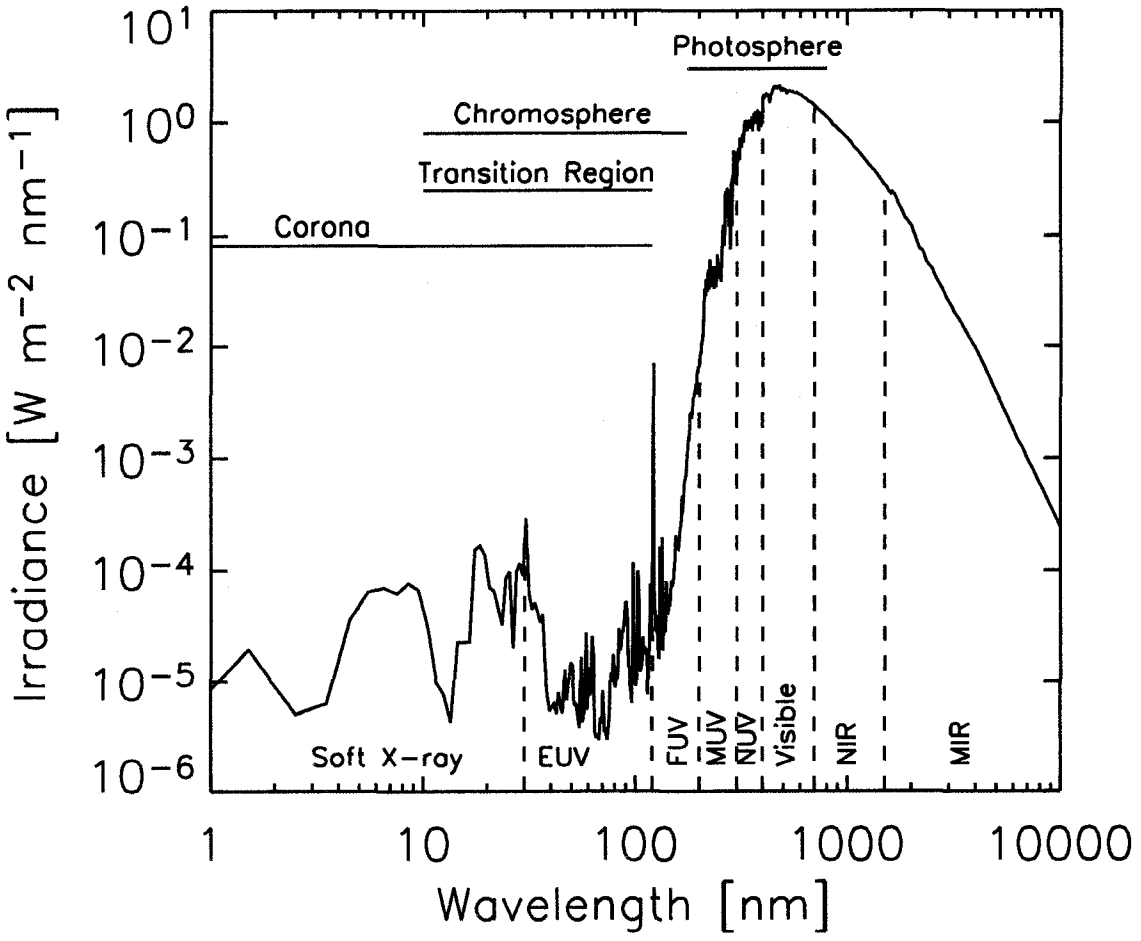

Figure 1.7 The solar irradiance from soft X-rays to infrared (IR) wavelengths and the region of the solar atmosphere that emits the radiation. The spectral regions are defined as: soft X-ray (0.1-30 nm), EUV (30-120 nm), far ultraviolet (FUV 120-200 nm), middle ultraviolet (MUV 200-300 nm), near ultraviolet (NUV 300-400 nm), visible (400-700 nm), near infrared (NIR 700-1500 nm), and middle infrared (MIR 1500-10000 nm). The solar spectrum is dominated by continuum emissions defined by a blackbody radiation curve for all radiation longward of approximately 135 nm, and is dominated by line emissions at wavelengths shorter than 17 nm. Figure from Woods and Chamberlin [2006] and Lean [1991].

[Aschwanden, 2005]. The irradiance spectrum is dominated by line emissions at wavelengths shorter than 17 nm, in particular, the soft X-ray range of the spectrum.

1.4. Solar Soft X-rays

Soft X-rays are produced in solar corona plasmas at 1.5-150 MK through several processes that result in both line and continuum emissions [Gronenschild and Mewe, 1978; Aschwanden, 2005]. The soft X-ray spectrum is dominated by narrow emission lines from the highly ionized coronal elements listed in Table 1.1 [Aschwanden, 2005] as shown in Figures 1.8-1.9. Soft X-ray line emissions are produced by electron collision excitation and decay [Landini and Fossi, 1990]. A line emission is produced when a free electron collides with a bound electron that then moves from a lower orbit to a higher orbit, thus exciting the atom to a higher energy state. When the electron decays to a lower orbit, a photon is emitted whose energy equals the change in energy between the two states. Plasma temperatures increase as electron energies increase; thus, each line emission is strongly dependent on the temperature of the plasma [Aschwanden, 2005; Sitenko and Malnev, 1995]. Therefore, each region of the solar atmosphere emits radiation in different spectral lines according to the temperature of that region.

The solar corona is a fully ionized plasma where electrons and ions (mostly protons) move freely, interacting with each other through their electrostatic charge [Aschwanden, 2005]. Three processes produce the continuous soft X-ray spectrum: Bremsstrahlung radiation, radiative recombination, and two-photon decay of metastable 2s states of hydrogenic and helium like ions [Gronenschild and Mewe, 1978]. Bremsstrahlung radiation, also called free-free transition, occurs when a free electron is scattered in the Coulomb field of an ion and emits a photon that has an energy corresponding to the energy difference of the incoming and outgoing electron [Aschwanden, 2005]. This process is the most common of the three processes that produce the soft X-ray continuum and the least interfering interaction with atomic structures [Aschwanden, 2005]. Radiative recombination, also called free-bound transition, occurs when a free electron is captured by an ion into one of the available energy states while the excess energy is emitted by a photon [Aschwanden, 2005]. Table 1.2 identifies the wavelength

Table 1.1 Elemental abundances in the solar corona and their First Ionization Potential (FIP), which is the minimum energy required to ionize the element. Abundances are given on a logarithmic scale, $12.0+\log_{10}(A/A_H)$, where A is the elemental abundance and A_H is the Hydrogen abundance. Table from Aschwanden [2005].

Element	Coronal Abundance	FIP [eV]
1 H	12.00	13.6
2 He	10.93 ± 0.004	24.6
6 C	8.5	11.3
7 N	7.9	14.5
8 O	8.8	13.6
10 Ne	8.08 ± 0.06	21.6
11 Na	6.3	5.2
12 Mg	7.6	7.6
13 Al	6.4	6.0
14 Si	7.6	8.1
15 P	5.5	10.5
16 S	7.2	10.3
17 Cl	5.8	13.0
18 Ar	6.40 ± 0.06	15.8
20 Ca	6.3	6.1
26 Fe	7.6	7.9
27 Co	5.0	-
28 Ni	6.3	7.6
29 Cu	4.1	-
30 Zn	4.4	-

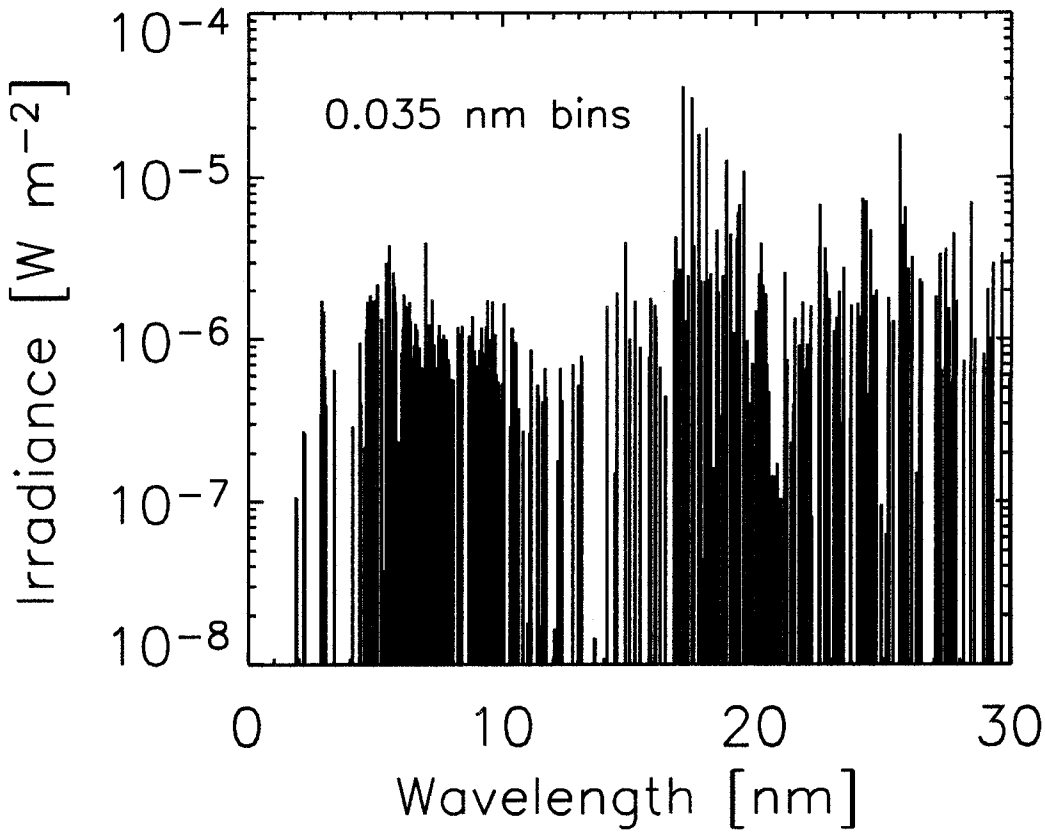

Figure 1.8 The SC#21REFW solar minimum reference spectrum between 1.8-30 nm [Hintegregger et al., 1981].

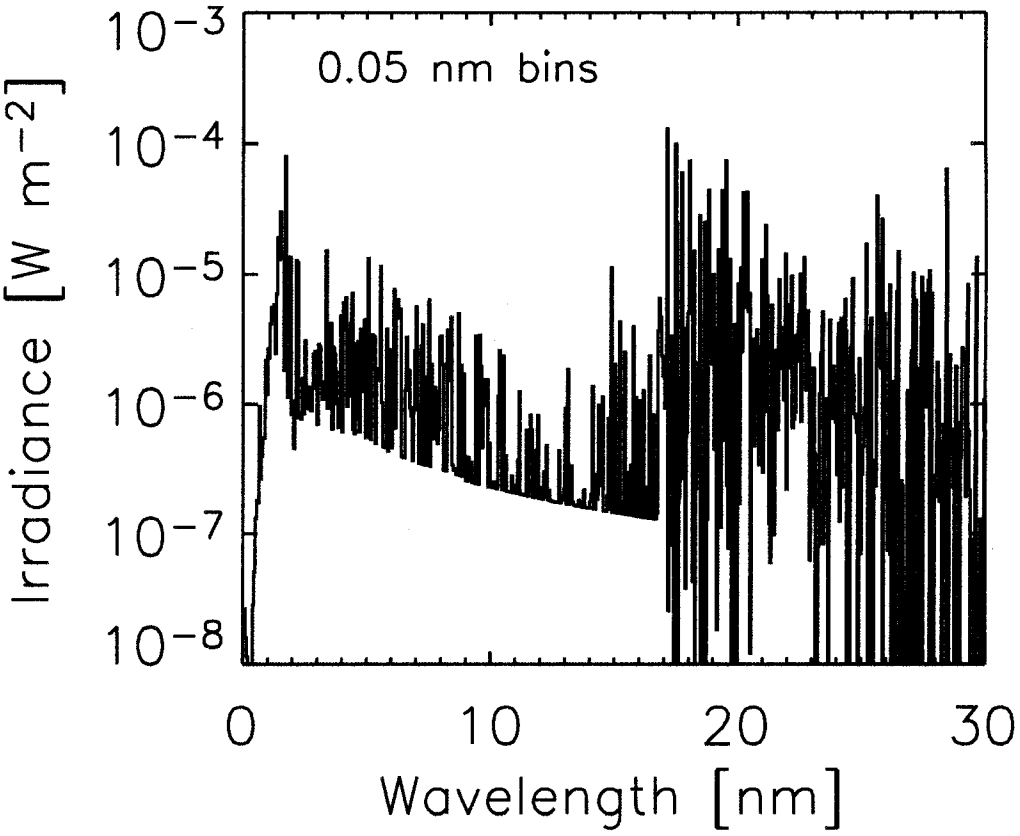

Figure 1.9 New soft X-ray (0.1-30 nm) reference spectrum based on the pre-flare quiet conditions before the 2000 Bastille Day flare (July 14). The reference spectrum was produced from the NRLEUV physics-based model method [Warren et al., 2001] and has been used by Meier et al. [2002] to study effects on Earth's atmosphere due to a solar flare, and by Woods et al. [2005a; 2005b] and Bailey et al. [2006] to interpret soft X-ray irradiance observations.

Table 1.2 Spectral wavelength definitions for EUV radiation, soft and hard X-rays and their associated photon energies. These definitions apply specifically to this dissertation. Also listed is the altitude in Earth's atmosphere where each different wavelength radiation is absorbed.

Spectral Range	Wavelength Range (nm)	Photon Energy (keV)	Altitude of Unit Optical Depth ($\tau = 1$) in Earth's atmosphere (km)
EUV	30-120	0.04-0.01	$150 < h$
Soft X-ray	0.1-30	12.4-0.04	80-150
Hard X-ray	0.01-0.1	124-12.4	30-80

spectral range of soft X-rays and the two surrounding spectral ranges of longer and shorter wavelengths, EUV (30-120 nm) and hard X-rays (0.01-0.1 nm), accordingly. These spectral wavelength definitions apply specifically to this dissertation.

1.4.1. Soft X-ray Observations

Solar soft X-rays are absorbed between 80-150 km in Earth's atmosphere. Therefore, observations of soft X-rays must be made from beyond Earth's atmosphere. Early knowledge of the soft X-ray irradiance came from solar observations made between 1960 and 1981 by several satellites such as SOLRAD [Kreplin, 1970; Kreplin and Horan, 1992], the Orbiting Solar Observatory (OSO) series of satellites [Krieger et al., 1972], the Atmospheric Explorer (AE) series of satellites [Gibson and Van Allen, 1970; Hinteregger et al., 1981; Torr and Torr, 1985], Skylab [Vaiana et al., 1977; Bray et al., 1991], and several sounding rocket programs [Manson, 1976; Feng et al., 1989 and references therein]. More recent soft X-ray irradiance information comes from solar observations made between 1974 and the present by the Geostationary Operational Environmental Satellite (GOES) X-ray Sensor (XRS) and Solar X-ray Imager (SXI) instruments [Garcia, 1994; Hanser and Sellers, 1996; Hill et al., 2005], the Yohkoh Soft X-ray Telescope [Tsuneta et al., 1991; Acton et al., 1999], the CORONAS-I mission [Kazachevskaya et al., 1998], the Solar and Heliospheric Observatory (SOHO) Solar EUV Monitor (SEM) [Judge et al., 1998], the SNOE Solar X-ray Photometer (SXP) [Bailey et al., 2000; 2001], the TIMED Solar EUV Experiment (SEE) X-ray ultraviolet (XUV) Photometer System (XPS) [Woods et al., 2005a], the SORCE XPS [Woods and Rottman, 2005], and several sounding rocket instruments [Woods et al., 1998; Bailey et al., 1999a; 2005]. Table 1.3 lists all soft X-ray irradiance satellite instruments to date.

Soft X-ray irradiance observations made before 1998 were sparse and did not cover the full range of solar activity. Measurements by the SNOE SXP between 1998 and 2003 improved the understanding of the solar soft X-ray irradiance through the use of new soft X-ray sensitive detectors [Bailey et al, 1999a], precise calibrations with known synchrotron light sources, and validation measurements made by sounding rocket underflights [Bailey et al., 2006]. The SEE XPS (2002-present) and the SORCE XPS

Table 1.3 History of soft X-ray irradiance satellite instruments.

Satellite / Instrument	Wavelength Range (nm)	Time Period
SOLRAD 1-11	1-10	1960-1976
OSO 3-6	2-40	1967-1970
Skylab	0.5-6	1973-1974
AE C-E	14-185	1974-1981
GOES / XRS	0.1-0.8	1974-Present
Yohkoh / SXT	0.2-3	1992-2001
CORONAS-I	1, 7, 28-50, 121.6	1994
SOHO / SEM	26-34	1996-Present
SNOE / SXP	0.1-20	1998-2003
TIMED-SEE / XPS	0.1-27	2002-Present
GOES / SXI	0.6-6	2003-Present
SORCE / XPS	0.1-34	2003-Present

(2003-present) currently measure the soft X-ray irradiance using the same technique as SNOE, and have continued to improve understanding of this spectral region [Woods et al., 2005a; Woods and Rottman, 2005].

Analysis of SNOE SXP measurements [Bailey et al., 1999b; 2000; 2001] confirmed contentions that the solar soft X-ray irradiance is larger by a factor of approximately four than suggested by earlier measurements and empirical models such as by Hinteregger et al. [1981]. Solomon et al. [2001] used the SNOE soft X-ray irradiance factor of four adjustment to accurately predict E-region electron densities and photoelectron fluxes in Earth's ionosphere. Barth and Bailey [2004] used the SNOE soft X-ray irradiance in a photochemical model to accurately explain SNOE NO observations, and Eastes et al. [2004] showed that the SNOE irradiance correlated well with satellite drag observations of neutral densities in Earth's thermosphere. Bailey et al. [2006] showed that SNOE soft X-ray irradiance varies linearly with the 10.7 cm radio flux (F10.7) index of solar activity. Also, SNOE soft X-ray irradiance showed similar 27-day solar rotation and 11-year solar magnetic cycle variability to SEE soft X-ray irradiance observations, but are a factor of 1.3-2 larger. The discrepancy of SNOE and SEE soft X-ray irradiance is attributed to revised SEE calibrations [Bailey et al., 2006]. Spare photodiode soft X-ray detectors were calibrated after the launch of SEE, and their calibrations were transferred to the SEE flight photodiode detectors using solar observations of an underflight sounding rocket experiment.

1.4.2. Soft X-ray Irradiance Models

The first widely used soft X-ray irradiance model was the Hinteregger et al. [1981] empirical model based on measurements with AE-E and several sounding rocket instruments. This model covers the spectral range of 1.8-102.7 nm and is based on two solar activity proxies; the chromospheric H I Lyman β (102.6 nm) and coronal Fe XVI (33.5 nm) emissions, which were not typically available prior to SEE solar observations. These two proxies were correlated with the F10.7 index and its 81-day average, and then used to determine the soft X-ray irradiance model. Hinteregger established a solar minimum reference spectrum referred to as SC#21REFW, which was shown in Figure

1.8. The Hinteregger model is referred to as SERF 1 by the Solar Electromagnetic Radiation Flux subgroup of the World Ionosphere-Thermosphere Study [Bailey et al., 2000; 2001]. More recently, Richards et al. [1994] developed a proxy model based on F10.7 called EUVAC, which increased the solar soft X-ray irradiances by a factor of 2 to 3 as compared to the SERF 1 model. Several proxy models have been developed over the years by Tobiska and coworkers. These include SERF 2 by Tobiska and Barth [1990], EUV91 by Tobiska [1991], EUV97 by Tobiska and Eparvier [1998], and SOLAR2000 by Tobiska et al. [2000]. Tobiska and coworkers continue to update and expand their model as more data sets become available.

Earth atmospheric studies by Richards and Torr [1984 ;1985], Barth et al. [1988], and Siskind et al. [1990; 1995] provided evidence that the empirical models underestimate the soft X-ray irradiance. Solomon [1991] summarizes the discrepancies between reported soft X-ray irradiances, empirical models, and the irradiances required to explain observations of Earth's atmosphere. A specific limitation to the Hintegregger empirical model and SC#21REFW soft X-ray spectrum is the lack of spectral information at wavelengths less than 1.8 nm. Recent development of soft X-ray irradiance physics-based models by Warren et al. [1998a; 1998b; 2001], Fontenla et al. [1999] and Lean et al. [1982] have produced the NRLEUV model, which extends the range to wavelengths below 1.8 nm. The approach used in constructing the NRLEUV model was to formulate a new reference spectrum based on the pre-flare quiet conditions before the 2000 Bastille Day flare (July 14). This reference spectrum, shown in Figure 1.9, extends to 0.075 nm and was used by Meier et al. [2002] to study the effects of solar soft X-ray enhancement on Earth's atmosphere during the 21 April 2002 X1.5 solar flare, and to interpret SEE and SNOE [Woods et al., 2005a; 2005b; Bailey et al., 2006] soft X-ray observations.

1.4.3. Soft X-ray Variability

Soft X-ray production varies on all timescales, mainly because soft X-ray production mechanisms are directly coupled to the variable magnetic activity of the Sun. Long-term variations follow the 11-year solar magnetic cycle, intermediate variations follow the 27-

day solar rotation as coronal loops appear and disappear on the solar disk, and short-term variations lasting minutes to hours occur during a flare. Reviews of soft X-ray irradiance and its variability are found in Lean [1987; 1991], Woods et al. [2004a] and Bailey et al. [2000, 2001, 2006]. Bailey et al. [2006] reported that the soft X-ray irradiance variability during both the 27-day solar rotation period and the 11-year solar magnetic cycle varies with wavelength. Based on the SNOE passbands of 0.1-7 nm, 6-19 nm, and 17-20 nm, the 27-day variability is 44%, 28%, and 14%, respectively, and the 11-year variability is approximately factors of 11, 6, and 5, respectively. Solar radiation generally becomes more variable higher in the solar atmosphere as the mass density decreases with altitude and the temperature increases with altitude [Woods et al., 2004a]. Highly ionized atoms have higher energy states resulting in higher temperature emissions that occur at shorter wavelengths. Therefore, coronal emissions are more variable than transition region emissions, which vary more than chromospheric emissions. Also, the shorter wavelength coronal emissions (0.1-7 nm) vary more than the emissions between 6-19 nm, which vary more than emissions between 17-20 nm.

Figure 1.10 shows SXT Yohkoh soft X-ray images of the solar corona every 120 days, ranging from solar maximum conditions to solar minimum conditions between 1991 (left) and 1995 (right). The bright regions come from hot (≈1 MK) coronal plasma trapped in coronal loops that emits soft X-rays [Lang, 2001]. The bright active regions are more numerous during maximum solar activity and almost disappear during minimum conditions, thus illustrating the long-term 11-year variability of soft X-rays.

1.5. Solar Flares

The dynamics and topology of all solar coronal phenomena, such as flares, are controlled by the solar magnetic field [Aschwanden, 2005]. Solar flares are responsible for the emission of radiation characteristic of temperatures in the range of T≈10-40 MK within coronal active regions, where there are strong magnetic field concentrations associated with the sunspots beneath them [Aschwanden, 2005]. Solar flares cause short-term variations in the soft X-ray irradiance through the rapid release of energy in the solar corona. Current thinking dictates that the release is probably triggered by

Figure 1.10 Soft X-ray images of the solar corona from solar maximum conditions to solar minimum conditions. Images were taken 120 days apart, beginning in 1991 (left) and ending in 1995 (right) by the SXT aboard the Yohkoh satellite. The active regions are more numerous during maximum activity and have almost disappeared during minimum conditions. The bright regions come from hot (≈1 MK) coronal plasma trapped in coronal loops. Figure courtesy of Gregory L. Slater and Gary A. Linford, NASA, the Institute of Space and Astronautical Science (ISAS), LMSAL, the National Astronomical Observatory of Japan, and the University of Tokyo as shown in Lang [2001].

magnetic reconnection above the top of a coronal loop. The first recorded observation of a solar flare was made 1 September 1859 by two independent observers, R. C. Carrington and R. Hodgson [Tandberg-Hanssen & Emslie, 1988]. They observed a white-light flare as an intense flash of light near a complex sunspot group. White-light flares are rare as they originate in the chromosphere and enhance the visible wavelength spectrum [Tandberg-Hanssen, 1988; Aschwanden, 2005]. Most flares, however, emit the majority of their radiation in the soft X-ray region of the spectrum [Lang, 2001; Woods et al., 2005a].

Solar flares are often classified by the magnitude of peak irradiance at wavelengths between 0.1-0.8 nm using the conversion scale described in Table 1.4. The classification of X, M or C is augmented by a number after the letter classification to represent the magnitude of the peak irradiance of the flare. For example, X1.5 stands for a peak soft X-ray irradiance of 1.5 $x10^{-4}$ Wm^{-2}. The peak soft X-ray irradiance has been continually measured by the GOES XRS 0.1-0.8 nm channel since 1974 [Garcia, 1994].

Garcia [2000] surveyed approximately 1100 solar flares observed by the GOES XRS during solar cycles 21 and 22 (1976-1995) and reported that, on average, there was one X-class flare per month and one M-class flare every 2 days. Flare occurrence rates follow the 11-year solar cycle and are more frequent during solar maximum [Popescu et al., 2002; Woods et al., 2005a]. The majority of larger flares occur during the latter part of solar maximum, with some periods of increased flare activity after solar maximum, during the descending phase of the solar cycle [Popescu et al., 2002].

The emphasis has been of soft X-ray emission, but flares emit radiation over a broad range, from radio waves to hard X-rays, and the time profile of each flare varies depending on the observed wavelength. Additionally, the time evolution of a flare is defined by three phases: A precursor phase, an impulsive phase, and a gradual phase [Lang, 2001]. Figure 1.11 shows a schematic profile of the flare irradiance in varying wavelengths over a relative time scale. Different wavelength emissions dominate the flare spectrum at different times during a flare. The precursor phase is described by gradual increases in the X-ray (0.04-0.1 nm), soft X-ray (0.1-7 nm) and EUV (7-103 nm)

Table 1.4 The soft X-ray classification of solar flares based on the peak soft X-ray irradiance between 0.1-0.8 nm measured at Earth. A number following each classification letter denotes the peak irradiance. For example, X1.5 stands for a peak soft X-ray irradiance of 1.5×10^{-4} Wm^{-2}.

Classification	Peak Irradiance (I) between 0.1-0.8 nm at Earth (Wm^{-2})
X	$10^{-4} \leq I$
M	$10^{-5} \leq I < 10^{-4}$
C	$10^{-6} \leq I < 10^{-5}$

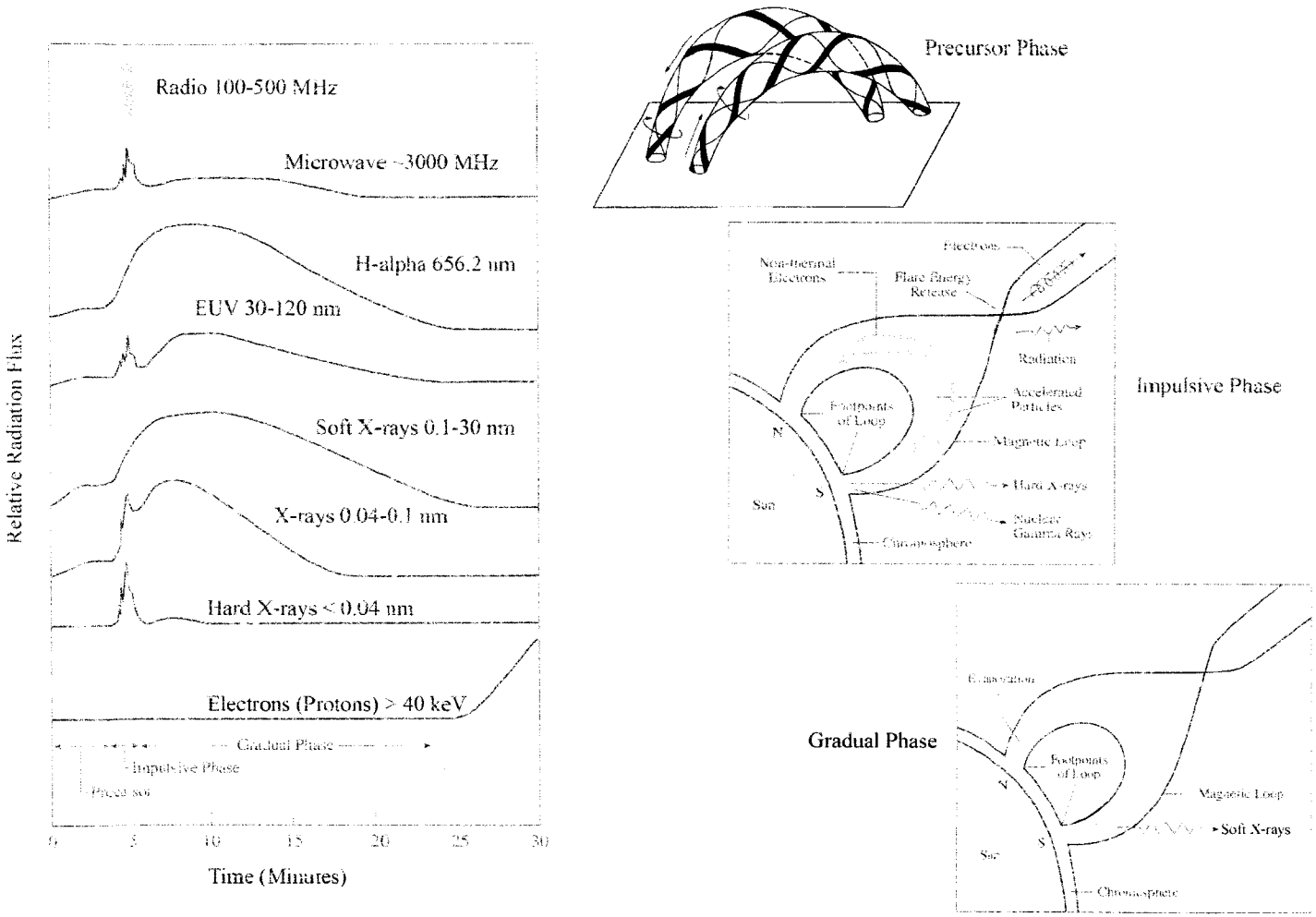

Figure 1.11 The time evolution of a flare is defined by three phases: A precursor phase, an impulsive phase, and a gradual phase. Figures from Lang [2001].

emissions. During the impulsive phase, electrons are rapidly accelerated to high energies as they emit radio bursts (0.6-3 m), microwave (0.1 m) and EUV radiation, X-rays and hard X-rays (0-0.04 nm). The gradual phase emissions of the flare are dominated by bremsstrahlung X-rays and soft X-rays.

The 28 October 2003 X18 solar flare was observed by GOES-12. The irradiance was observed in the 0.1-0.8 nm bandpass, which is in the X-ray and soft X-ray wavelength range. All three phases (precursor, impulsive and gradual) of the X18 flare are identified in Figure 1.12. There was a steady rise in the X-ray and soft X-ray emissions during the precursor phase, a sharp increase in X-ray and soft X-ray emissions during the impulse phase, and a gradual decay of X-ray and soft X-ray emissions during the gradual phase of the flare. The precursor phase of this large X18 flare lasted approximately 30 minutes, and the impulse and gradual phase lasted approximately 1.7 hours. The time evolution of individual solar flares varies in duration and complexity depending on the size and type of flare.

The precursor flare phase occurs when coronal loops in regions of strong magnetic field concentrations, such as active regions, make contact with other magnetic loops as was illustrated in Figure 1.11. This can happen when magnetic loops become twisted due to photospheric motion and are then forced together by that same underlying convective motion, or when newly emerging magnetic loops rise from the photosphere to merge with an existing coronal loop [Priest, 1981; Lang, 2001]. The precursor magnetic configuration will continue to evolve until at some critical point it becomes unstable, causing the magnetic fields to partially annihilate each other and then reconnect into a new magnetic configuration [Priest, 1981; Lang, 2001]. Aschwanden [2005] describes the most widely accepted standard solar flare model as the 2D magnetic reconnection model that evolved from the concepts of Carmichael [1964], Sturrock [1966], Hirayama [1974], and Kopp and Pneuman [1976]. This flare model was further elaborated by Tsuneta [1996; 1997] and Shibata [1995], based on Yohkoh observations. The precursor phase activity leading to the magnetic instability in this flare model is driven by a rising prominence or fast expanding coronal arches above the magnetic

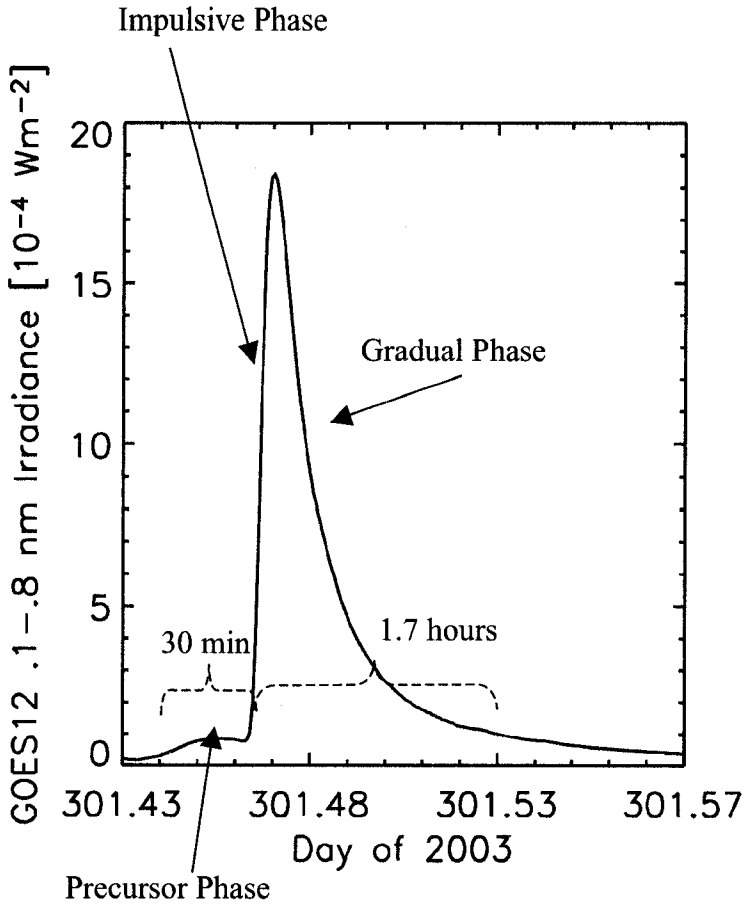

Figure 1.12 The 28 October 2003 X18 solar flare as observed by GOES-12 in the 0.1-0.8 nm bandpass, which is in the X-ray and soft X-ray wavelength range. All three phases (precursor, impulsive and gradual) of the X18 flare are identified. There is a steady rise in the X-ray, and soft X-ray emissions during the precursor phase, a sharp increase in X-ray and soft X-ray emissions during the impulse phase, and a gradual decay of X-ray and soft X-ray emissions during the gradual phase of the flare.

polarity neutral line through an active region, as seen in Figure 1.13a [Hirayama, 1974]. Figure 1.13b shows a rising prominence stretching a current sheet above a neutral line to the point of instability, thus initiating magnetic reconnection below the erupting prominence [Hirayama, 1974]. A side view of this process is shown in Figure 1.13b'.

The coronal loop can be pulled into a peak or cusp shape at the reconnection point, as shown in Figures 1.11 and 1.14, where energy is released in the form of an explosion which indicates the impulsive phase. Magnetic energy is converted to kinetic energy in the electrons, which are then accelerated along the magnetic field lines and generate a burst of radio energy and hard X-ray emissions at the top of the flare loop (Figure 1.11) [Lang, 2001]. Simultaneously, non-thermal electrons and protons are accelerated down the magnetic field lines to the chromosphere (Figure 1.11), where the atmosphere is denser. Here, the electrons radiate by non-thermal bremsstrahlung radiation and the protons collide with heavier nuclei to produce gamma rays [Aschwanden, 2005; Lang, 2001]. These three areas of hard X-ray emissions are seen in Figure 1.14 (right) near the coronal loop top and footprints, and are associated with the flare impulsive phase.

The gradual phase of the flare is considered a solar atmospheric response to the impulsive phase. The newly injected electrons and protons in the chromosphere heat up the surrounding cooler plasma, causing it to rise through the magnetic loop to the lower corona during a process called chromospheric evaporation [Achwanden, 2005]. This process allows very hot plasma (10-40 MK) to fill up the same magnetic loop and emit soft X-rays through thermal bremsstrahlung radiation during the flare gradual phase. Figure 1.14 (right) shows soft X-rays emitted along the magnetic loop during a solar flare. The observed rise of the soft X-rays in the gradual phase corresponds to the time integral of the impulsive hard X-ray and microwave bursts and is known as the Neupert [1968] effect. The derivative of the soft X-ray emission corresponds to the magnitude of the hard X-ray emission through this empirical relationship.

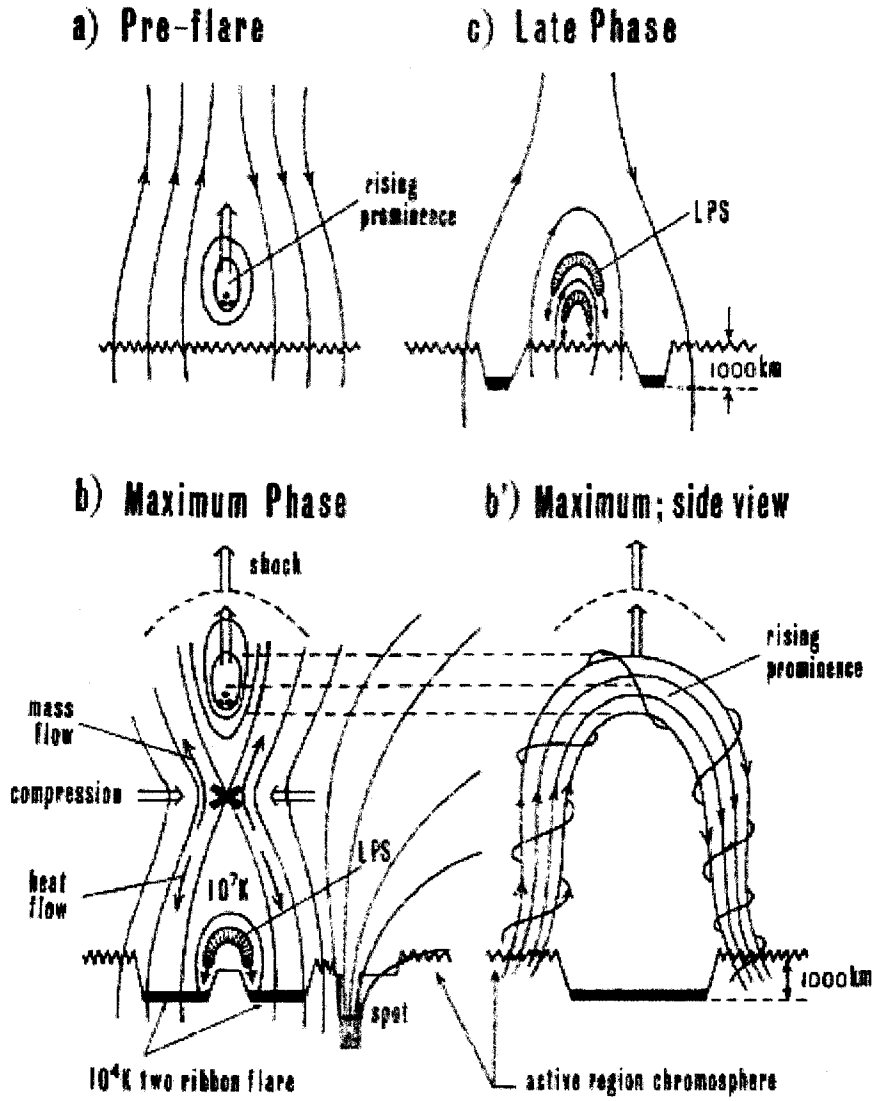

Figure 1.13 2D magnetic reconnection model is the most widely accepted standard solar flare model. a) Prominence, or fast expanding coronal arch, rises above the magnetic polarity neutral line through an active region. b) Rising prominence triggers a magnetic reconnection below an erupting prominence. b') Side view. c) Chromospheric evaporated plasma within the post flare loop prominence systems (LPS) is confined to the newly reconnected magnetic field below the reconnection point. Figure from Hirayama [1974].

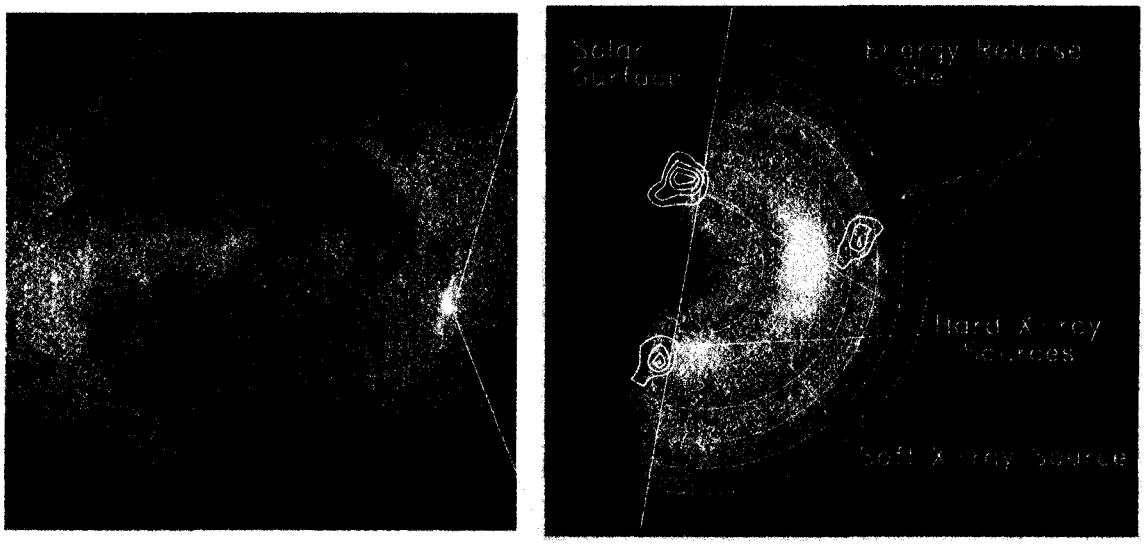

Figure 1.14 [Left] Soft X-ray image of the solar corona. [Right] Soft X-ray emission and hard X-ray contour map. The contour map shows the three regions where hard X-rays are emitted during the impulsive phase of solar flare. These locations are the coronal loop top near the magnetic reconnection point and near the coronal loop footprints. Soft X-rays are emitted during the gradual phase of the flare along the magnetic loop after chromospheric evaporation occurs due to the hard X-ray emissions during the impulsive phase. The image on the left was taken 13 January 1992 by the Yohkoh SXT. The color image on the right is a blow up of the indicated region in the left plot, and the contour plot on the right was taken the same day by the Yohkoh Hard X-ray Telescope (HXT). Figure courtesy of Satoshi Masuda, NASA, ISAS, LMSAL, the National Astronomical Observatory of Japan, and the University of Tokyo as shown in Lang [2001].

1.6. Solar Flare Soft X-ray Irradiance

Solar flares dramatically enhance the soft X-ray region of the solar spectrum. Woods et al. [2003; 2004b] confirm through analysis of SEE soft X-ray observations that there was a factor of 8 increase in the 0.1-7 nm irradiance during the 21 April 2002 X1.6 solar flare and a factor of 42 increase in the 0.1-7 nm irradiance during the 28 October 2003 X18 solar flare. Additionally, Meier et al. [2002] concluded that solar X-rays from 0.05 to 0.8 nm increased by more than a factor of 200 during the 2000 Bastille Day (July 14) X5 flare. Such large increases in soft X-ray irradiance can enhance a solar flare spectrum more significantly than previously thought, and suggest a need for further studies to better understand solar flare soft X-ray irradiance. Woods et al. [2004b] also examined the total solar irradiance (TSI) during the X18 flare from TIMED and SORCE soft X-ray observations. They concluded that 19% of the TSI changes during the X18 flare were due to solar soft X-rays between 0.1-27 nm. This result, along with TSI changes in other wavelength ranges, indicates that the majority of the X18 flare's energy was released at wavelengths shortward of 27 nm and longward of 200 nm. Meier et al. [2002] and Woods et al. [2003; 2004b] indicate that as the soft X-ray wavelengths become shorter and shorter, there is more of an increase in the magnitude of soft X-ray irradiance during a flare. They also discuss the importance of studying the variability of the solar irradiance on short time scales, such as during a solar flare.

Typical solar flare plasma temperatures range from 10-40 MK [Aschwanden, 2005], and the most intense plasma temperatures of flares reach approximately 50 MK [Garcia, 1998]. The solar soft X-ray spectrum varies with plasma temperature. As the plasma temperature increases, the relative contribution from short wavelengths becomes more significant. Specifically, the continuum emissions increase and line emissions emerge at wavelengths shorter than in pre-flare conditions for wavelengths from 0.1 to 2 nm [Mitra, 1974]. Figure 1.15 illustrates how the solar soft X-ray spectrum between 0.1-10 nm varies with increasing plasma temperature. Each curve in Figure 1.15 is a spectrum at one temperature plus the sum of all the spectra at the cooler temperatures for a fixed plasma density between 1 MK (blue) and 100 MK (red). As the plasma temperature

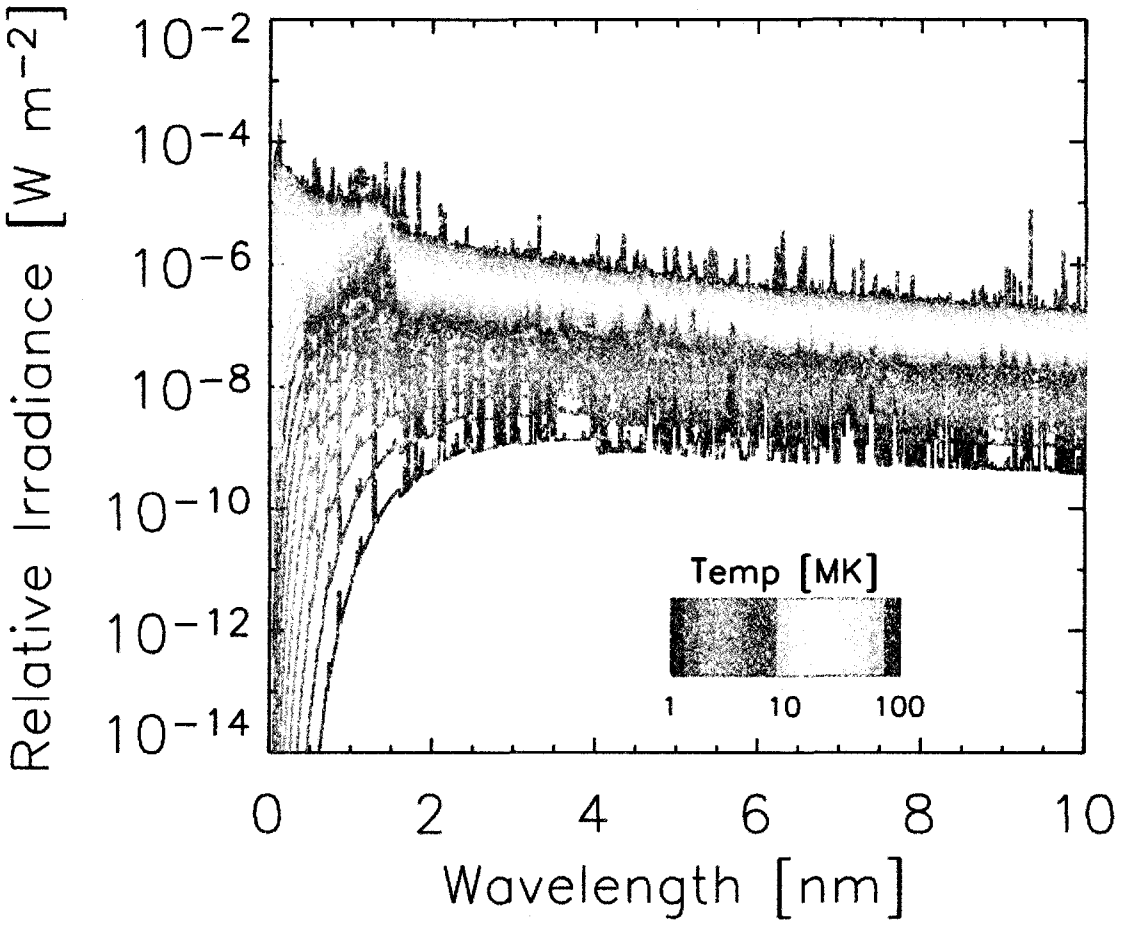

Figure 1.15 The solar soft X-ray spectrum between 0.1-10 nm varies with increasing plasma temperature. Each curve represents an isothermal assumption of the coronal plasma temperature. Each curve is a solar soft X-ray spectrum at a certain temperature plus the sum of all the spectra at the cooler temperatures for a fixed plasma density between 1 MK (blue) and 100 MK (red). Quiet-sun regions have temperatures of 1-3 MK (blue colors), active regions have temperatures of 2-8 MK (green colors), and flares have temperatures of 10-50 MK (yellow-orange colors). The solar irradiance in the wavelength range of 0.1-2 nm increases by three orders of magnitude from temperatures of 5-100 MK (green-red) for a fixed plasma density.

increases, emission lines in the short end of the spectrum begin to appear and dominate the spectrum. Of particular interest is the wavelength range of 0.1-2 nm, where the irradiance can increase by three orders of magnitude from temperatures of 5-100 MK (green-red) for a fixed plasma density.

The dramatic increase in soft X-ray irradiance between 0.1-2 nm is due to the emergence of numerous highly ionized Fe emissions lines that are radiated at temperatures equal to and greater than 8 MK as shown in Figure 1.16. The five most abundant elemental coronal emission lines from the CHIANTI 5.1 atomic database [Dere et al., 1997; Landi et al., 2006] that occur at temperatures between 3-100 MK and wavelengths between 0.1-7 nm are shown in Figure 1.16. The emission lines originate from highly ionized Fe, S, Si, Ni, and Ar. The magnitude of each vertical line represents the temperature at which the emission radiates. Figure 1.17 shows the number of coronal emission lines at and below 3, 10, 32 and 100 MK between 0-7 nm in 1 nm bins. Very few emission lines occur between 5-7 nm for temperatures less than 3 MK. There is an increase in mostly Fe emission lines at all wavelengths between 0-7 nm and a large increase of Fe emission lines between 1-2 nm for temperatures less than 10 MK. The number of Fe emission lines sharply increases between 0-1 nm and continues to increase between 1-2 nm for all temperatures up to 100 MK. Most of the numerous highly ionized Fe emissions lines between 0.1-2 nm are in the 1-2 nm range and are radiated at temperatures equal to and greater than 8 MK. Therefore, solar flare plasma at temperatures of 10-50 MK are hot enough to excite the highly ionized Fe emission lines between 0.1-2 nm that dominate the soft X-ray spectrum at these hot temperatures.

The solar flare soft X-ray spectrum between 0.1-7 nm for the 21 April 2002 X1.6, flare shown in Figure 1.18, confirms a large increase in the 0.1-2 nm irradiance during the flare. A complete discussion of how this flare spectrum was retrieved can be found in Section 3. This flare spectrum was compared to the flare spectrum representing the pre-flare quiet-Sun conditions before the 2000 Bastille Day flare and the comparison is shown in Figure 1.19. The 0.1-2 nm irradiance, which dominates the X1.6 solar flare spectrum, is found to be up to a factor of 10 higher than the pre-flare spectrum in the 1-2

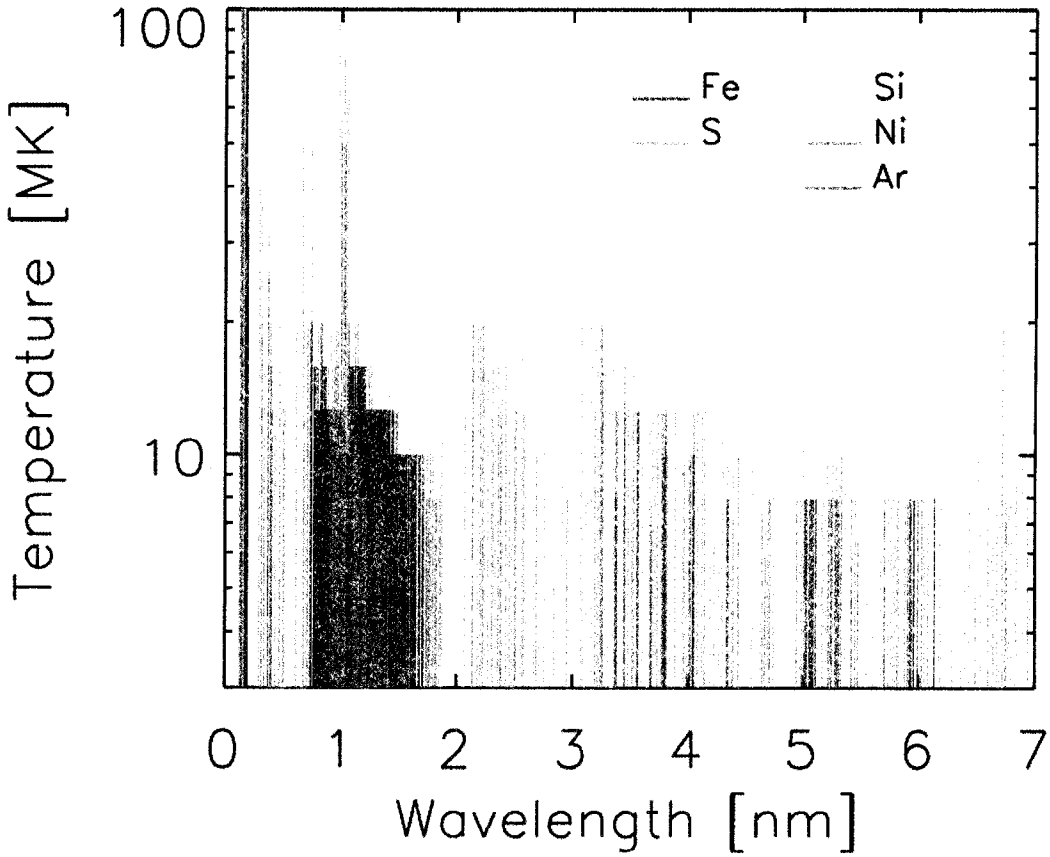

Figure 1.16 The five most abundant elemental coronal emission lines at temperatures between T=3-100 MK and wavelengths between 0.1-7 nm. These emission lines occur from highly ionized Fe, S, Si, Ni, and Ar. The magnitude of each vertical line represents the temperature at which the emission radiates. Most emission lines between 0.1-7 nm occur from highly ionized Fe with temperatures greater than 3 MK. There is an emergence of numerous highly ionized Fe emissions lines between 0.1-2 nm that are radiated at temperatures equal to and greater than 8 MK, which cause a dramatic increase in the 0.1-2 nm solar flare irradiance. Emission line data from CHIANTI 5.1 atomic data base [Dere et al., 1997; Landi et al., 2006].

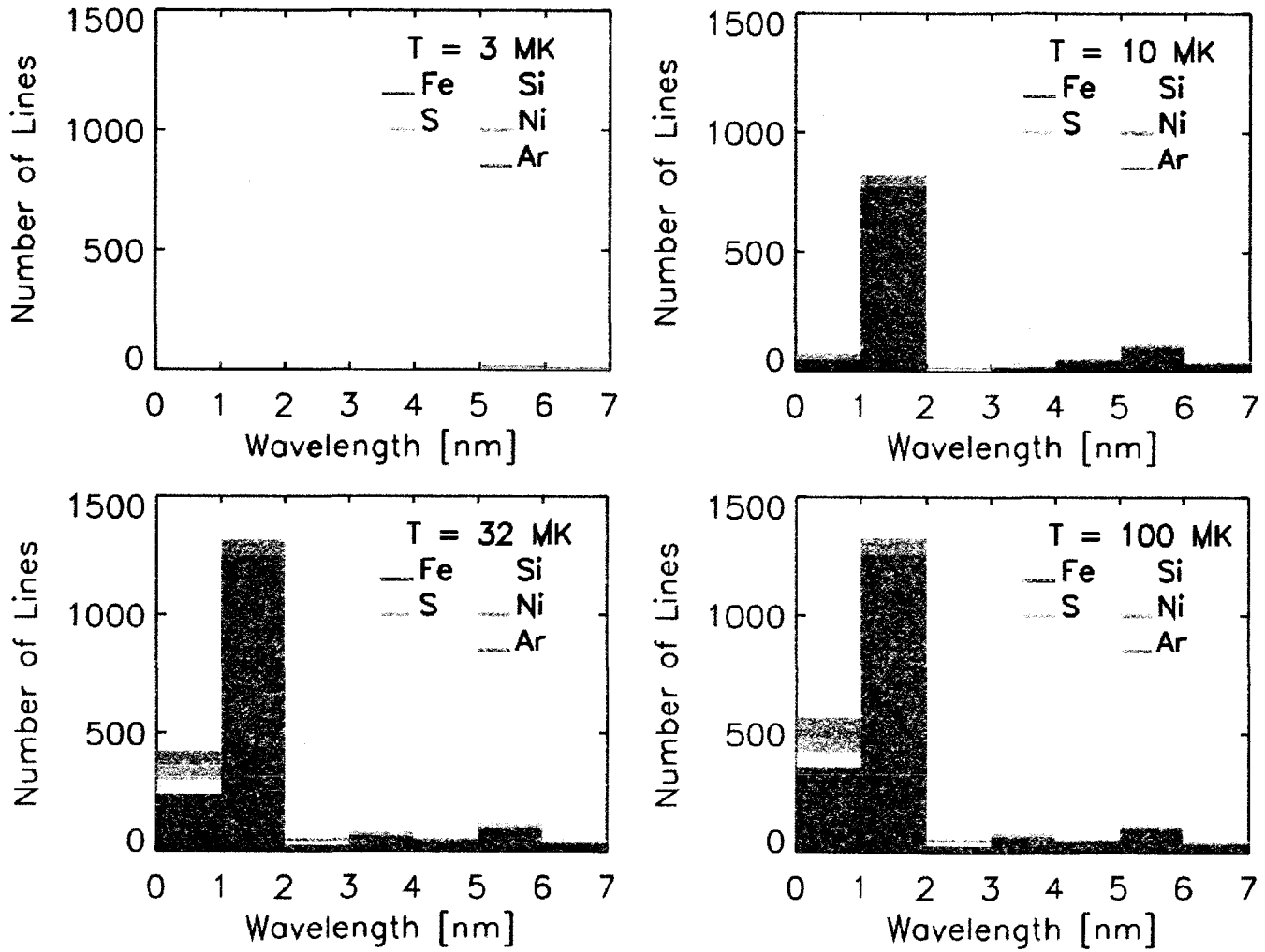

Figure 1.17 Number of coronal emission lines at and below temperatures of 3, 10, 32 and 100 MK of the five most numerous elemental coronal emission lines [Dere et al., 1997; Landi et al., 2006].

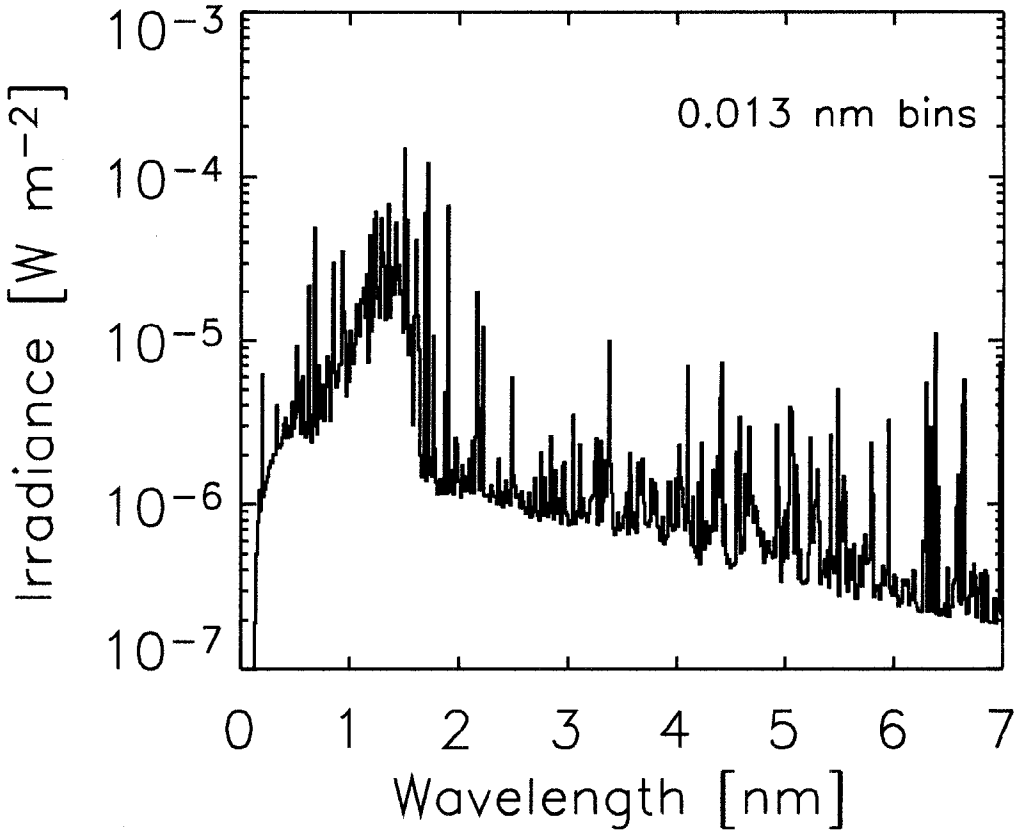

Figure 1.18 Solar flare soft X-ray irradiance between 0.1-7 nm for 21 April 2002 X1.5 flare. The 0.1-2 nm irradiance dominates the flare spectrum.

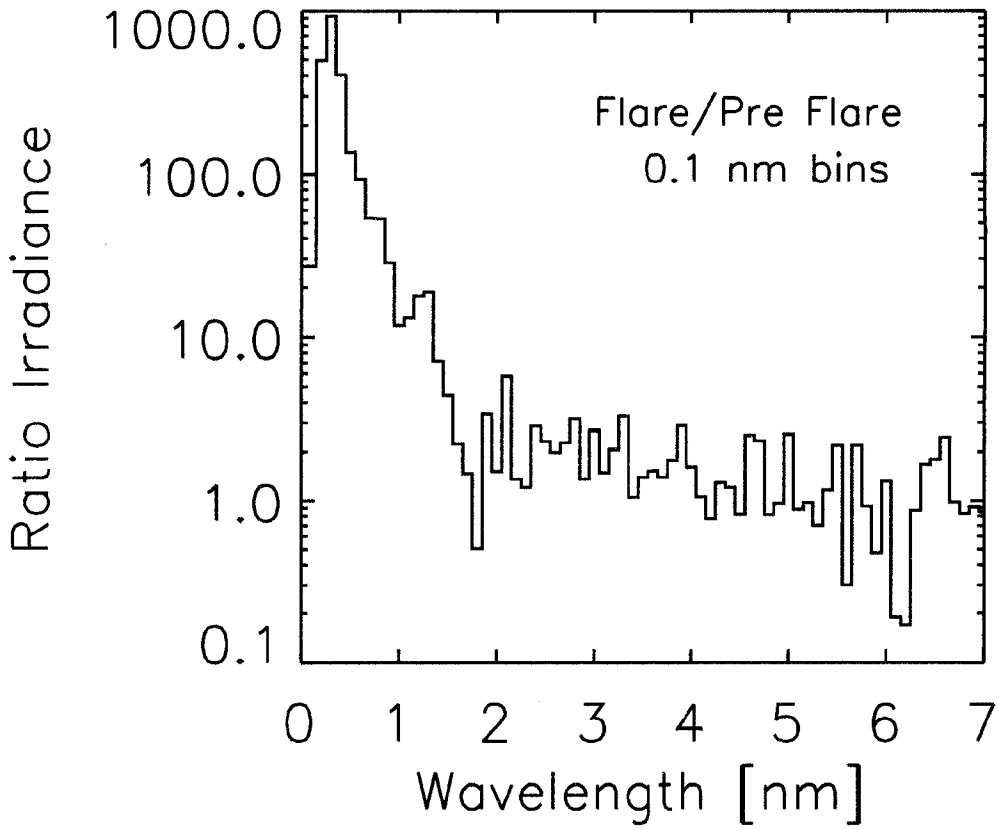

Figure 1.19 Ratio of 21 April 2002 X1.6 solar flare soft X-ray irradiance to pre-flare quiet-Sun soft X-ray irradiance shown in Figure 1.9. The 0.1-2 nm irradiance, which dominates the X1.6 solar flare spectrum (Figure 1.18), is found to be up to a factor of 10 higher than the pre-flare spectrum in the 1-2 nm range and up to a factor of 1000 higher than the pre-flare spectrum in the 0.1-1 nm range.

nm irradiance and up to a factor of 1000 higher than the pre-flare spectrum in the 0.1-1 nm irradiance. The solar flare spectrum varies significantly in both spectral shape and magnitude as compared to a quiet-Sun spectrum.

1.7. Solar Soft X-ray Irradiance Impact on Earth's Atmosphere

Solar irradiance below 310 nm is absorbed at different altitudes in Earth's atmosphere because atmospheric constituents (O, O_2, N_2, and O_3) absorb radiation at different wavelengths, as shown in Figure 1.20a [Lean, 1997]. Figure 1.20a shows the altitude of unit vertical optical depth where the solar irradiance is absorbed. Solar soft X-rays (0.1-30 nm) are absorbed in Earth's lower thermosphere between 80-150 km and provide a strong, variable energy source for this region of the upper atmosphere. Soft X-rays are primarily absorbed by N_2, O_2, and O and ionize these major neutral constituents of the terrestrial upper atmosphere. The photoionization rate, $P(z)$, at a certain altitude, z, is determined by the number density and ionization cross-section of the major neutral constituents at that altitude. For each neutral constituent,

$$P(z) = n(z)\sigma^i(\lambda)f_0(\lambda)\exp[-\tau(\lambda,z)] \quad \text{(ionizations s}^{-1}\text{ cm}^{-3}\text{)}, \tag{1.1}$$

where $n(z)$ is the number density (cm^{-3}) of O, O_2, or N_2, $\sigma^i(\lambda)$ is the ionization cross-section (cm^2), the probability of ionization by O, O_2, or N_2, $f_0(\lambda)$ is the solar irradiance (photon s^{-1} cm^{-2}), and $\tau(\lambda,z)$ is the optical depth (unitless). In the absence of scattering, the optical depth is given by

$$\tau(\lambda,z) = \sec(\phi)\left[N_O(z)\sigma_O^a(\lambda) + N_{O_2}(z)\sigma_{O_2}^a(\lambda) + N_{N_2}(z)\sigma_{N_2}^a(\lambda)\right], \tag{1.2}$$

where ϕ is the path angle, $N(z)$ is the column density (cm^{-2}) of O, O_2, or N_2 above altitude z, and $\sigma^a(\lambda)$is the respective absorption cross-section (cm^2).

Soft X-rays photoionize the major neutral constituents and produce photoelectrons through the following reaction,

$$M + h\nu \rightarrow M^+ + e^*, \tag{1.3}$$

where M is a molecule (N_2, O_2) or an atom (O), $h\nu$ is the photon energy, M^+ is the ionized molecule or atom, and e^* is a photoelectron. The ionization threshold energies (wavelengths) required to photoionize O_2, O, and N_2 are 12.08 eV (102.6 nm), 13.61 eV

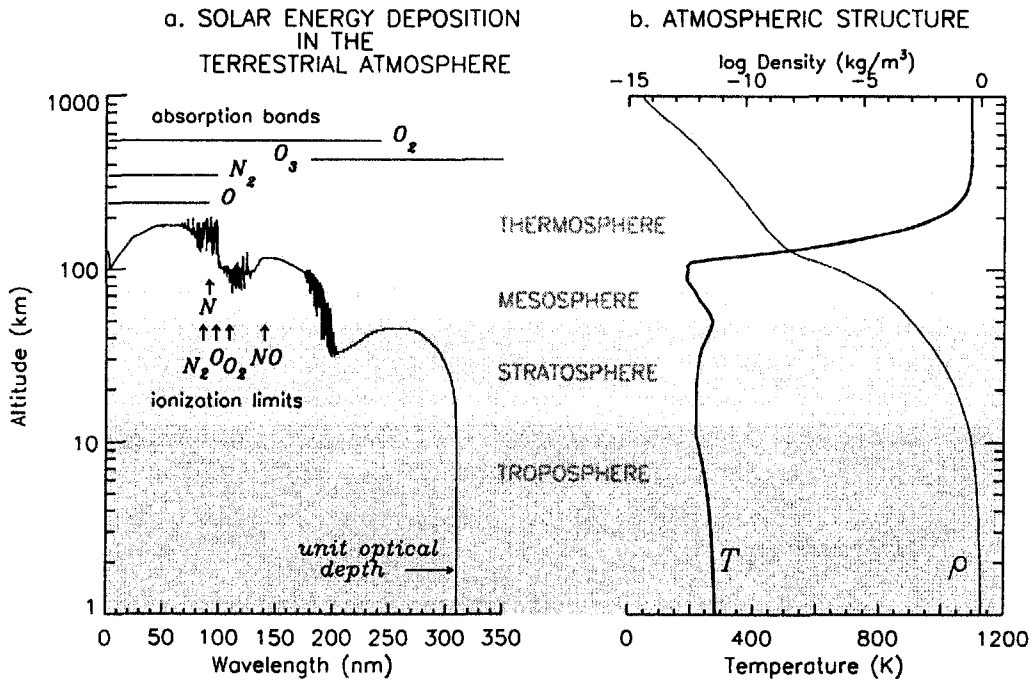

Figure 1.20 Solar irradiance below 310 nm is absorbed at different altitudes in Earth's atmosphere because atmospheric constituents absorb radiation at different wavelengths. Soft X-rays (0.1-30 nm) deposit their energy between 80-150 km in the thermosphere. a) The altitude of vertical unit optical depth where the solar irradiance is absorbed. b) The temperature and density of the atmosphere are determined by the deposited solar radiation. Figure from Lean [1997].

(91.1 nm), and 15.58 eV (79.6 nm), respectively [Rees, 1989]. Solar photons with high energies, such as soft X-rays (12.4-0.04 keV, 0.1-30 nm), have more energy than is required to ionize, and the extra energy is channeled into kinetic energy carried by the electron released in the ionization. This energetic electron is called a photoelectron and has an energy equal to the extra energy left over from the initial photon that caused the ionization. It is primarily this process of photoionization that produces the ionosphere [Rees, 1989]. Photoelectrons produced through soft X-ray photoionization produce primarily E-region ionization, which peaks near 105 km with ionization between 95-150 km and part of the D-region ionization, which peaks near 90 km with ionizations between 75-95 km, as shown in Figure 1.21. Figure 1.21 shows the altitudes where soft X-rays deposit their energy in the thermosphere thus forming the ionosphere. Higher energy, shorter wavelength, soft X-rays (2.5 keV-827 eV, 0.5-1.5 nm) deposit their energy between 90-110 km, moderately energetic soft X-rays (177-130 eV, 7-9.5 nm) deposit their energy between 115-120 km, and less energetic soft X-rays (62-41 eV, 20-30 nm) deposit their energy between 140-150 km. Figure 1.21 shows the individual absorption profiles (black) calculated for seven different soft X-ray wavelengths, and the total soft X-ray absorption (blue), which defines the D- and E-regions of the ionosphere.

Photoelectrons can react with other thermospheric constituents to cause further ionization, dissociation and excitation through the following three processes, respectively,

$$e^* + M \rightarrow M^+ + e^* + e^- \tag{1.4}$$

$$e^* + M \rightarrow M + M + e^* \tag{1.5}$$

$$e^* + M \rightarrow M^* + e^*, \tag{1.6}$$

where e^* is a photoelectron, M is a molecule (N_2, O_2) or an atom (O), M^+ is the ionized molecule or atom, M^* is the excited molecule or atom, and e^- is an electron. Each photoelectron collision leads to ionization (1.4), dissociation (1.5), excitation (1.6), or any combination of collisions, all of which continually reduce the energy of the original photoelectron as kinetic energy is transferred to the molecules and atoms of the thermosphere. Heating the neutral constituents is a direct consequence. Photoelectrons

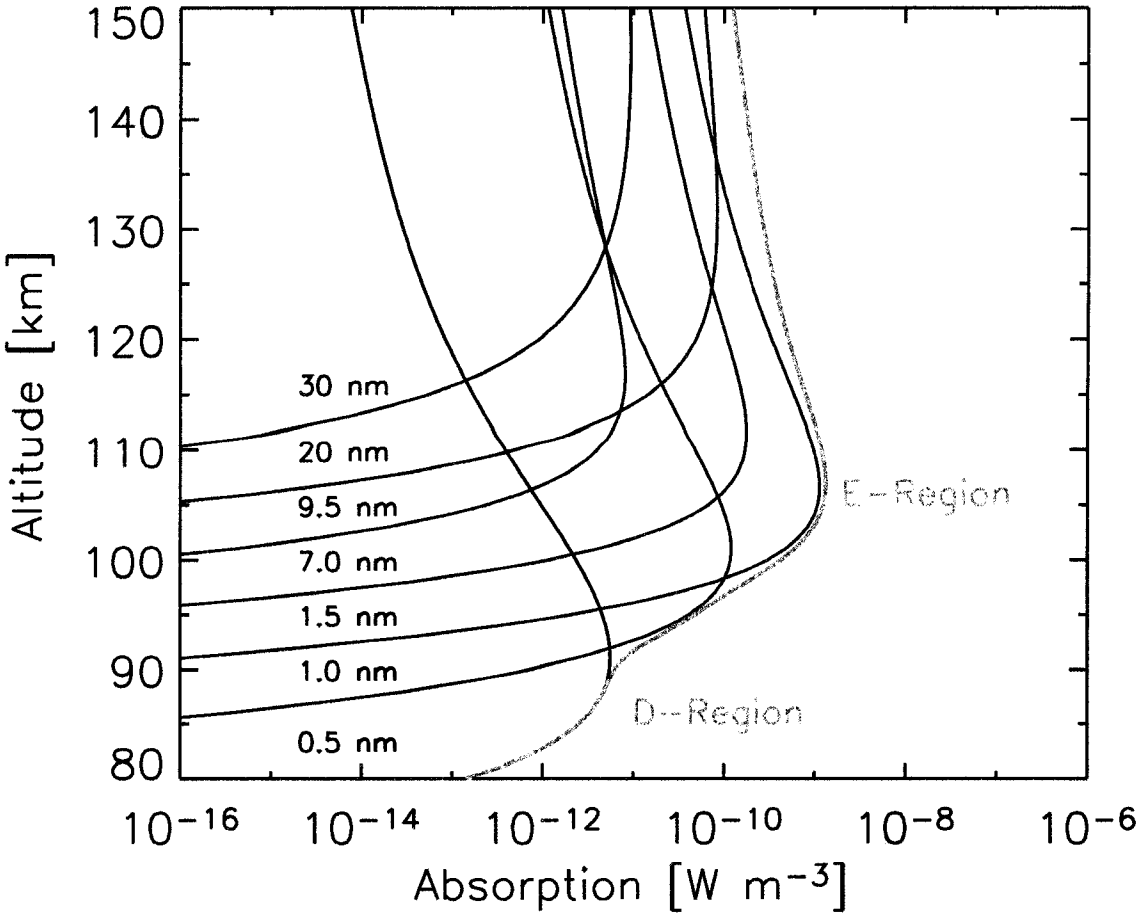

Figure 1.21 Altitudes where soft X-rays deposit their energy in the thermosphere to form the D- and E-regions of the ionosphere. Higher energy, shorter wavelength, soft X-rays (2.5 keV-827 eV, 0.5-1.5 nm) deposit their energy between 90-110 km, moderately energetic soft X-rays (177-130 eV, 7-9.5 nm) deposit their energy between 115-120 km, and less energetic soft X-rays (62-41 eV, 20-30 nm) deposit their energy between 140-150 km. The individual absorption profiles (black) are defined for seven different soft X-ray wavelengths, and the total soft X-ray absorption (blue) defines the D- and E-regions of the ionosphere.

give up energy until they are thermalized and have energies appropriate to the local thermospheric temperature.

Therefore, absorption of soft X-rays changes the composition and structure of the upper atmosphere through primary and secondary processes. The temperature and density profiles of the thermosphere are determined to a large extent by the deposited solar radiation, as was shown in Figure 1.20b. Because the soft X-ray irradiance varies, as described in Section 1.4.3, the thermospheric temperature and density also vary. An increase in soft X-ray photons leads to an increase in photoionization that leads to an increase in the photoelectron production, which lead to increased collisions that increase the temperature of the thermosphere [Rees, 1989]. The temperature can increase up to 50% for altitudes less than 150 km during the 11-year solar magnetic cycle, and as the thermosphere is heated, the mass and electron densities also increase [Lean, 1997]. Thermospheric temperature and density fluctuations also occur on intermediate timescales such as the 27-day solar rotation, and short-term variations lasting minutes to hours occur during a flare.

During a solar flare, the overall soft X-ray irradiance is increased and the 0.1-2 nm region dominates the spectrum (Figure 1.18). Thus, the magnitude and spectral shape are different than during quiet-Sun conditions. Since 0.1-2 nm soft X-ray photons are deposited between 80-115 km, a solar flare can rapidly modify the energy input to this region of the lower thermosphere. An increased number of soft X-rays result in an increase in photoionization and photoelectron production, which leads to an increase in the temperature, electron density, and modifications in the overall composition and structure of the D- and E-regions of the ionosphere.

As the thermosphere is heated during a solar flare, it expands outward resulting in higher densities at higher altitudes [Lean, 1997]. This increased density can increase the drag on low-Earth orbiting satellites, causing short-term orbit perturbations and ultimately reducing the expected mission lifetimes. The SNOE satellite began to re-enter Earth's atmosphere following several large X-class solar flares that occurred over a two-week period during the fall of 2003, as shown in Figure 1.22. The increased

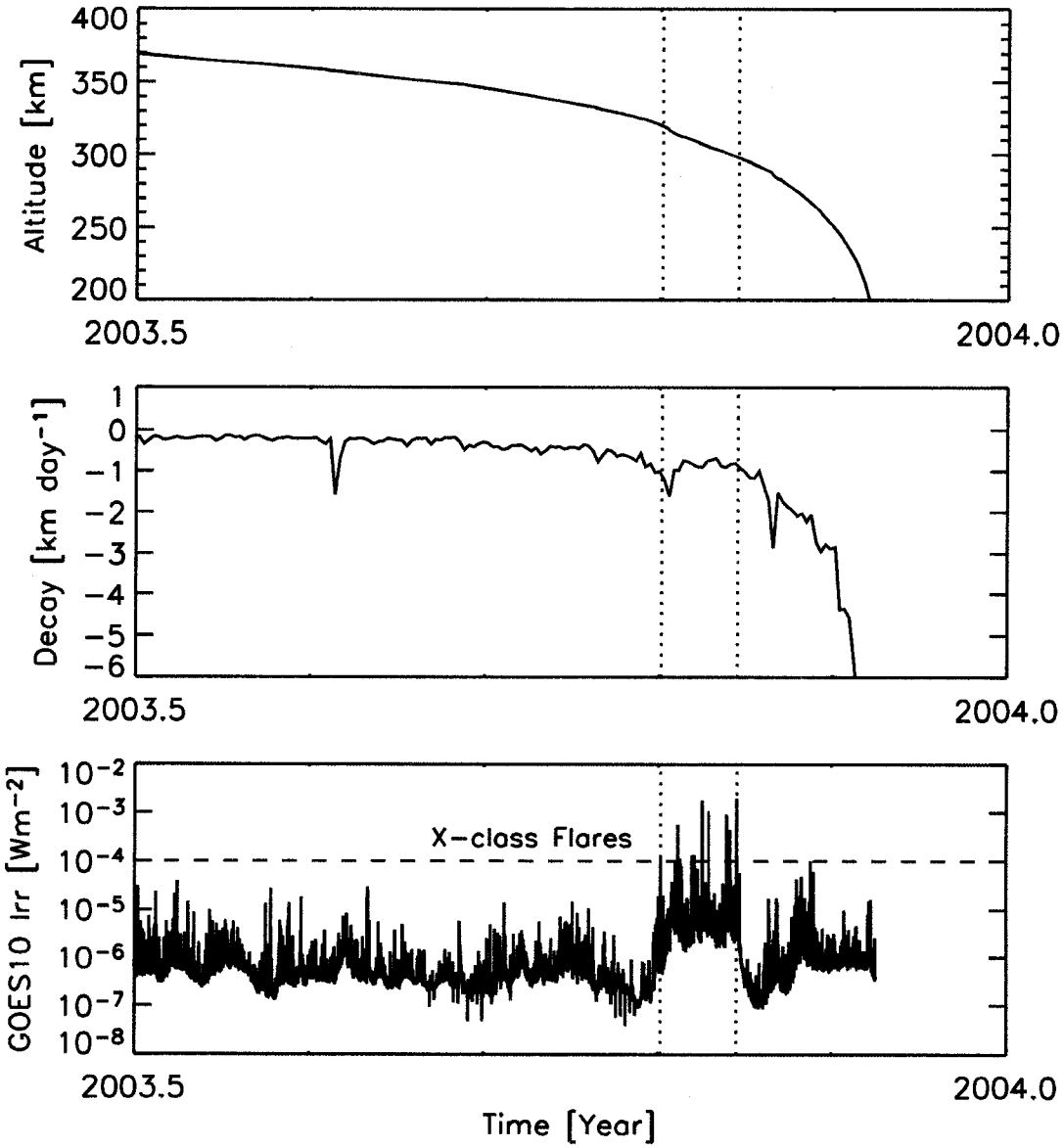

Figure 1.22 The SNOE satellite began to re-enter Earth's atmosphere following several large X-class solar flares that occurred over a two week period during the fall of 2003. [Top] SNOE altitude during the last five months of its lifetime. [Middle] SNOE decay rate during the last five months of its lifetime. [Bottom] GOES-10 irradiance over the same time period shows several large X-class solar flares occurred prior to the increased decay rate and decline in altitude of SNOE.

satellite decay rate caused an earlier than expected re-entry above the Pacific Ocean on 13 December 2003.

1.8. Nitric Oxide in the Thermosphere

The presence of nitric oxide (NO) in the upper atmosphere was first suggested in 1945 when Nicolet recognized that solar ionizing radiation is absorbed in the thermosphere above 100 km [Nicolet, 1945]. NO is a minor constituent of the thermosphere. However, it plays an important role in the energy balance of the thermosphere as it is a source of radiative cooling through infrared emissions. NO is primarily produced in the thermosphere through the reaction of excited atomic nitrogen, $N(^2D)$, with molecular oxygen, O_2,

$$N(^2D) + O_2 \rightarrow NO + O \tag{1.7}$$

Molecular nitrogen, N_2, is dissociated when energetic electrons break the strong N_2 bond and produce $N(^2D)$ through the following reaction,

$$N_2 + e^* \rightarrow 2N(^2D, ^4S) + e^* \tag{1.8}$$

The required energetic electrons come from two sources. First, solar soft X-rays are a global source of energy that produce photoelectrons, the primary energy driver for producing NO at low latitudes. Second, auroral electrons and energetic secondary auroral electrons provide the source of energy that leads to large amounts of NO at high latitudes.

Sunlight can also destroy NO. During the daytime, solar FUV irradiance between 150-180 nm provides a loss mechanism for NO through photodissociation,

$$NO + h\nu \rightarrow N(^4S) + O \tag{1.9}$$

This reaction produces ground state nitrogen, $N(^4S)$, which goes on to further destroy NO through another chemical reaction,

$$NO + N(^4S) \rightarrow N_2 + O \tag{1.10}$$

thus enhancing the effectiveness of photodissociation for destroying NO and removing odd-nitrogen [Bailey et al., 2002]. More complete discussions of NO production and loss mechanisms are described in Barth [1992] and Bailey et al. [2002].

NO emissions at 5.3 μm are a primary mechanism responsible for cooling the thermosphere as solar energy is converted to infrared radiation that transfers energy to space [Kockarts, 1980; Mlynczak et al., 2003]. The cooling effect is highly variable due to the variability of NO abundance and its strong temperature dependence [Kockarts, 1980]. Inelastic collisions with atomic oxygen, O, are the dominant excitation mechanism of NO vibrations during quiet times via

$$NO + O \rightarrow NO^{*} + O, \tag{1.11}$$

and when the excited NO relaxes to a lower state, an infrared photon (5.3 μm) is emitted

$$NO^{*} \rightarrow NO + h\nu \tag{1.12}$$

thus cooling the atmosphere [Mlynczak et al., 2003]. Four processes produce a change in the amount of radiation emitted by NO: 1) An increase in the NO abundance, leading to more collisions with O; 2) An increase in the kinetic temperature; 3) Exothermic production of vibrational levels of NO; and 4) increase in the atomic oxygen abundance [Mlynczak et al., 2003]. The thermospheric emission of radiation by NO is described in detail by Sharma and Duff [1997], Sharma et al., [1998], and Dothe et al., [2002].

1.8.1. NO Observations

Observations of thermospheric NO began in 1968 and were made by the Orbiting Geophysical Observatory (OGO-4). The fluorescent scattering of ultraviolet solar radiation by NO was observed by an ultraviolet spectrometer, and Rusch and Barth [1975] determined that the average NO concentration is higher at high latitudes than at midlatitudes. The AE C-D and Solar Mesospheric Explorer (SME) satellites made limb-scanning measurements of NO using florescent scattering [Barth et al, 1973; Barth, 1992]. SME NO measurements showed NO density to be highly variable between 100-120 km, and that low-latitude variation correlates with solar activity, while high-latitude variability correlates to magnetic activity [Barth, 1992]. More recently, the Halogen Occultation Experiment (HALOE) [Russell et al., 1993] and SNOE observations confirmed that thermospheric NO varies in both space and time, and that the maximum NO density occurs near 106-110 km [Barth et al., 2003].

Barth et al. [1988] first hypothesized that solar soft X-rays were the source of low-latitude thermospheric NO and the cause of thermospheric NO variability because soft X-rays are absorbed between 106-110 km where peak NO production occurs. Siskind et al. [1990; 1995] then calculated that there was a possible effect of soft X-rays on thermospheric NO. Simultaneous SNOE measurements of solar soft X-rays and thermospheric NO confirmed that soft X-ray irradiance between 0.1-7 nm is the primary low-latitude source of NO production with its maximum effect in the equatorial region at the subsolar point, but also influencing the entire illuminated hemisphere [Barth et al., 2003].

Figure 1.23a shows the correlation of equatorial SNOE NO at 106 km with soft X-rays between 0.1-7 nm for 935 days of observation beginning 11 March 1998. The correlation coefficient is 0.76, the slope is 9.2×10^7 cm^{-3} mW^{-1} m^2 and the y-intercept is 0.86×10^7 cm^{-3}. The NO density correlates well with the soft X-ray irradiance, indicating that soft X-rays (0.1-7 nm) lead to the production of thermospheric NO at low- and mid-latitudes [Barth et al., 2003]. Figure 1.23b shows the altitude profile of mean equatorial SNOE NO density during equinox periods of low, medium and high solar activity as defined by the F10.7 daily index between 20 March 1998 and 20 September 2000, which is shown in Figure 1.23c. The periods of solar activity are defined by F10.7 index values of less than 132, between 132 and 165, and greater than 165, and the mean equatorial NO density was calculated during each period for equinox plus and minus 15 days. The peak NO density at 110 km increases by approximately 20% from low to medium to high solar activity as shown in Table 1.5. Each altitude profile is proportional to the others between 97-123 km, indicating that soft X-rays are controlling the NO density in this altitude region, as soft X-rays directly correlate to the F10.7 index [Bailey et al., 2000; Barth et al., 2003].

SNOE observations also show that auroral electrons and energetic secondary auroral electrons produce high latitude NO [Barth et al., 2003]. The mean NO density is higher for auroral regions between 60°-70° geomagnetic latitude than for geographic equatorial regions. Figure 1.24a shows the altitude profile of mean auroral SNOE NO density

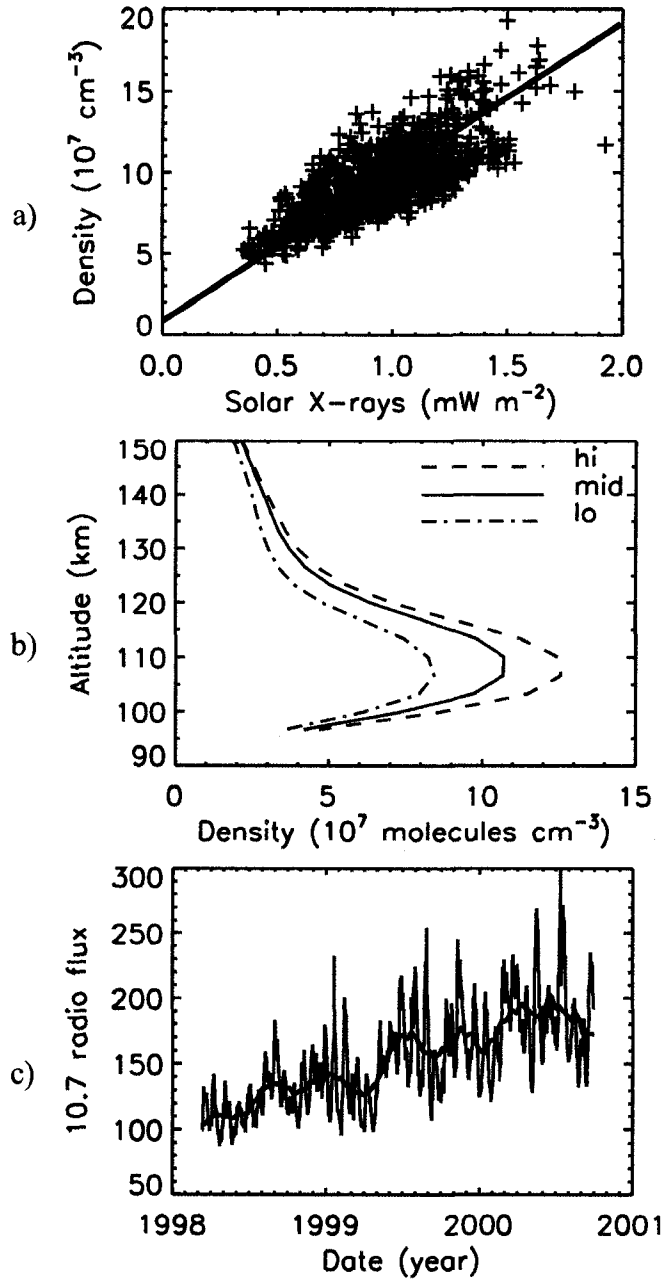

Figure 1.23 Soft X-ray irradiance between 0.1-7 nm is the primary low-latitude source of NO production. a) Correlation of equatorial SNOE NO at 106 km with soft X-rays (0.1-7 nm). b) Altitude profile of mean equatorial SNOE NO density for periods of low medium and high solar activity as defined by the F10.7 index. c) Corresponding F10.7 daily index and the 81-day F10.7 average. Figures from Barth et al. [2003].

Table 1.5 Mean equatorial NO density at 110 km for low, medium and high solar activity.

Solar Activity	F10.7	Mean Equatorial NO Density at 110 km [molecules cm^{-3}]
Low	90-132	8.0×10^{7}
Medium	132-165	1.1×10^{8}
High	165-300	1.3×10^{8}

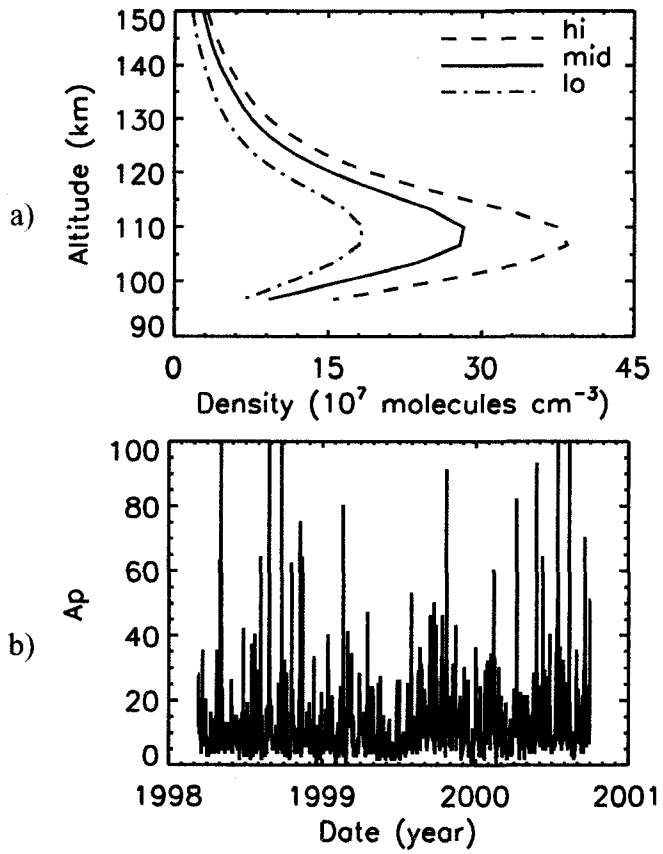

Figure 1.24 Auroral electrons and energetic secondary auroral electrons produce high latitude NO. a) Altitude profile of mean auroral SNOE NO density for periods of low, medium and high geomagnetic activity as defined by the Ap index. b) The corresponding Ap index during the SNOE observation period. Figures from Barth et al. [2003].

during equinox periods of low, mid and high geomagnetic activity as defined by the Ap index between 20 March 1998 and 20 September 2000, which was shown in Figure 1.24b. The periods of geomagnetic activity are defined from Ap index values of less than 6, between 6 and 12, and greater than 12, and the mean NO density was calculated during each period in the northern auroral region for equinox plus and minus 15 days. The peak NO density at 110 km increases by approximately 50% from low to medium to high geomagnetic activity as shown in Table 1.6. Each altitude profile is proportional to the others between 97-123 km, indicating that auroral electrons and energetic secondary auroral electrons are controlling the NO density in this altitude region.

The thermospheric NO density varies with geomagnetic activity, solar activity and time. Figure 1.25 shows the daily NO densities at an altitude of 106 km for two one-year periods beginning on 20 March 1998 and 1999. NO is more abundant in auroral regions between 60°-70° geomagnetic latitude than near the geographic equator. However, excess NO is carried to equatorial regions during periods of high geomagnetic activity by meridonal winds. Variations in equatorial NO are due to the variable soft X-ray irradiance. SNOE does not measure NO when the atmosphere is in darkness as is the case in the polar regions during winter solstices (days 172 and 355). Therefore, black regions at high latitudes are centered around winter solstices. NO is measured between 82°S and 82°N during equinox periods (days 079 and 266) when the atmosphere is illuminated between these latitudes. Minimum NO densities south of the equator occur during the late southern hemisphere fall and early winter, and minimum NO densities north of the equator occur during the late northern hemisphere fall and early winter [Barth et al., 2003].

SNOE observations of non-flare equatorial and auroral NO were compared to results from a time dependent photochemical model [Barth and Bailey, 2004]. This model predicts NO density as a function of altitude by using solar irradiance and auroral conditions as inputs. The SNOE daily soft X-ray irradiance between 0.1-7 nm was used for these comparisons. This model uses observed values of solar soft X-ray irradiance to describe the variability of NO in the equatorial region of the lower thermosphere. Daily

Table 1.6 Mean high latitude NO density at 110 km for low, medium and high geomagnetic activity.

Geomagnetic Activity	Ap	Mean High Latitude NO Density at 110 km [molecules cm^{-3}]
Low	0-6	$1.7x10^8$
Medium	6-12	$2.7x10^8$
High	12-100	$3.8x10^8$

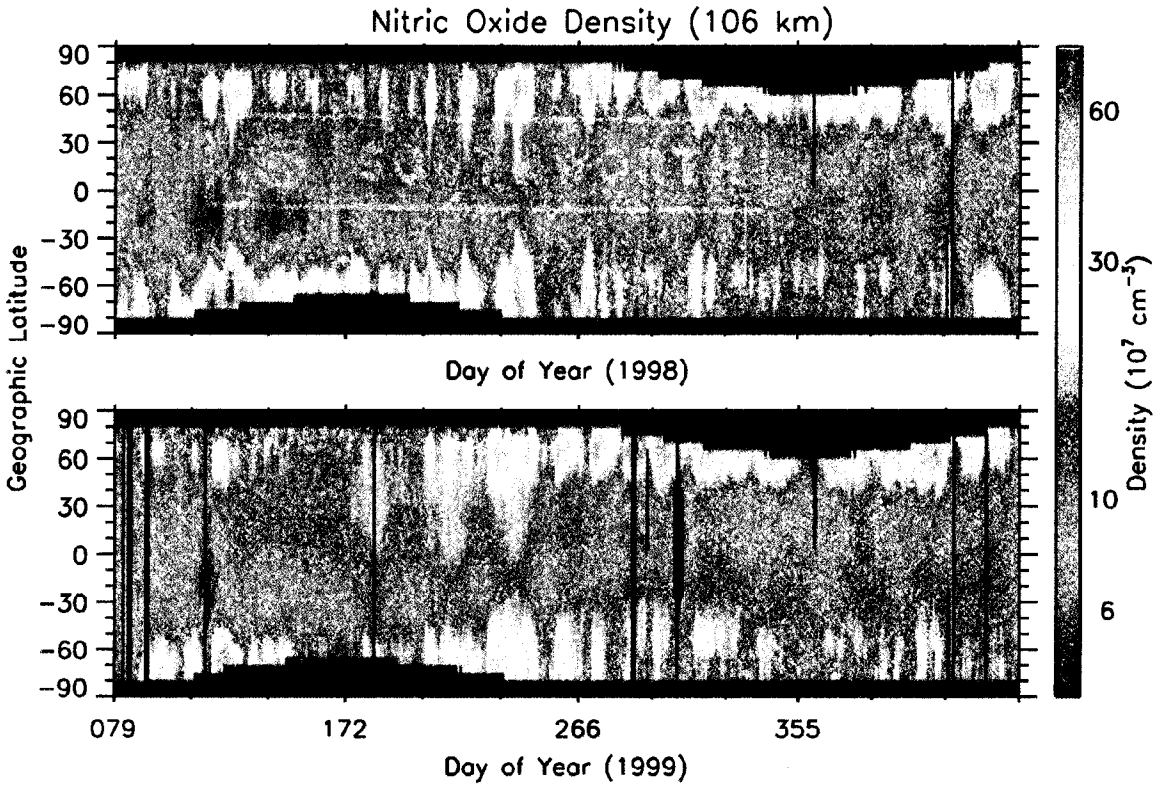

Figure 1.25 Daily NO densities at an altitude of 106 km for two one-year periods beginning on 20 March of 1998 and 1999. NO is more abundant in auroral regions between 60°-70° geomagnetic latitude than near the geographic equator. However, excess NO is carried to equatorial regions during periods of high geomagnetic activity by meridonal winds. Variations in equatorial NO are due to the variable soft X-ray irradiance. Minimum NO densities south of the equator occur during the late southern hemisphere fall and early winter, and minimum NO densities north of the equator occur during the late northern hemisphere fall and early winter. Figure from Barth et al. [2003].

changes in the 0.1-7 nm soft X-ray irradiance are accurately predicted by the model, with a high correlation between SNOE observations and model calculations for latitudes between 30°S and 30°N [Barth and Bailey, 2004]. Model comparisons confirm that auroral electrons and secondary auroral electrons between 65°-75° geomagnetic latitude are a large and varying source of thermospheric NO [Barth and Bailey, 2004]. NO produced in auroral regions can be transported equatorward by atmospheric transport during the fall-winter seasons, and can be transported all the way to the equator during large geomagnetic storms [Barth and Bailey, 2004].

1.8.2. Solar Flare Soft X-ray Irradiance Impact on Nitric Oxide Production

Solar soft X-rays are the primary source of photoionization and dissociation of molecular nitrogen (N_2) at low latitudes [Barth et al., 1988; Bailey et al., 1999b], which are important processes that lead to the production of thermospheric NO. SNOE observations of NO density and subsequent comparisons to a photochemical model show an understanding of the chemistry and how it relates to the energy sources that lead to thermospheric NO production during non-flare conditions. The equatorial density of NO peaks in the lower thermosphere near 110 km. NO has a lifetime of about one day in the thermosphere, and the rate of equatorial NO production responds linearly to the daily non-flare soft X-ray energy deposited at the peak altitude as shown in Figure 1.26. As the daily averaged non-flare soft X-ray irradiance doubles, the daily averaged equatorial NO density near 110 km also doubles. During a solar flare, the overall soft X-ray irradiance between 0.1-7 nm is increased and the 0.1-2 nm region dominates the spectrum (Figure 1.18). The excess of 0.1-2 nm soft X-rays leads to more photoelectrons near 110 km, which leads to more NO production at these altitudes, which then leads to increased cooling of the thermosphere due to infrared emissions. Siskind et al. [1995] first pointed out that 1-2 nm non-flare soft X-rays are important for the production of NO when a photochemical model that predicts NO density produced NO more efficiently when including 1-2 nm soft X-rays. Therefore, 1-2 nm photons are important to the production of thermospheric NO during non-flare times. The question

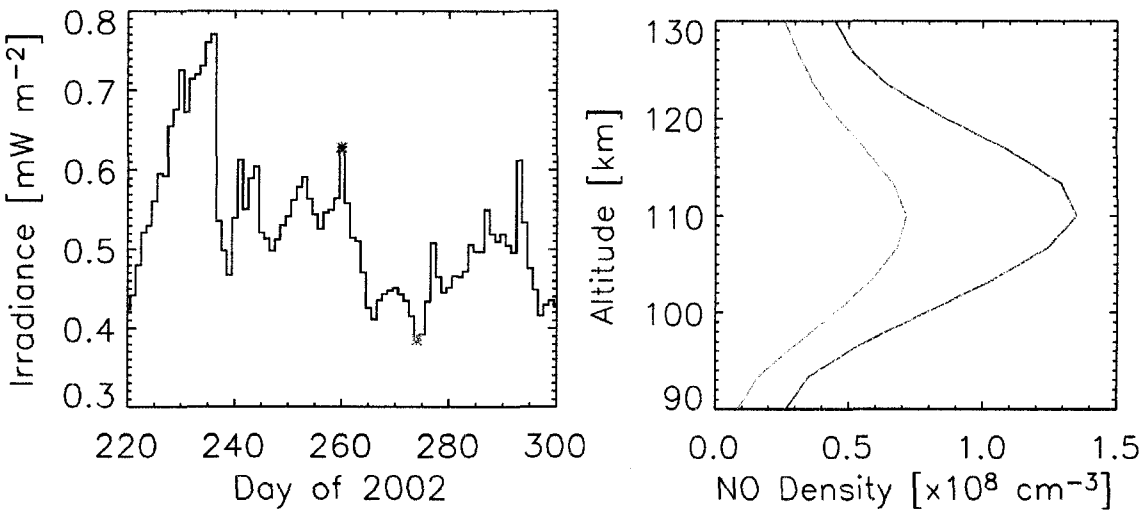

Figure 1.26 Equatorial density of NO peaks in the lower thermosphere near 110 km and responds linearly to the daily solar soft X-ray (0.1-7 nm) energy deposited at that altitude. [Left] Daily averaged soft X-ray irradiance as observed by the SEE XPS between days 220-300 (8 Aug-27 Oct) during 2002. The red star represents the soft X-ray irradiance on day 260, which is twice as much as the soft X-ray irradiance represented by the blue star on day 274. [Right] Daily averaged equatorial NO density for day 260 (red) and 274 (blue) shows the NO density near 110 km doubles when the daily averaged soft X-ray irradiance doubles.

remains of how much of an increase in thermospheric NO is observed and modeled when there is an increase in the 1-2 nm irradiance during a solar flare.

1.9. Overview of Dissertation

SNOE observations of NO density and subsequent comparisons to a photochemical model have resulted in an understanding of the chemistry and how it relates to the two energy sources that lead to thermospheric NO production during non-flare conditions. The next step is to understand the increase in low latitude NO density due to solar flare enhanced soft X-ray irradiance. This dissertation answers the following two questions: 1) What is the solar soft X-ray energy deposition into Earth's lower thermosphere during a solar flare and how does that energy deposition vary as a function of altitude? 2) What is the effect of this energy input on the NO density in the Earth's lower thermosphere? The first research question is answered through analysis of the XPS instruments aboard the TIMED-SEE and SORCE satellites. The second research question is answered through analysis of thermospheric NO observations from an instrument aboard SNOE.

XPS observations from SEE, beginning 22 January 2002 and SORCE, beginning 25 February 2003 are analyzed to determine the solar soft X-ray energy deposition to the Earth's upper atmosphere during a solar flare. The SEE XPS observed 102 flares of various strengths over a six-month period in 2002, and the SORCE XPS observed 16 large flares during the fall of 2003. The XPS detectors are broadband silicon photodiodes that observe from 0.1 to 34 nm. Both the photodiode sensitivities and the solar spectrum vary significantly within each detector bandpass. Therefore, analysis of XPS observations requires a reference spectrum to interpret the signals. There is no single reference spectrum available that can accurately be used for interpreting broadband signals during solar flares. A method to determine an accurate solar flare spectrum is described in this dissertation. The flare spectrum of individual observations is determined by interpreting the XPS observations of solar flares with a model that calculates theoretical spectra for input differential emission measures (DEMs). An algorithm iterates the DEMs until the resulting spectrum reproduces the XPS observations. This technique is applied to the 102 flares observed by the SEE XPS in

2002 and to the 16 observed by the SORCE XPS in 2003 to retrieve their spectra. These solar flare spectra are used to determine the soft X-ray energy input to the thermosphere during each flare.

A quantitative understanding of the energy deposited from flares is required to determine the terrestrial impacts of solar flares. The retrieved spectrum of one solar flare is input to an existing thermospheric NO model to calculate the predicted flare NO enhancements. Model results are compared to SNOE Ultraviolet Spectrometer (UVS) observations of this flare. The UVS observed thermospheric NO between 11 March 1998 and 31 October 2003. The NO density enhancements due to the integrated irradiance deposited during an additional ten flares are analyzed to determine the solar flare soft X-ray energy impact on the NO abundance.

Chapter 2 describes the SEE and SORCE XPS instruments, their calibrations, and their observations of solar flares. Chapter 3 describes the solar flare spectral analysis, including the model and algorithm, and retrieved solar flare spectra. Chapter 4 describes SNOE NO density observations of a solar flare, predicted NO density of the flare from a photochemical model and comparisons to observed SNOE NO density. Chapter 5 concludes this dissertation with a summary of results and applications for future research.

Chapter 2 Solar Flare Observations

2.1. Solar Soft X-ray Instrumentation

Solar flare irradiance measurements are made with two nearly identical XPS instruments currently in orbit about Earth. One instrument is aboard the TIMED satellite and the other is aboard the SORCE satellite. TIMED was launched on 7 December 2001 and SEE XPS solar observations began on 22 January 2002. SORCE was launched on 25 January 2003 and solar observations began on 25 February 2003. Solar irradiance observations of both XPS instruments continue today. The TIMED and SORCE satellites are both in low Earth orbits, but observe the Sun differently due to orbital inclination and other satellite operation requirements. The TIMED orbit has an inclination of 70° and the SEE XPS observes the Sun for 3 minutes within each 96-minute orbit. Solar flare observations from the first six months of operation are described in this work. Only the first six months are analyzed because a mechanical anomaly occurred that reduced the number of SEE XPS instrument channels [Woods et al., 2005a]. The SORCE orbit has an inclination of 40° and an orbital period of 97 minutes. The SORCE XPS makes solar observations for 40 minutes of each orbit. Solar flare observations from only a two-week period during the fall of 2003 are described in this work. Very large flares occurred during this time and SORCE observations are used to supplement and diversify SEE XPS observations of only a few large flares.

The XPS instrument has twelve photodiode channels, of which eight measure the solar irradiance in the soft X-ray wavelength range of 0.1 to 34 nm. Seven SEE soft X-ray photodiodes were used for analysis because one channel has a higher than normal background uncertainty. Three SORCE XPS soft X-ray photodiodes were used for analysis because they provide three unique quiet-Sun spectral bandpasses, and using the other photodiodes would be redundant. Section 3.4 provides a complete discussion. A filter wheel mechanism is located at the front of the instrument and each photodiode channel is mounted behind circular apertures defined by the filter wheel mechanism. Figure 2.1 shows the SORCE XPS instrument prior to satellite integration.

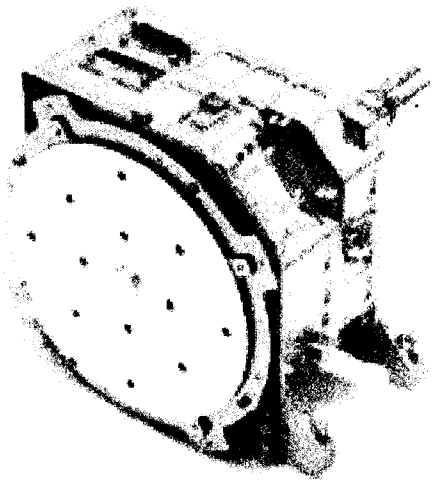

Figure 2.1 The SORCE XPS instrument prior to satellite integration. The XPS has twelve photodiode channels mounted behind a common filter wheel mechanism, of which eight channels observe soft X-rays between 0.1-34 nm. The SEE XPS is nearly identical to the SORCE XPS.

The individual SEE and SORCE XPS detectors are broadband silicon XUV photodiodes that are available commercially and designed to have low noise and good long-term stability [Korde and Geist, 1987; Korde et al., 1988; Canfield et al., 1989; Korde and Canfield, 1989; Canfield et al., 1994]. These silicon photodiodes are similar to those previously flown on sounding rockets by Ogawa et al. [1990] and Bailey et al. [1999a; 1999b], and on the Student Nitric Oxide Explorer (SNOE) satellite as described by Bailey et al. [2000; 2001; 2006]. Thin-film metallic coatings are deposited directly onto the active area of each photodiode to avoid using foil filters that can develop pinholes and degrade with time [Woods et al., 1999; 2005a; 2005b].

The filter coatings, calibrated coating thicknesses, and bandpasses of the SEE and SORCE XPS photodiodes are listed in Tables 2.1 and 2.2, respectively. The coatings are designed to have a narrow soft X-ray transmission band and to be thick enough to block any contribution from the much brighter, longer wavelength spectrum of the Sun [Bailey et al., 2000]. Visible light can be transmitted through microscopic pinholes in the filter coating or from around the edge of any photodiode active area and needs to be subtracted from the measurement. To do this, fused silica windows, with a short wavelength cutoff of approximately 300 nm, can be rotated in front of the individual photodiode detectors housed in the filter wheel mechanism to permit accurate subtraction of the background signal from visible light [Woods et al., 2005a; 2005b]. Filter wheel rotation between three different positions permits three different measurements to be made: soft X-ray measurements behind clear apertures, dark measurements behind blocked apertures, and visible background measurements behind fused silica windows [Woods et al., 2005a; 2005b].

The metallic coating material and thickness, in conjunction with the response of a bare (uncoated) photodiode, determines the wavelength region of sensitivity for each detector [Bailey et al., 2000; 2001]. The calibrated sensitivities and calibrated coating thicknesses of the SEE XPS flight photodiodes were determined using the Physikalisch-Technische Bundesanstalt (PTB) electron storage ring called BESSY, and the calibrated sensitivities and calibrated coating thicknesses of the SORCE XPS flight photodiodes

Table 2.1 TIMED-SEE XPS photodiode parameters.

XPS Channel	Filter Coating	Calibrated Thickness [nm]	Quiet Sun Conditions		Solar Flare Conditions	
			Bandpass [nm]	% Total Signal	Bandpass [nm]	% Total Signal
1	Ti / C	496 / 45	0.1-7	98.7	0.1-2	88.5
2	Ti / C	482 / 48	0.1-7	98.7	0.1-2	88.5
5	Ti / Pd	229 / 79	0.1-10	99.9	0.1-2	86.0
6	Ti / Zr / Au	59 / 204 / 100	0.1-10	99.5	0.1-2	95.9
7	Al / Nb / C	374 / 50 / 56	0.1-7	69.1	0.1-2	94.9
			17-21	30.0		
9	Al / Mn	187 / 60	0.1-10	82.4	0.1-2	88.1
			25-34	13.2		
10	Al / Cr	195 / 60	0.1-7	92.3	0.1-2	92.5
			28-34	6.5		

Table 2.2 SORCE XPS photodiode parameters.

XPS Channel	Filter Coating	Calibrated Thickness [nm]	Quiet Sun Conditions		Solar Flare Conditions	
			Bandpass [nm]	% Total Signal	Bandpass [nm]	% Total Signal
2	Ti / C	387.5 / 50	0.1-7	98.7	0.1-2	90.6
3	Al / Sc / C	179.1 / 50 / 25	0.1-7	54.8	0.1-2	90.7
			17-25	43.7		
6	Ti / Mo / Au	45.2 / 111.3 / 74.1	0.1-10	99.6	0.1-2	94.6

were determined using the National Institute for Standards and Technology Synchrotron Ultraviolet Radiation Facility (NIST-SURF III) facility. The SEE XPS photodiode sensitivity calibrations were performed from 0.8-25 nm [Woods et al., 1999] and the SORCE XPS photodiode sensitivity calibrations were performed from 4.5-21 nm [Woods et al., 2005b]. Sensitivity outside of the calibration wavelength ranges is modeled based on filter coating material absorption coefficients [Henke et al., 1982; 1988; 1993], and the known sensitivity of a bare (uncoated) photodiode [Korde and Canfield, 1989; Canfield et al., 1994], where an uncoated photodiode produces one electron per 3.63 eV of incident photon energy. Figures 2.2 and 2.3 show the photoelectron yield of the SEE and SORCE XPS photodiodes. The calibrated coating thicknesses are determined from a least squares fit between the model and measured sensitivities [Woods et al., 1999; 2005b]. A complete discussion of all calibration results for SEE and SORCE can be found in Woods et al. [1999] and Woods et al. [2005b], respectively.

The sensitivity of each broadband detector channel varies within each photodiode wavelength bandpass, and the wavelengths of their peak sensitivity are different, as shown in Figures 2.2 and 2.3. It is not easily known which soft X-ray wavelengths contribute the most to the total photodiode signal. For this reason, a reference spectrum is required to interpret the photodiode signal. An individual channel's response, i_k, is determined by convolving a quiet-Sun reference spectrum [Warren et al., 2001] or a solar flare spectrum with the sensitivity of each coated photodiode, [Woods et al., 1999; 2005b] in order to calculate a photodiode model signal (current) per wavelength interval:

$$i_k(\Delta\lambda,\lambda) = \int_{\lambda}^{\lambda+\Delta\lambda} S_k(\lambda)F(\lambda)q_e A_k d\lambda \quad \text{(A)}. \tag{2.1}$$

$S_k(\lambda)$ is the sensitivity (e^- ph^{-1}) of each photodiode, k, $F(\lambda)$ is the quiet-Sun irradiance shown in Figure 1.9 at wavelength λ (Å), q_e is the charge of an electron (C e^{-1}) and A_k is the area (cm^2) of the photodiode, k, that is illuminated through its aperture. Each XPS detector channel observes the Sun and measures a total current that is representative of

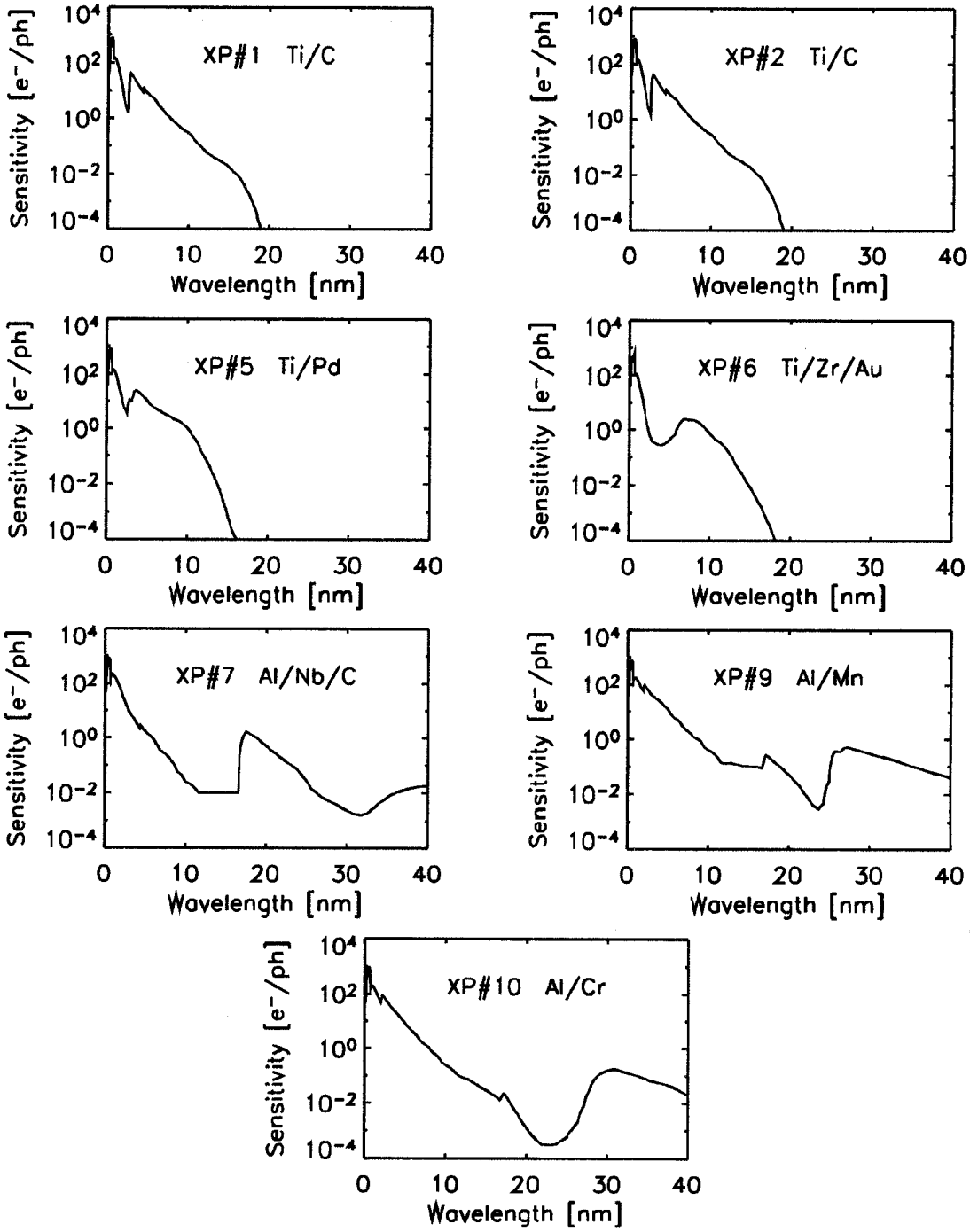

Figure 2.2 Photoelectron yield of SEE XPS coated photodiodes from 0.1-40 nm.

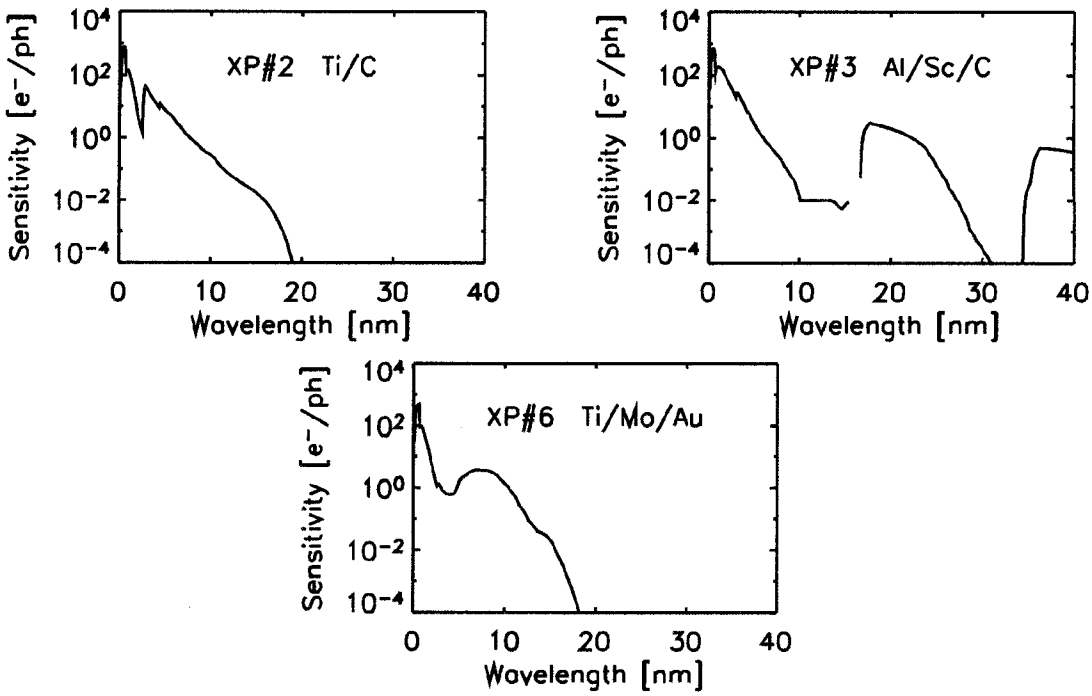

Figure 2.3 Photoelectron yield of SORCE XPS coated photodiodes from 0.1-40 nm.

the entire detector wavelength bandpass. The photodiode model current per wavelength interval ($\Delta\lambda$ at λ) calculated from Equation 2.1 is divided by the total measured current for each photodiode, k, to determine the fraction of current per wavelength interval or the percent of total current per wavelength interval. The effective bandpass is then defined as the wavelength region where the highest percentage of the signal is produced. These percentages were defined in Tables 2.1 and 2.2 along with the spectral bandpasses for modeled quiet-Sun conditions. The modeled quiet-Sun photodiode spectral relative responses are shown in 1 nm wavelength bins for the SEE XPS in Figure 2.4 and for the SORCE XPS in Figure 2.5.

The photodiode spectral relative responses vary with wavelength for each photodiode channel, and some photodiode channels have overlapping responses. Generally, over 50% of the total current comes from the 0.1-10 nm wavelength range during quiet-Sun conditions, and approximately 20% of the current is shortward of 2 nm. There are three significant quiet-Sun spectral bandpasses, 0.1-7 nm, 7-10 nm, and 17-21 nm for the SEE XPS photodiodes, and 0.1-7 nm, 7-10 nm, and 17-25 nm for the SORCE XPS photodiodes. The 25-34 nm and 28-34 nm bandpass ranges for two of the SEE XPS photodiodes comprise only 13.2% and 6.5% of the total current, respectively, and are therefore not considered significant spectral bandpasses.

The reference spectrum assumed in standard SEE and SORCE data reduction is appropriate for quiet-Sun conditions, but this solar soft X-ray irradiance differs significantly both in magnitude and spectral shape from the irradiance during solar flare conditions, as was indicated in Figures 1.15 and 1.16. The 0.1-2 nm irradiance is small during quiet-Sun conditions, but during flare conditions it can be equal to or greater than the irradiance at 20 nm. This is important for the SEE and SORCE XPS because the photodiode sensitivities peak between 0.1-2 nm, and when this region of the spectrum is enhanced, as occurs during flares, the photodiode current may become dominated by the short-wavelength contribution. The percent of total current was determined for each photodiode using Equation 2.1 and the method previously described, but using for $F(\lambda)$ the solar flare spectrum shown in Figure 1.15. The SEE and SORCE XPS photodiode

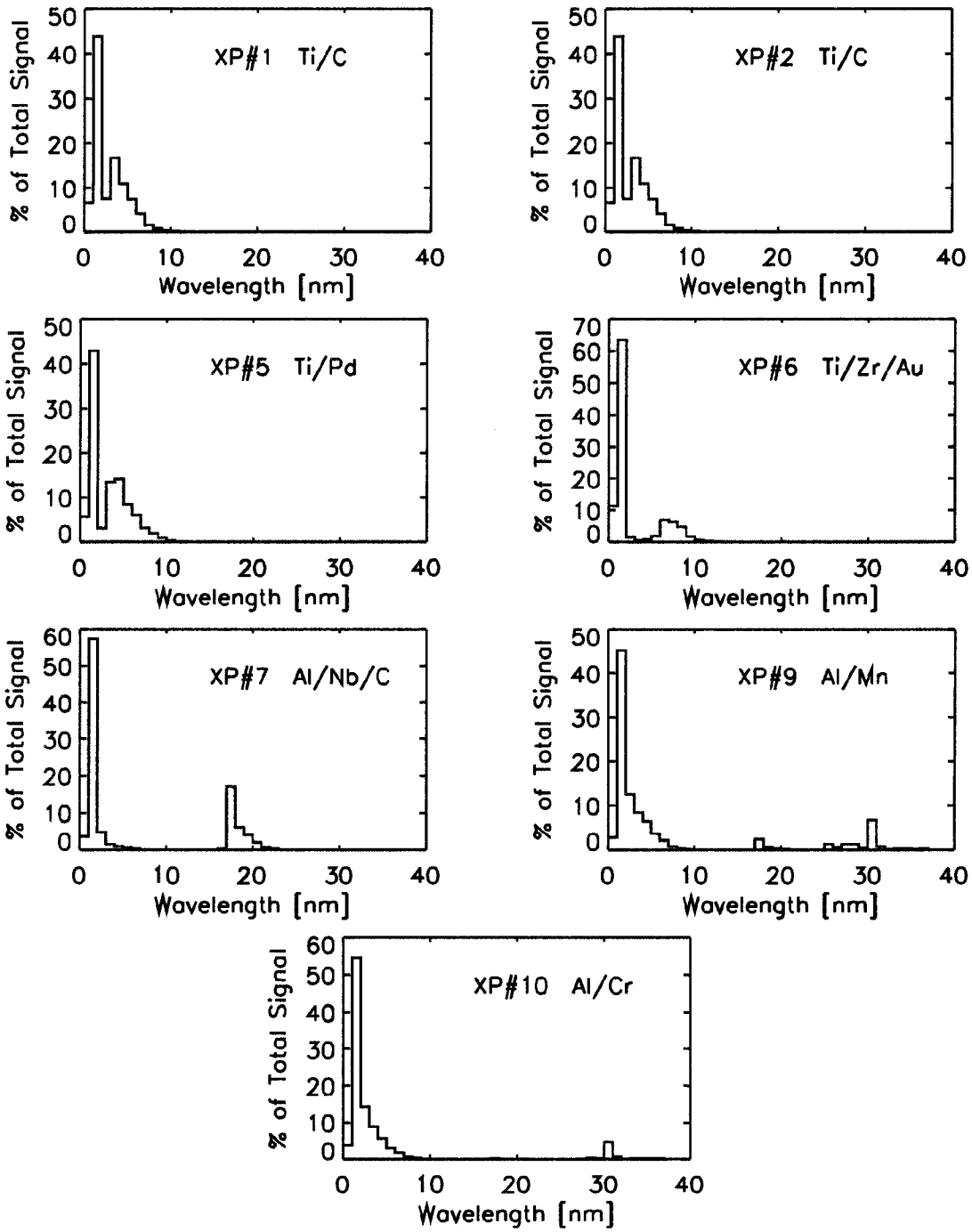

Figure 2.4 SEE XPS photodiode spectral relative responses for modeled quiet-Sun conditions in 1 nm wavelength bins.

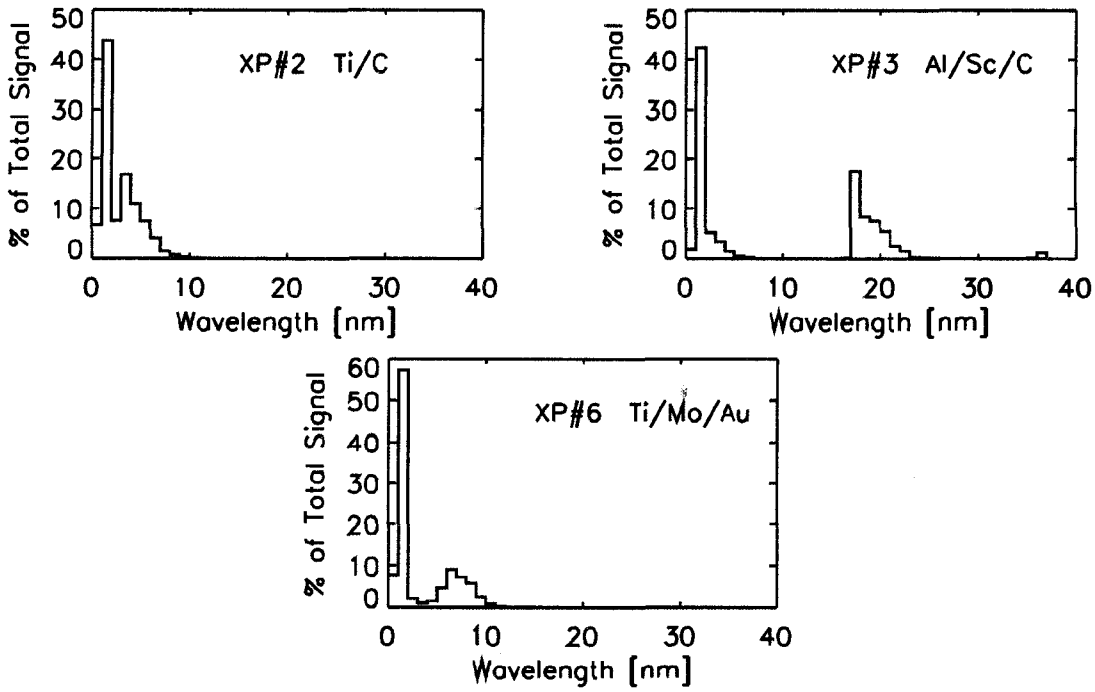

Figure 2.5 SORCE XPS photodiode spectral relative responses for modeled quiet-Sun conditions in 1 nm wavelength bins.

percents of total current and their spectral relative responses during a solar flare are shown in Figures 2.6 and 2.7, respectively. The spectral bandpasses for modeled solar flare conditions are also listed in Tables 2.1 and 2.2. Over 86% of the total current comes from the 0.1-2 nm wavelength range for all photodiodes during solar flare conditions. This compares with approximately 20% for the quiet-Sun irradiance.

Without a reliable reference spectrum or an independent spectral measurement, it is not possible to determine the relative contribution as a function of wavelength. Solar soft X-rays deposit their energy in Earth's lower thermosphere between 80-150 km, where the absorption efficiency of the atmosphere varies strongly with wavelength. For example, highly energetic photons in the 0.1-2 nm wavelength range (12.4 keV-620 eV), which are numerous during solar flares, deposit their energy at a lower altitude (80-115 km) than do 20 nm (62 eV) photons (140 km). It is important to use a reference spectrum that accurately reflects solar flare conditions; otherwise, the spectral relative response is incorrect, which then leads to a misrepresentation of the altitudes at which the energy is absorbed. Solomon et al., [2005] illustrate this point by demonstrating that a spectrum which takes into account flare conditions leads to a more realistic atmospheric response during flares than do the standard SEE and SORCE XPS reference spectra. No single spectrum is currently available that can accurately serve as a reference spectrum for interpreting broadband signals during solar flares. Chapter 3 describes a forward model of a flare spectrum used in an iterative approach to determine a realistic flare spectrum to interpret broadband signals. An example of one such retrieved flare spectrum was shown in Figure 1.15 and used previously in this section to convolve with the photodiode sensitivities when determining the spectral relative response of each photodiode.

2.2. XPS Solar Observations

Observations with individual photodiodes are made at different times with different filter wheel positions, allowing the detectors to make relevant observations: dark signal behind a blocked aperture; visible background signal behind a fused silica window; and solar soft X-ray irradiance behind a clear aperture [Woods et al., 2005a; 2005b].

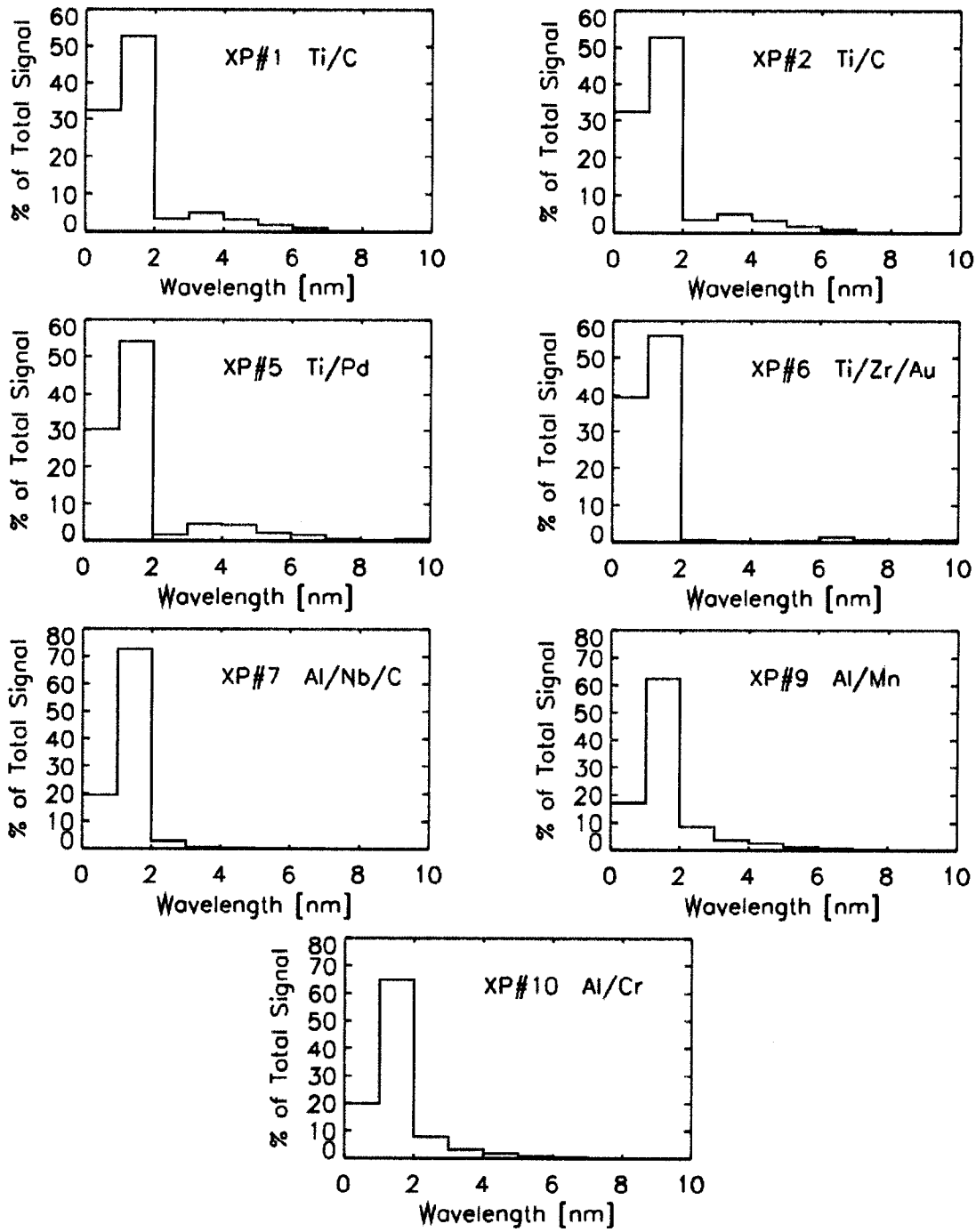

Figure 2.6 SEE XPS photodiode spectral relative responses for modeled solar flare conditions in 1 nm wavelength bins.

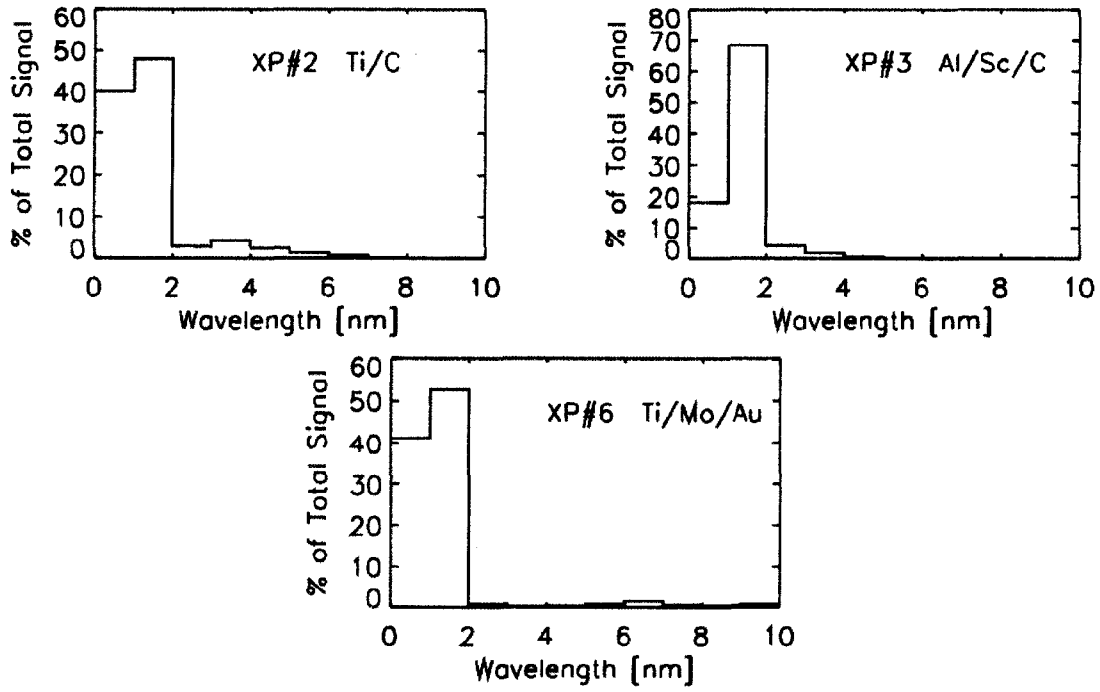

Figure 2.7 SORCE XPS photodiode spectral relative responses for modeled solar flare conditions in 1 nm wavelength bins.

Observations with individual SEE XPS photodiodes take place during 20-second intervals after which the filter wheel rotates quickly to the next location. Observations are made continuously for approximately 3 minutes of each orbit. In comparison, SORCE XPS photodiode observations are made during 50-second intervals before the filter wheel rotates to the next location. SORCE XPS observations are made continuously for approximately 40 minutes of each orbit.

As a result of the rotating filter wheel, the photodiodes sense the solar irradiance and measure a current at sequentially different times. The measurement of each photodiode detector channel were extrapolated onto the time grid of a selected XPS channel so that all photodiode measurements are referenced to one time grid. The SEE XPS channel #2 and SORCE XPS channel #3 time grids were chosen as the reference time grids for interpolation of the SEE and SORCE detectors, respectively. These detector channels were chosen because of their stable background current and because they reflect the sequential median time grid of all respective XPS channels.

Solar flare observations are characterized by a rise and fall in measured photodiode current. The XPS current measurements were analyzed for discrete increases that would be considered flare enhancements above the background. Solar flares were identified by extracting flare enhancements from the observed XPS signals by subtracting the background current from the measured current. The background current was defined as the daily average of the smallest 20% of all current measurements over that one-day interval. Calculating the daily average of all current measurements would include non-flare and flare times that can occur during the same one-day interval. Including flare observations can increase the background current uncertainty by up to about 60% depending on the photodiode channel. A flare is flagged when two criteria are met: 1) The signal produces a 3-σ increase above the background signal, where σ is one standard deviation of variation in the background current distribution over that one-day interval; and 2) The 3-σ signal increase must be observed by all photodiode channels. All flares were flagged by some photodiodes, while other photodiodes may not flag all of the observed flares due to the differences in the signal and backgrounds of each

detector. A 3-σ increase usually corresponds to about a 30% increase above the average signal for a given day.

The SEE XPS photodiode makes three measurements during its 20-second solar observation period, and the SORCE XPS makes six measurements during its 50-second solar observation period. The maximum measured flare current during each solar observation period was used as a data point for analysis. Depending on its position in orbit, the SORCE XPS may observe a single flare several times during the lifetime of the flare, whereas the SEE XPS may observe a single flare only once during the lifetime of the flare, due to the lower time cadence of SEE observations. Several SORCE XPS data points may be identified for each flare, but the maximum observed current for each flare is identified as the single solar flare observation and studied.

A total of 102 solar flares observed by all SEE XPS photodiodes were identified in this way. Figure 2.8 displays the time series of SEE XPS observations during a six-month period in 2002 for all photodiode channels. The background current is highlighted in red and the green diamonds represent the peak of the 102 observed solar flares. The background error, highlighted in dashed orange, is one standard deviation of the variation in the background current distribution over a one-day period. The flare signals can be seen as discrete events on top of a smoothly varying background. These discrete events are interpreted to be solar flares. Each photodiode channel detects a different number of solar flares due to the detector's different sensitivity. The brightest flares were identified by all detector channels, and these 102 flares were considered for this study. The background current subtracted from the peak measured current is the flare current. The flare currents have average absolute uncertainties of 0.12 nA for channel 1, 0.12 nA for channel 2, 0.36 nA for channel 5, 0.23 nA for channel 6, 0.31 nA for channel 7, 0.14 nA for channel 9, and 0.15 nA for channel 10.

The SORCE XPS observed 16 solar flares of various intensities during the fall of 2003. Figure 2.9 displays the time series of all photodiodes. Many of these 16 flares are bright X-class flares, thus allowing for analysis of a diverse range of solar flares since the SEE XPS observed more flares of dim to medium intensity. The background current

a)

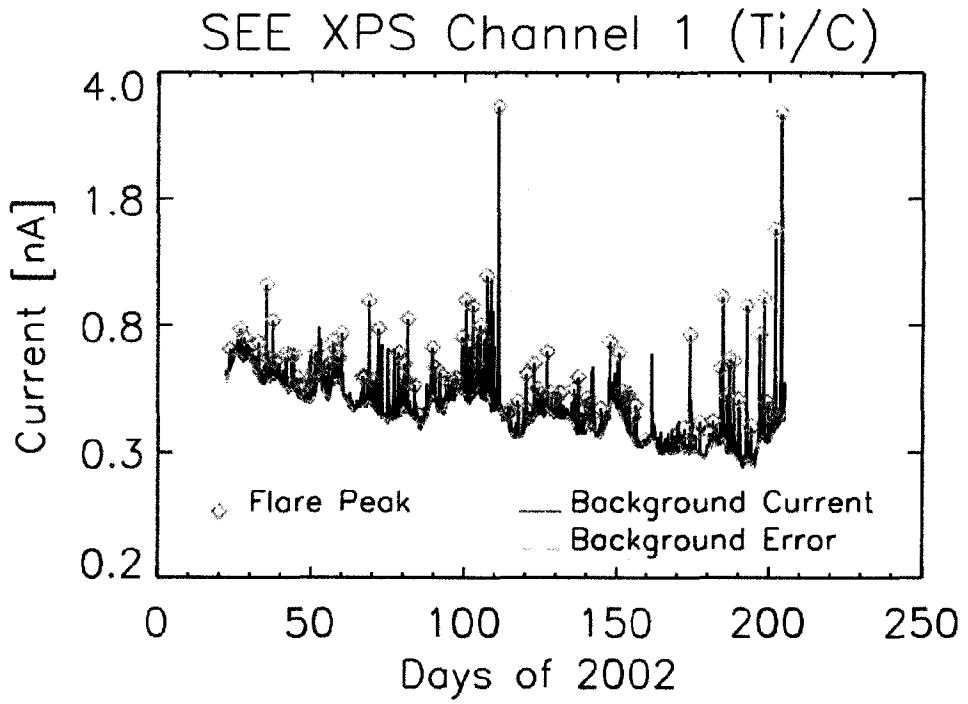

b)

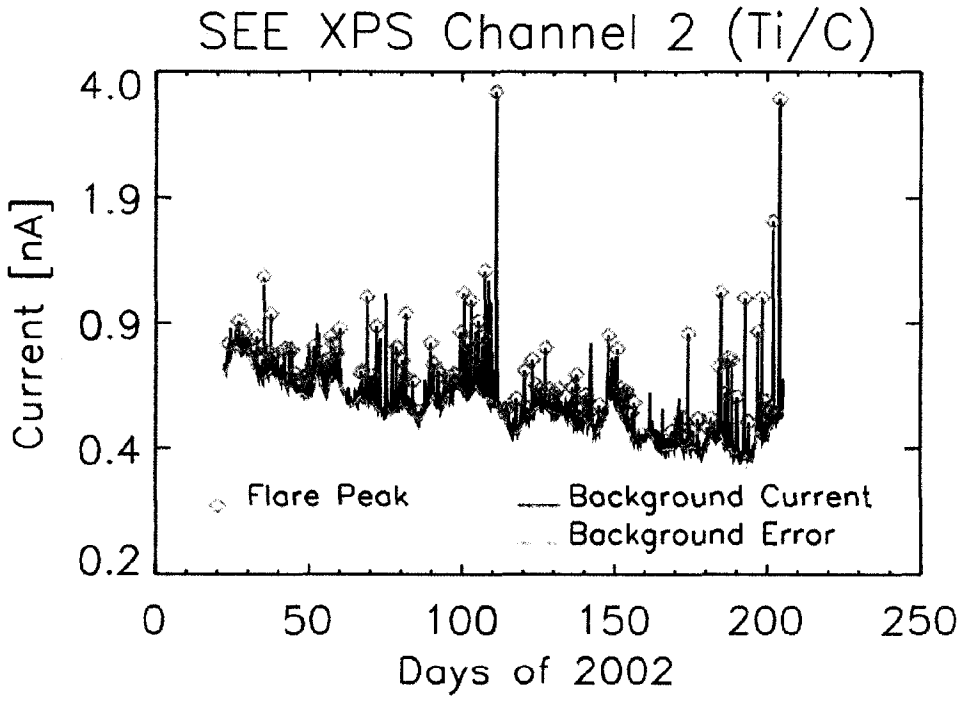

Figure 2.8 Time series of SEE XPS observations during 2002. a) channel 1, b) channel 2, c) channel 5, d) channel 6, e) channel 7, f) channel 9, and g) channel 10. Peaks of the studied flares are highlighted green.

c)

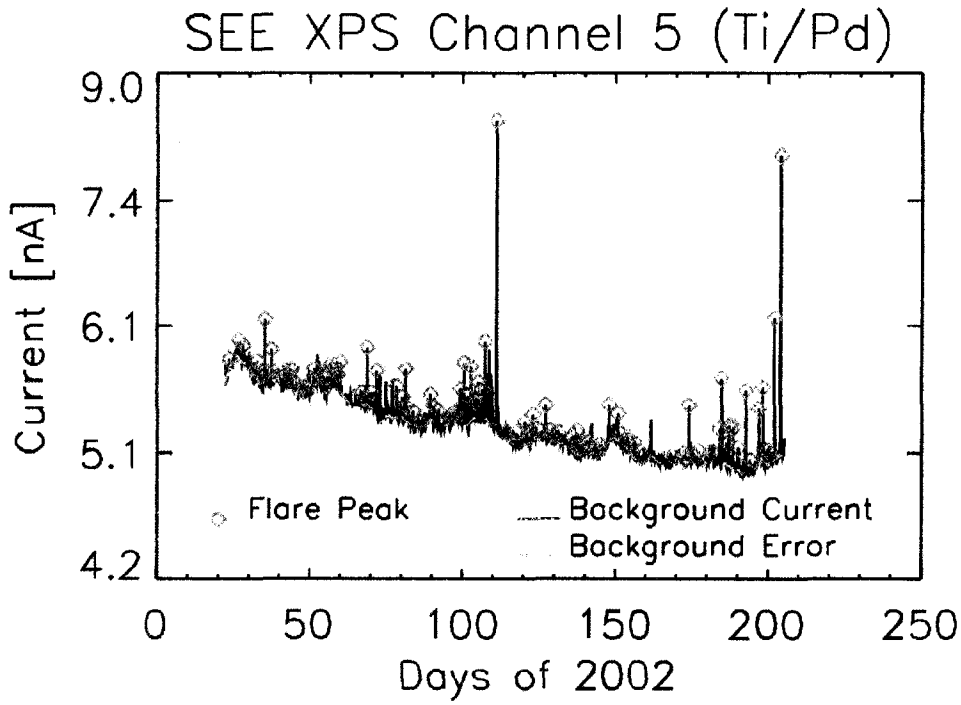

d)

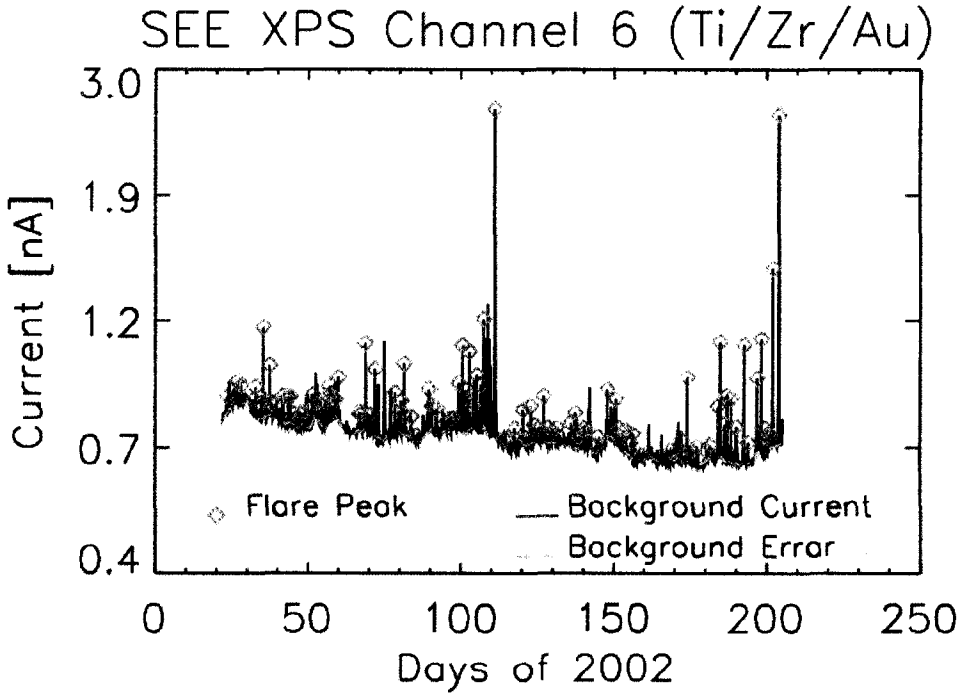

Figure 2.8 continued

e)

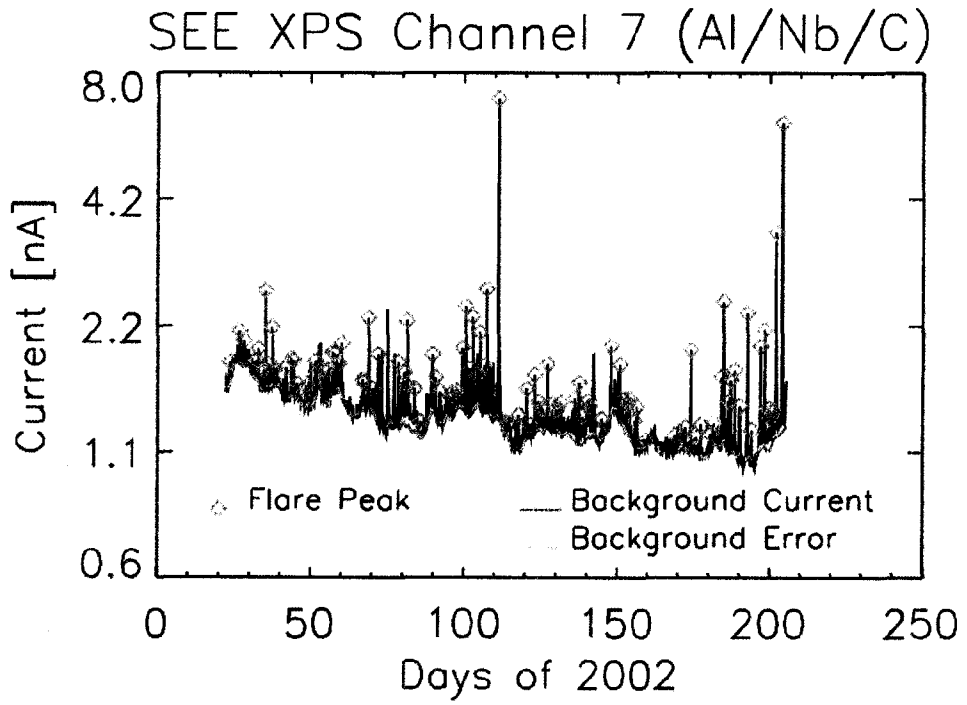

f)

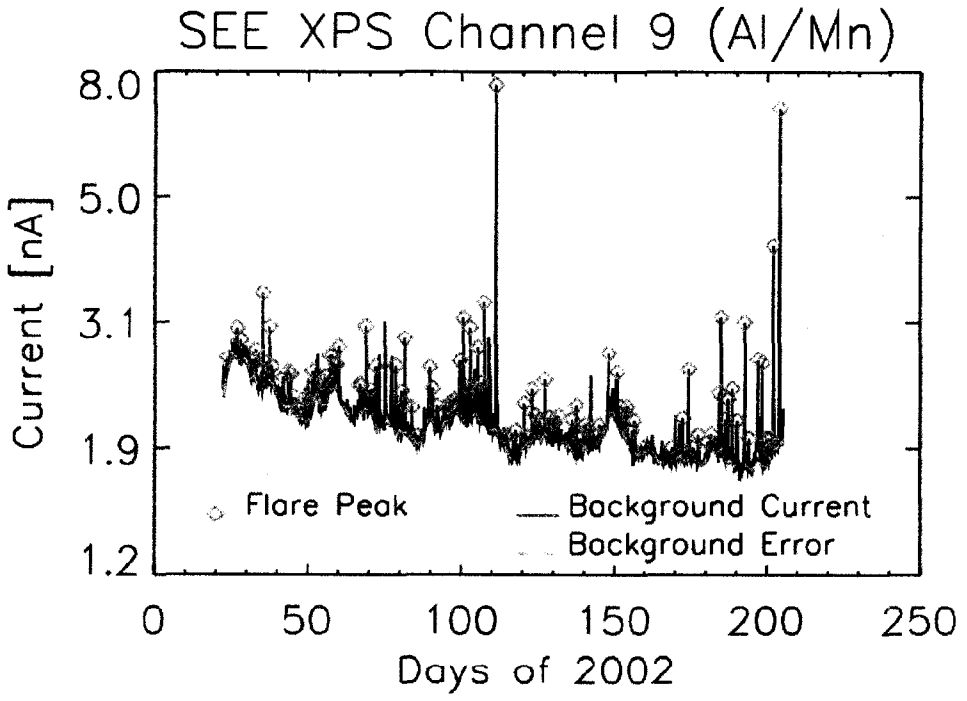

Figure 2.8 continued

g)

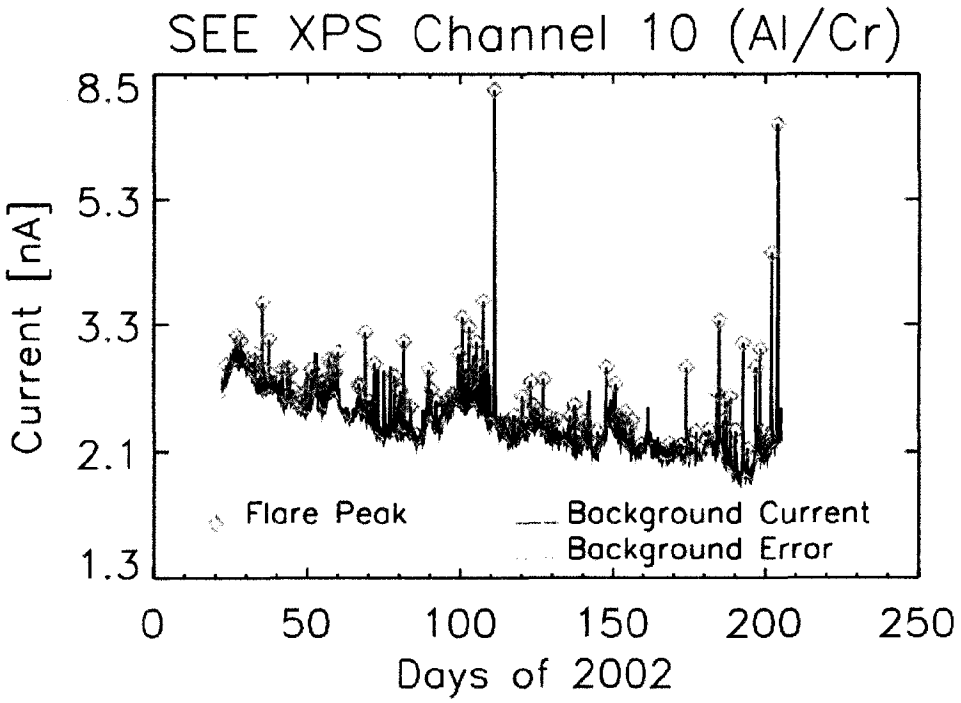

Figure 2.8 continued

a)

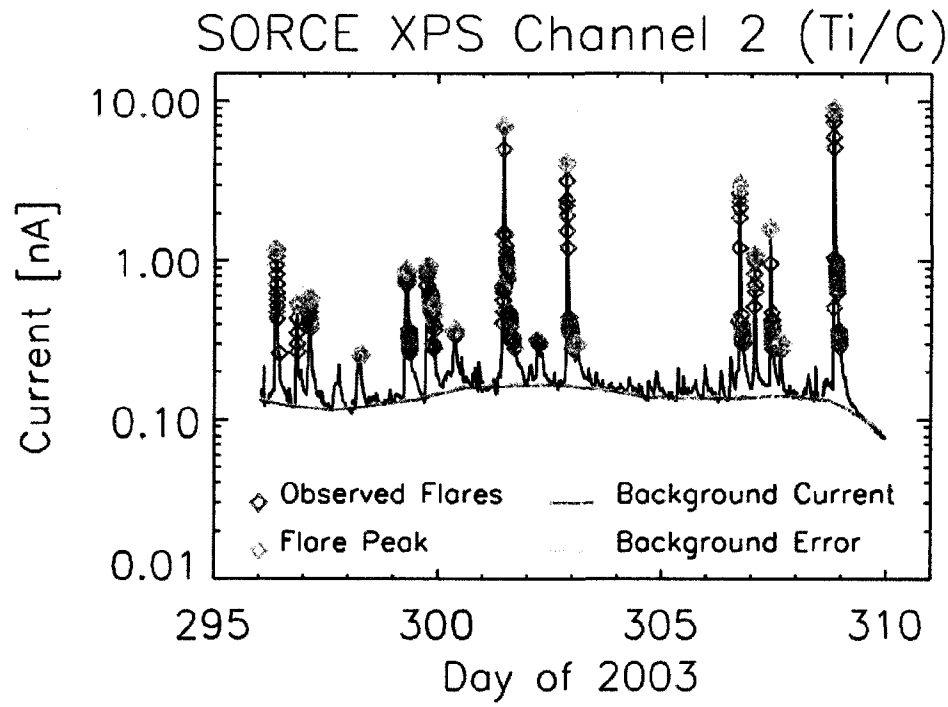

b)

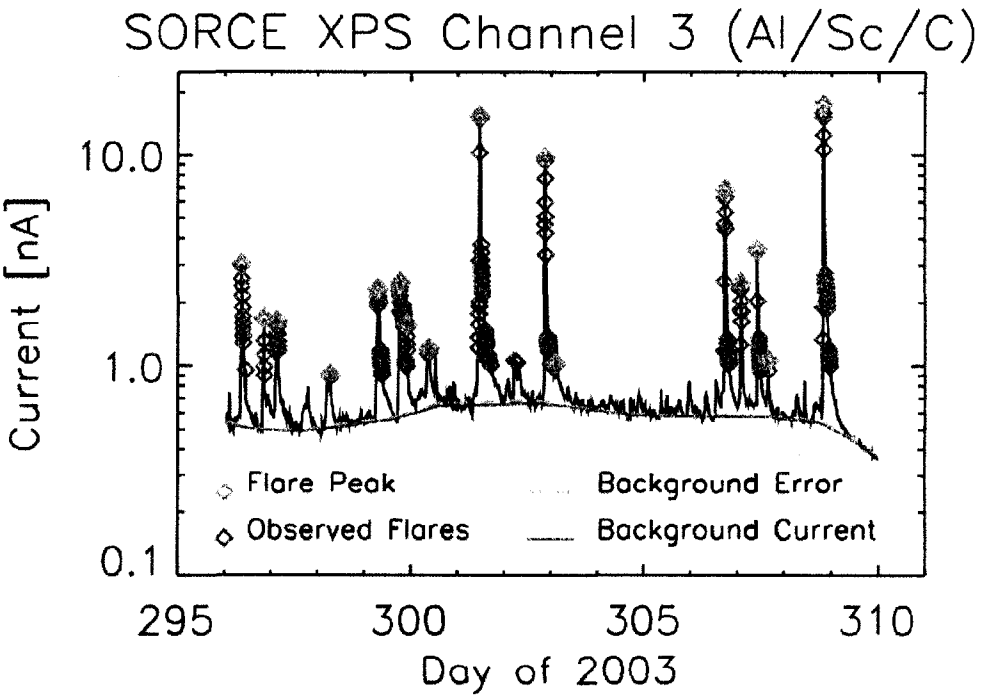

Figure 2.9 Time series of SORCE XPS observations during 2003. a) channel 2, b) channel 3, and c) channel 6. Peaks of the studied flares are highlighted green.

c)

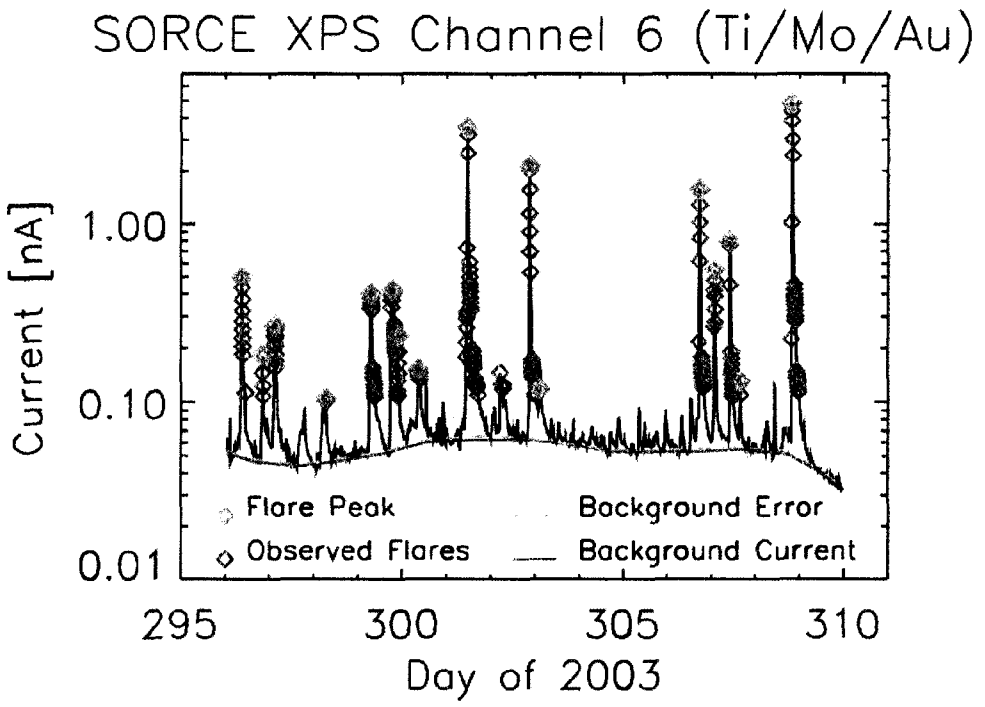

Figure 2.9 continued

is highlighted in red, the background error in dashed orange, and all solar flare observations are represented by blue diamonds. The green diamonds represent the peak of the 16 observed flares that are considered for this study. The flare currents have average absolute uncertainties of 0.12 nA for channel 2, 0.17 nA for channel 3, and 0.16 nA for channel 6.

The SEE and SORCE XPS solar flare observations were compared to GOES solar flare X-ray irradiance data for the same dates and times during 2002 and 2003. Figures 2.10 and 2.11 show the relevant time series of the GOES-10 0.1-0.8 nm irradiance. The orange diamonds represent the peak irradiance of the solar flares observed by GOES-10 that are also observed by either the SEE or SORCE XPS respectively for each figure. The solar flare X, M and C classification regions previously defined in Table 1.4 are also shown. The XPS instruments detect flares at the same time as GOES using the described 3-σ limit set for identifying XPS flares. Of the total 118 solar flares observed by both SEE and SORCE, 15 are X-class, 41 are M-class and 62 are C-class. Tables 2.3 and 2.4 compare the GOES-10 XRS peak observation times and the SEE and SORCE XPS flare observation times for the same solar flares. As indicated by these tables, GOES generally detects the peak solar flare irradiance earlier because the XRS observes the Sun over longer observation periods and observes shorter X-rays (0.1-0.8 nm) than does the XPS instrument (0.1-34 nm). The GOES XRS can detect flares in the impulsive and gradual phase, while the XPS mostly detects flares in the later gradual phase while the signal is still 3-σ higher than the background signal.

The flare currents change very little during the sampling time of the XPS photodiode channels, over which time the peak measured currents are interpolated onto one time grid. Figures 2.12 and 2.13 show the peak measured current of SEE XPS channel #7 before and after interpolation for two different solar flares. The peak measured current varied by 0.05% (0.0007 nA difference) from the original value for the 5 June 2002 C3.4 flare observation, and the peak measured current varied by 0.23% (0.017 nA difference) from the original value for the 21 April 2002 X.16 flare observation. These values are representative of all 102 SEE XPS flare current measurements. The GOES-10 0.1-0.8

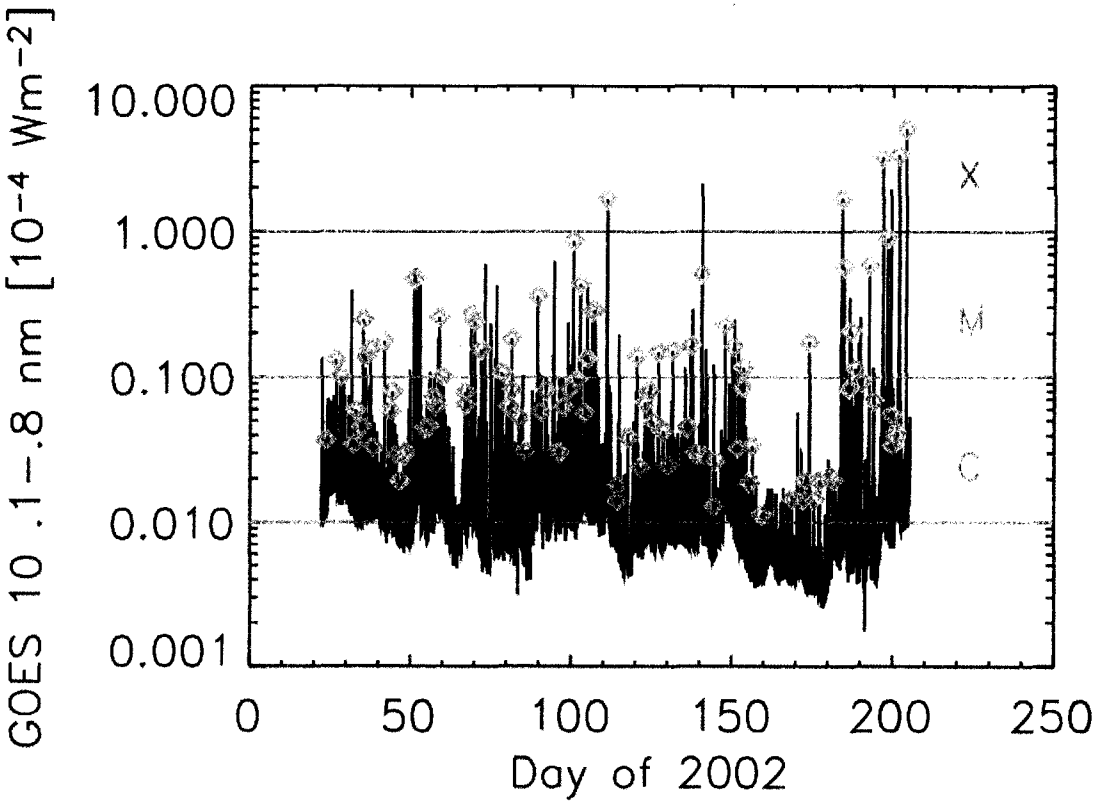

Figure 2.10 Time series of the GOES-10 0.1-0.8 nm irradiance for the same six month period in 2002 as the SEE XPS flare observations. The 102 orange diamonds represent the peak of the solar flares observed by GOES-10 that are also observed by the SEE XPS. Each level of solar flare classification is highlighted.

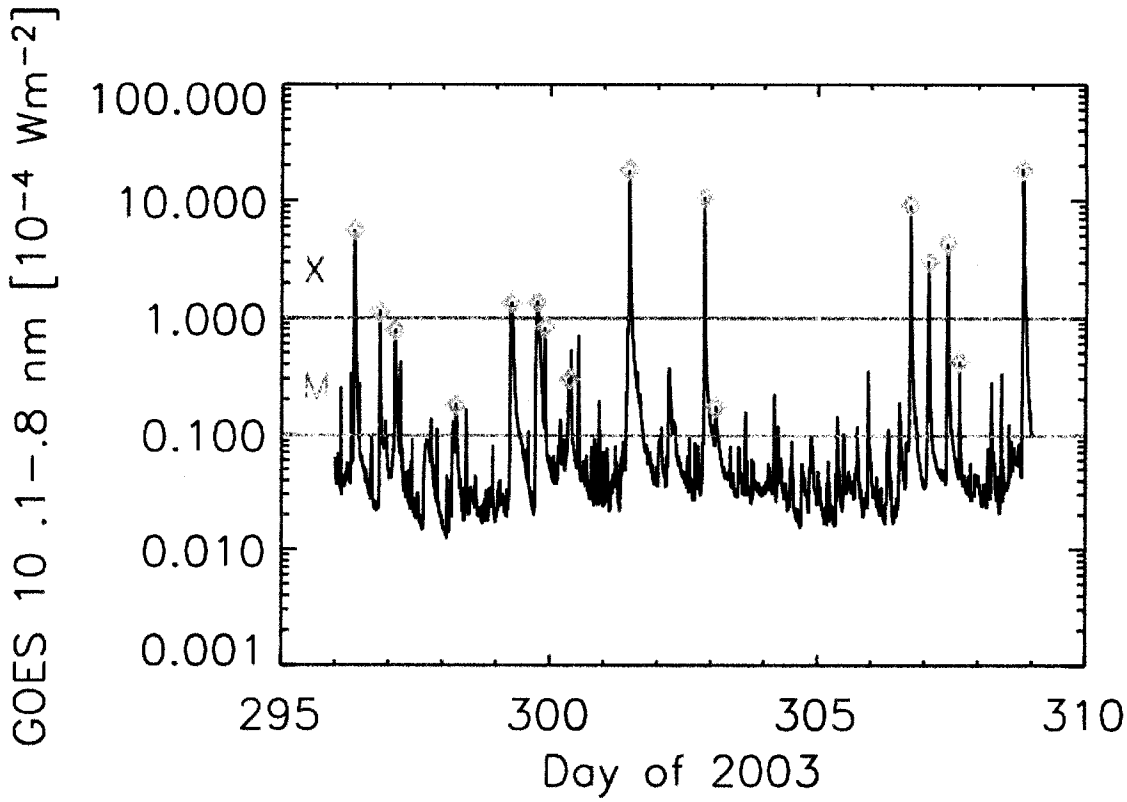

Figure 2.11 Time series of the GOES-10 0.1-0.8 nm irradiance for the same two-week period in 2003 as the SORCE XPS flare observations. The 16 orange diamonds represent the peak irradiance of the solar flares observed by GOES-10 that are also observed by the SORCE XPS. Each level of solar flare classification is highlighted.

Table 2.3 The 102 SEE XPS observed flares compared to GOES-10 XRS observed flares on same date during a six month period in 2002. The little difference between the XPS 0.1-2 and 0.1-7 nm irradiance for these flares shows that most of the flare enhanced energy is in the 0.1-2 nm wavelength range.

Flare Observation		GOES 10	GOES Peak	XPS Flare Obs	XPS 0.1-0.8 nm	XPS 0.1-2 nm	XPS 0.1-7 nm
Date	DOY 2002	Class	Time (UT)	Time (UT)	Irradiance [mW/m^2]	Irradiance [mW/m^2]	Irradiance [mW/m^2]
01/23/02	023	C3.7	1337	1337	0.004	0.060	0.083
01/26/02	026	M1.3	2045	2104	0.003	0.108	0.172
01/28/02	028	M1.0	0310	0353	0.005	0.076	0.126
02/01/02	032	C3.4	0427	0510	0.002	0.054	0.091
02/01/02	032	C5.9	2120	2123	0.006	0.106	0.152
02/03/02	034	C4.5	1519	1533	0.002	0.053	0.079
02/04/02	035	M2.4	0602	0607	0.018	0.358	0.473
02/04/02	035	M1.3	2330	2358	0.003	0.067	0.113
02/06/02	037	M1.5	1131	1138	0.016	0.140	0.269
02/07/02	038	C3.3	0524	0529	0.003	0.058	0.067
02/10/02	041	M1.7	1848	1926	0.010	0.085	0.108
02/12/02	043	C5.8	1442	1514	0.004	0.114	0.151
02/13/02	044	C8.0	0712	0727	0.005	0.100	0.143
02/14/02	045	C2.9	1106	1104	0.003	0.044	0.068
02/15/02	046	C1.9	1734	1759	0.001	0.022	0.039
02/16/02	047	C2.9	2332	2324	0.004	0.030	0.050
02/17/02	048	C3.1	1036	1049	0.003	0.052	0.082
02/20/02	051	M4.7	0251	0350	0.003	0.066	0.095
02/20/02	051	M4.8	0959	1019	0.006	0.106	0.162
02/23/02	054	C4.5	1360	1433	0.004	0.079	0.104
02/24/02	055	C4.5	1447	1453	0.005	0.088	0.132

Table 2.3 continued

Flare Observation		GOES 10	GOES Peak	XPS Flare Obs	XPS 0.1-0.8 nm	XPS 0.1-2 nm	XPS 0.1-7 nm
Date	DOY 2002	Class	Time (UT)	Time (UT)	Irradiance [mW/m^2]	Irradiance [mW/m^2]	Irradiance [mW/m^2]
02/26/02	057	C7.3	0056	0055	0.009	0.121	0.157
02/26/02	057	C6.3	1627	1708	0.007	0.078	0.172
02/28/02	059	M2.5	0012	0134	0.003	0.065	0.117
03/01/02	060	M1.0	0012	0015	0.011	0.165	0.191
03/07/02	066	C6.4	2103	2138	0.003	0.076	0.124
03/07/02	066	C7.9	2240	2315	0.002	0.073	0.113
03/09/02	068	M2.7	1853	1901	0.018	0.304	0.380
03/11/02	069	M2.4	2320	0326	0.003	0.059	0.096
03/12/02	071	M1.5	2313	2313	0.028	0.162	0.252
03/19/02	078	M1.0	1144	1227	0.006	0.165	0.287
03/21/02	080	C6.3	0812	0813	0.006	0.115	0.162
03/22/02	081	C8.2	0615	0654	0.004	0.077	0.115
03/22/02	081	M1.8	1111	1146	0.011	0.328	0.382
03/24/02	083	C5.2	1754	1853	0.004	0.075	0.126
03/26/02	085	C3.1	1521	1616	0.001	0.030	0.036
03/30/02	089	M3.6	1301	1417	0.007	0.155	0.227
03/31/02	090	C5.7	1237	1258	0.003	0.099	0.137
04/02/02	092	C8.1	0043	0038	0.005	0.085	0.098
04/05/02	095	C3.1	1722	1747	0.001	0.039	0.061
04/06/02	096	C3.0	0638	0645	0.002	0.053	0.078
04/07/02	097	C6.2	0824	0841	0.002	0.041	0.061
04/09/02	099	C8.2	0736	0741	0.009	0.159	0.243
04/10/02	100	M8.6	1232	1251	0.028	0.239	0.484
04/11/02	101	C9.6	1626	1626	0.014	0.128	0.151

Table 2.3 continued

Flare Observation		GOES 10	GOES Peak	XPS Flare Obs	XPS 0.1-0.8 nm	XPS 0.1-2 nm	XPS 0.1-7 nm
Date	DOY 2002	Class	Time (UT)	Time (UT)	Irradiance [mW/m^2]	Irradiance [mW/m^2]	Irradiance [mW/m^2]
04/12/02	102	M4.3	1801	1821	0.015	0.288	0.412
04/14/02	104	C5.7	0108	0111	0.005	0.070	0.119
04/15/02	105	M1.3	0353	0445	0.010	0.216	0.313
04/16/02	106	M2.8	1319	1312	0.012	0.140	0.164
04/17/02	107	M2.8	0824	0840	0.028	0.387	0.555
04/21/02	111	X1.6	0147	0213	0.103	1.967	2.541
04/24/02	114	C1.8	0548	0633	0.001	0.025	0.037
04/24/02	114	C1.4	0805	0811	0.001	0.027	0.051
04/27/02	117	C3.9	1539	1537	0.004	0.073	0.102
04/30/02	120	M1.4	0823	0828	0.009	0.090	0.168
05/01/02	121	C2.4	1003	1025	0.001	0.023	0.039
05/02/02	122	C6.7	2133	2203	0.007	0.126	0.215
05/04/02	124	C8.0	0251	0314	0.003	0.053	0.090
05/05/02	125	C4.9	0808	0825	0.002	0.048	0.065
05/07/02	127	M1.5	0346	0411	0.008	0.153	0.225
05/08/02	128	C4.3	1324	1412	0.002	0.055	0.089
05/10/02	130	C2.4	0116	0152	0.002	0.037	0.068
05/11/02	131	M1.5	1133	1154	0.003	0.049	0.010
05/16/02	136	C4.5	0032	0030	0.006	0.079	0.120
05/17/02	137	M1.6	0752	0854	0.007	0.117	0.185
05/18/02	138	C3.0	1138	1227	0.002	0.043	0.060
05/20/02	140	M5.1	1053	1128	0.002	0.063	0.089
05/20/02	140	C2.9	1820	1835	0.002	0.051	0.072
05/24/02	144	M1.2	0646	0751	0.001	0.028	0.033

Table 2.3 continued

Flare Observation		GOES 10	GOES Peak	XPS Flare Obs	XPS 0.1-0.8 nm	XPS 0.1-2 nm	XPS 0.1-7 nm
Date	DOY 2002	Class	Time (UT)	Time (UT)	Irradiance [mW/m^2]	Irradiance [mW/m^2]	Irradiance [mW/m^2]
05/24/02	144	C2.6	1911	1912	0.002	0.056	0.064
05/27/05	147	M2.2	1810	1830	0.010	0.180	0.297
05/30/02	150	M1.6	1723	1750	0.008	0.143	0.209
05/31/02	151	C3.2	1939	1945	0.002	0.063	0.095
06/02/02	153	C8.4	1015	1039	0.004	0.058	0.096
06/02/02	153	M1.1	2044	2154	0.003	0.091	0.134
06/04/02	155	C1.8	1255	1255	0.002	0.053	0.087
06/05/02	156	C3.4	0940	0959	0.006	0.065	0.125
06/08/02	159	C1.1	0856	0919	0.001	0.014	0.020
06/17/02	168	C1.4	2015	2020	0.001	0.041	0.051
06/21/02	172	C1.4	0554	0702	0.002	0.076	0.087
06/21/02	172	C1.9	2021	2314	0.001	0.018	0.036
06/23/02	174	M1.7	0251	0248	0.026	0.218	0.360
06/24/02	175	C1.4	1606	1606	0.001	0.035	0.044
06/26/02	177	C1.9	0818	0838	0.003	0.044	0.107
06/29/02	180	C2.0	0933	0936	0.001	0.033	0.056
06/30/02	181	C1.9	1256	1309	0.001	0.047	0.065
07/03/02	184	X1.6	0212	0245	0.015	0.164	0.189
07/03/02	184	M5.7	2010	2035	0.026	0.386	0.588
07/05/02	186	C8.3	0810	0815	0.007	0.110	0.146
07/06/02	187	M2.0	0340	0341	0.017	0.171	0.215
07/07/02	188	M1.1	1143	1207	0.014	0.173	0.283
07/09/02	190	C9.3	0413	0438	0.008	0.090	0.161
07/11/02	192	M5.9	1451	1500	0.021	0.401	0.602

Table 2.3 continued

Flare Observation		GOES 10	GOES Peak	XPS Flare Obs	XPS 0.1-0.8 nm	XPS 0.1-2 nm	XPS 0.1-7 nm
Date	DOY 2002	Class	Time (UT)	Time (UT)	Irradiance [mW/m^2]	Irradiance [mW/m^2]	Irradiance [mW/m^2]
07/13/02	194	C6.9	0050	0102	0.003	0.063	0.105
07/15/02	196	X3.2	2008	2106	0.020	0.215	0.397
07/17/02	198	M9.0	0713	0707	0.057	0.281	0.353
07/18/02	199	C5.5	1354	1355	0.007	0.071	0.094
07/18/02	199	C3.4	2023	2024	0.003	0.050	0.066
07/19/02	200	C3.9	1853	1905	0.002	0.054	0.068
07/20/02	201	C4.2	0259	0312	0.002	0.046	0.062
07/20/02	201	X3.3	2127	2238	0.035	0.801	1.010
07/23/02	204	X5.1	0035	0052	0.119	1.755	2.108

Table 2.4 Sixteen SORCE XPS observed flares compared to GOES-10 XRS observed flares on same date during the fall of 2003. The little difference between the XPS 0.1-2 and 0.1-7 nm irradiance for these flares shows that most of the flare enhanced energy is in the 0.1-2 nm wavelength range.

Flare Observation		GOES 10	GOES Peak	XPS Flare Obs Time	Calculated 0.1-0.8 nm	XPS 0.1-2 nm	XPS 0.1-7 nm
Date	DOY 2003	Class	Time (UT)	(UT)	Irradiance [mW/m^2]	Irradiance [mW/m^2]	Irradiance [mW/m^2]
10/23/03	296	X5.6	0836	0859	0.168	2.137	2.444
10/23/03	296	X1.1	2002	2015	0.047	0.773	1.311
10/24/03	297	M7.8	0253	0259	0.095	0.917	1.067
10/25/03	298	M1.7	0600	0622	0.019	0.223	0.426
10/26/03	299	X1.3	0652	0656	0.131	1.533	1.792
10/26/03	299	X1.3	1813	1832	0.151	1.597	1.843
10/26/03	299	M8.3	2140	2145	0.081	0.843	0.992
10/27/03	300	M2.9	0927	0847	0.088	0.725	0.843
10/28/03	301	X18	1109	1112	0.778	12.28	16.93
10/29/03	302	X10	2048	2050	0.726	5.568	10.11
10/30/03	303	M1.7	0207	0212	0.009	0.342	0.543
11/02/03	306	X9.2	1725	1728	0.447	5.440	6.520
11/03/03	307	X3.0	0129	0135	0.098	1.816	2.076
11/03/03	307	X4.3	0955	0956	0.249	2.659	3.085
11/03/03	307	M4.2	1532	1545	0.023	0.327	0.592
11/04/03	308	X28	1944	1949	1.183	15.07	19.42

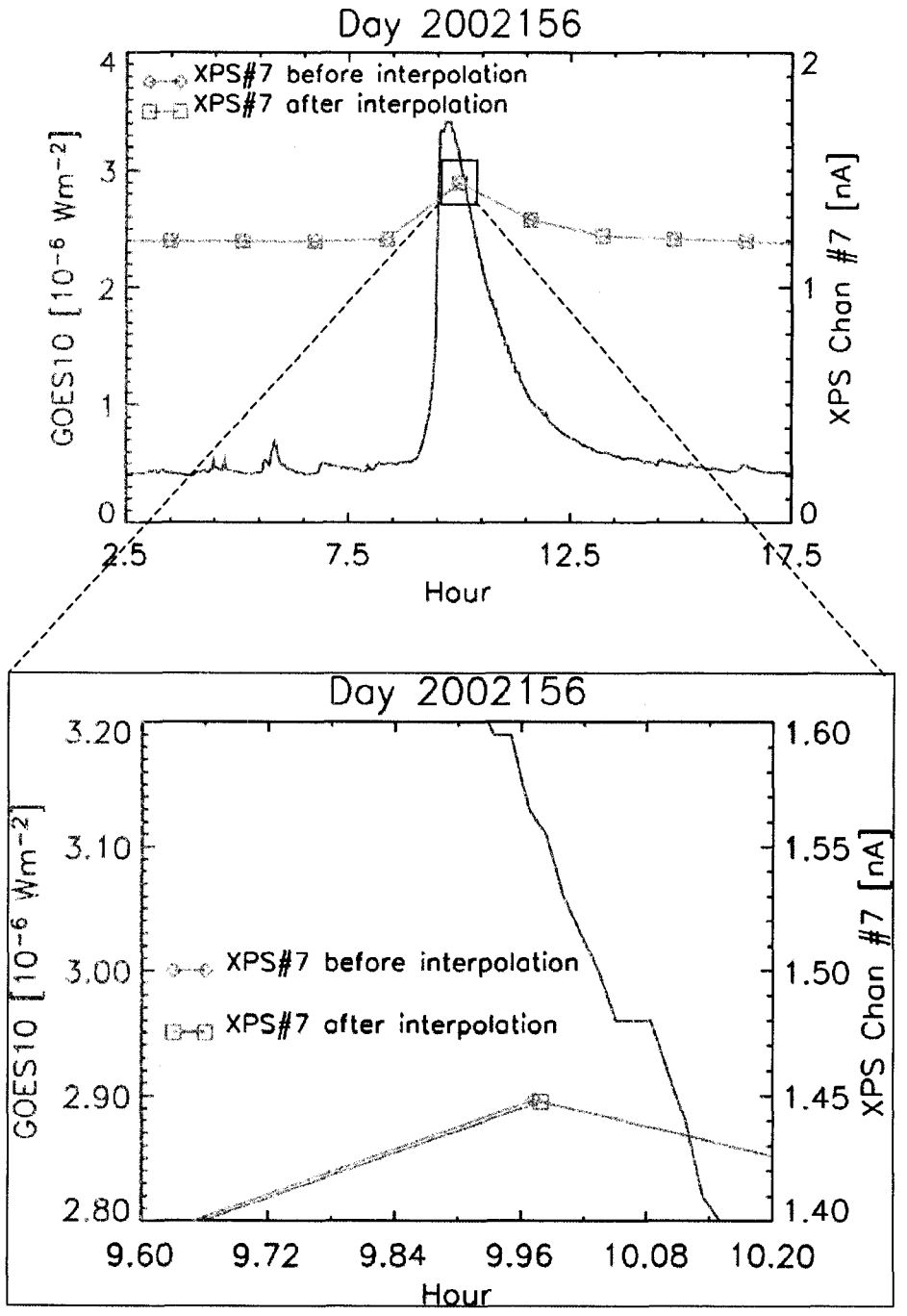

Figure 2.12 Peak measured currents of SEE XPS channel #7 before (green) and after (blue) interpolation for the 5 June 2002 C3.4 solar flare. The flare current changes very little during the sampling time of the XPS photodiode channels, over which time the peak measured currents are interpolated onto one time grid. The GOES-10 0.1-0.8 nm irradiance (red) does not change significantly over the time period of interpolation.

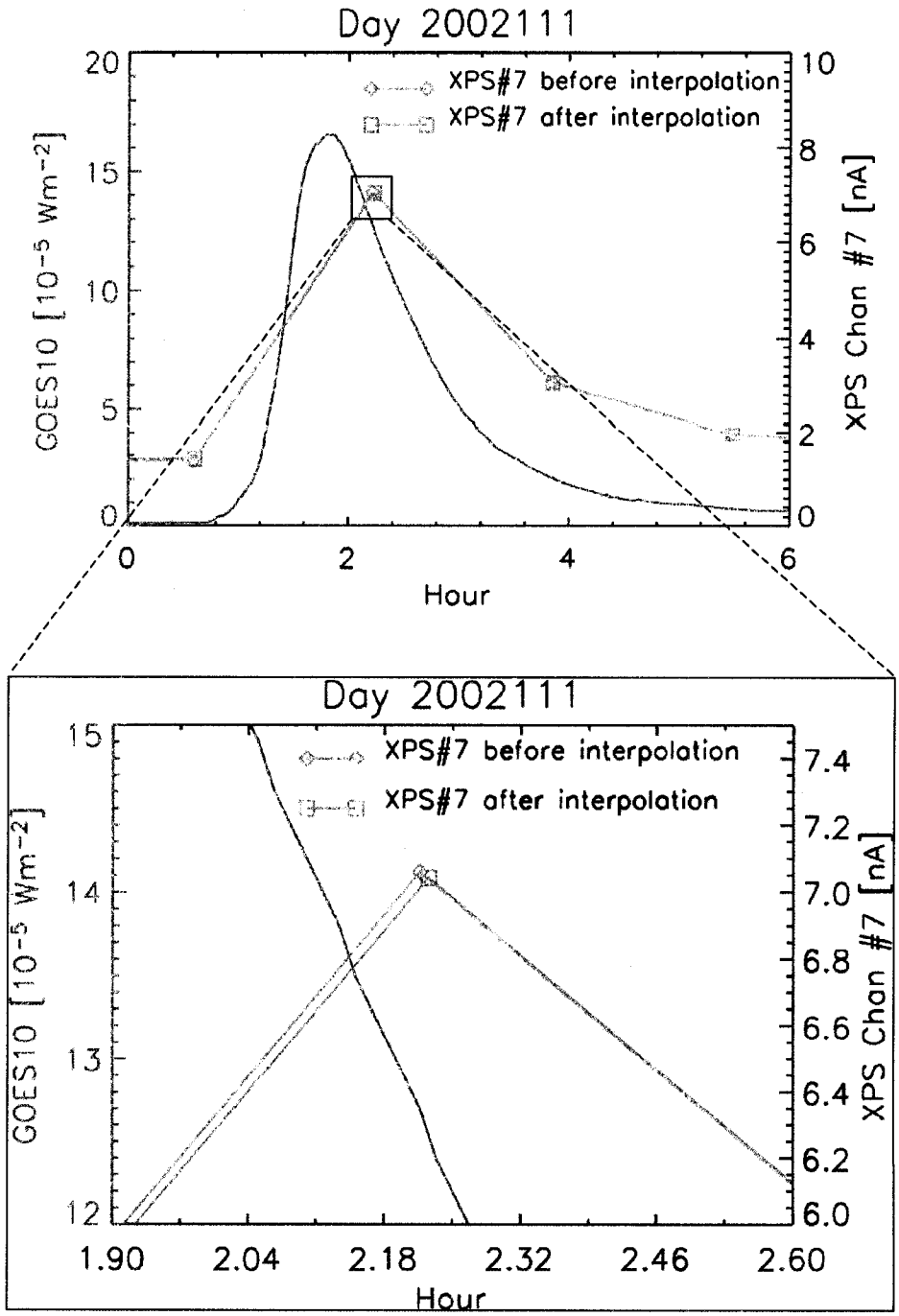

Figure 2.13 Peak measured currents of SEE XPS channel #7 before (green) and after (blue) interpolation for the 21 April 2002 X1.6 solar flare. The flare current changes very little during the sampling time of the XPS photodiode channels, over which time the peak measured currents are interpolated onto one time grid. The GOES-10 0.1-0.8 nm irradiance (red) does not change significantly over the time period of interpolation.

nm irradiance does not change significantly over the time period of interpolation as shown in Figures 2.12 and 2.13. Both flare observations were made after the peak of the flare was observed by GOES-10.

Figure 2.14 shows the peak measured current of SORCE XPS channel #6 before and after interpolation for one solar flare. The peak measured current varied by 1.2% (0.042 nA difference) from the original value for the 28 October 2003 X18 flare observation. This value is representative of all 16 SORCE XPS flare current measurements and is larger than those for the SEE XPS because the SORCE XPS peak measured currents are interpolated over a longer time period that corresponds to a longer solar observation period. This flare observation was made after the peak of the flare was observed by GOES-10, and the 0.1-0.8 nm irradiance does not change significantly during the time period of interpolation as shown in Figure 2.14.

The SEE and SORCE XPS flare currents and their corresponding errors are used in Chapter 3 to determine the spectra of all SEE and SORCE XPS observed solar flares.

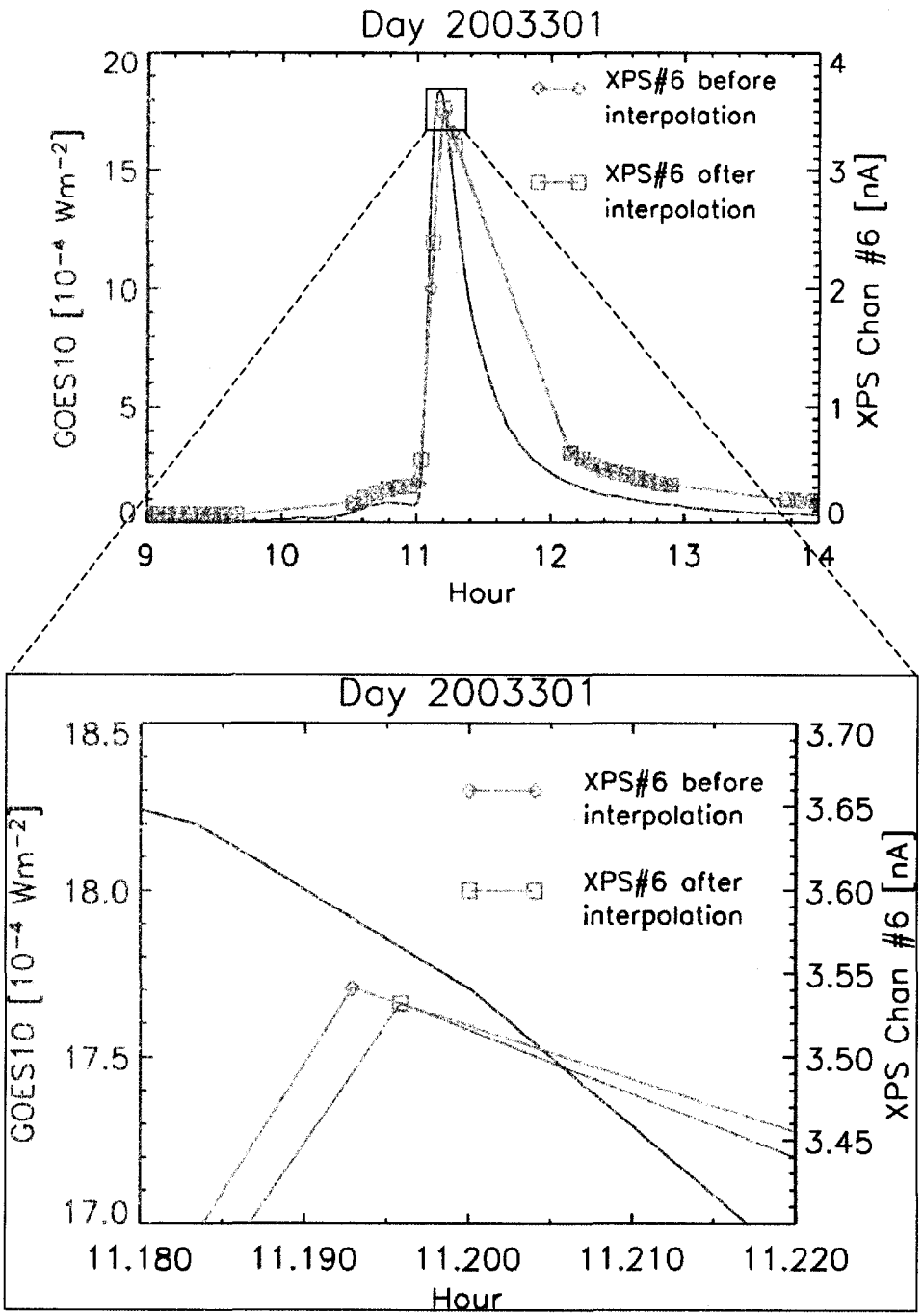

Figure 2.14 Peak measured currents of SORCE XPS channel #6 before (green) and after (blue) interpolation for the 28 October 2003 X18 solar flare. The flare current changes very little during the sampling time of the XPS photodiode channels over, which time the peak measured currents are extrapolated onto one time grid. The GOES-10 0.1-0.8 nm irradiance (red) does not change significantly over the time period of interpolation.

Chapter 3 Solar Flare Retrieval Algorithm

The SEE and SORCE XPS solar flare observations described in Chapter 2 were used to infer solar flare spectra. The particular method for determining a solar flare irradiance spectrum from broadband measurements relies first on the 'differential emission measure' (DEM) technique for describing solar irradiance, as presented by Warren et al. [1998a] and earlier developed by Pottasch [1963]. The flare spectrum is then determined by interpreting the XPS observations with a model that calculates theoretical spectra for DEMs input to this model. Chapter 3 provides a full description of the DEM technique, how it is used to define the solar irradiance, and how the DEM technique, solar irradiance and XPS photodiode measurements are used together in an algorithm to determine spectra from the solar flare observations.

3.1. Differential Emission Measure (DEM)

A solar line emission is produced when an electron in an atom is first caused to move from a lower to a higher energy orbit, exciting the atom, followed at some later time by the release of energy (a photon) as the electron decays to a lower energy orbit. The photon energy equals the difference in energy of the two energy states. The volume emission rate is defined as the number of photons emitted isotropically per unit time per unit volume, and is determined quantitatively as the transition rate from the upper to the lower energy state times the number density of excited atoms (the corona is fully ionized and all atoms are ions);

$$\varepsilon(\lambda_{ul},T) = n_u A_{ul} \quad (\text{ph cm}^{-3}\ \text{s}^{-1}). \tag{3.1}$$

The number density of excited ions is denoted as n_u (cm^{-3}), and A_{ul} is the Einstein rate coefficient (s^{-1}). The radiance of an optically thin solar emission line is the volume emission rate of the solar emission line integrated along the line of sight, s, from the solar disk to the Earth,

$$I(\lambda_{ul}) = \frac{1}{4\pi}\int_s \varepsilon(\lambda_{ul},T)ds = \frac{1}{4\pi}\int_s n_u A_{ul} ds \quad (\text{ph s}^{-1}\ \text{cm}^{-2}\ \text{sr}^{-1}). \tag{3.2}$$

Here the thin coronal emitting layer is small relative to the distance to the Earth. An optically thin medium has a total optical path much less than one, which means that solar

photons are expected to traverse the coronal region with only minimal (or no) absorption or scattering. The medium here is assumed to be optically thin.

To achieve a description of the DEM, the radiance of an optically thin solar emission line is first separated into factors that are known and those that are unknown, beginning with an expansion of the number density of excited ions, n_u, through the following identity composed of a chain of ratios;

$$n_u = \frac{n_u}{n_{ion}} \frac{n_{ion}}{n_{el}} \frac{n_{el}}{n_H} \frac{n_H}{n_e} n_e \quad (\text{cm}^{-3}). \tag{3.3}$$

Here n_{ion} is the number density of ions (cm^{-3}), n_{el} is the number density of the emitting atoms (cm^{-3}), n_H is the hydrogen number density (cm^{-3}) and n_e is the electron number density (cm^{-3}). First, the radiance of an optically thin solar emission line is separated into factors that depend on solar conditions and those that depend on atomic physics. The level population ratio, $\frac{n_u}{n_{ion}}$, is the ratio of excited ions relative to the total number of ground-state ions (e.g., $\frac{[FeXV]^*}{[FeXV]}$). This ratio is calculated for all ions in the solar corona with the Astrophysical Plasma Emission Database [Smith et al., 2001] assuming the n_e is 10^9 cm^{-3} and using collisional excitation/de-excitation rate coefficients, radiative transition rates, and the radiative and dielectronic recombination rate coefficients of the emitting ions, n_u, for a given temperature. The ionization ratio, $\frac{n_{ion}}{n_{el}}$, is the number density of ground-state ions relative to the number density of atoms (e.g., $\frac{[FeXV]}{[Fe]}$), and is calculated from coronal ionization balance calculations by Mazzotta et al. [1998]. The $\frac{n_{el}}{n_H}$ ratio, is generally referred to as A_{el}, and is the coronal elemental abundance relative to hydrogen for all atoms in the corona (e.g., $\frac{[Fe]}{[H]}$), and is given by Feldman et al. [1992]. Lastly, the hydrogen to electron density ratio (e.g., $\frac{[H]}{[e^-]}$), $\frac{n_H}{n_e} \approx 0.8$, is

determined by Warren et al. [1998a] to be $1/(1+2A_{He}/A_H)$ where the coronal abundances of He and H (A_{He} and A_H) are listed in Table 1.1.

The level population ratio, $\frac{n_u}{n_{ion}}$, and ionization ratio, $\frac{n_{ion}}{n_{el}}$, were calculated by the previously defined databases, assuming they are weakly dependent on electron density and strongly dependent on the electron temperature. The $\frac{n_H}{n_e}$ and A_{el} ratios depend on solar atmosphere conditions and are determined from independent observations of emission line radiance [Warren et al., 1998a]. The $\frac{n_H}{n_e}$ ratio is constant and the A_{el} ratio is constant for each coronal elementUsing these defined ratios, the radiance of a solar emission line (Equation 3.2) can now be expressed as,

$$I(\lambda_{ul}) = \frac{1}{4\pi}\int_s \frac{n_u}{n_{ion}}\frac{n_{ion}}{n_{el}}A_{el}\frac{n_H}{n_e}A_{ul}n_e ds \quad (\text{ph s}^{-1}\text{ cm}^{-2}\text{ sr}^{-1}). \tag{3.4}$$

The $\frac{n_u}{n_{ion}}$, $\frac{n_{ion}}{n_{el}}$, A_{el}, and $\frac{n_H}{n_e}$ ratios are known for the conditions in which they were calculated or observed, and are assumed to be valid under all conditions. Therefore, it is possible to assume that only the electron density of the emitting solar flare plasma, n_e, and its distribution along the line of sight are unknown.

It is common to combine all atomic physics and solar condition ratios into a contribution function, $G_{ul}(\lambda,T)$, which is the $\varepsilon_{ul}(\lambda,T)$ divided by n_e^2. The photons described here arise from the collision of ions and electrons. In the fully ionized corona, the $\frac{n_u}{n_{ion}}$ ratio is proportional to n_e, and $G_{ul}(\lambda,T)$ is expressed as;

$$G_{ul}(\lambda,T) = \frac{1}{4\pi}\frac{n_u}{n_{ion}}\frac{n_{ion}}{n_{el}}A_{el}\frac{n_H}{n_e}A_{ul}\frac{1}{n_e} \quad (\text{ph s}^{-1}\text{ cm}^{3}\text{ sr}^{-1}). \tag{3.5}$$

The contribution function is strongly peaked in temperature and contains all of the known atomic physics and solar atmosphere conditions. The contribution function is substituted into the solar emission line radiance (Equation 3.4) and is expressed as,

$$I(\lambda_{ul}) = \int_s G_{ul}(\lambda,T)n_e^2 ds \quad (\text{ph s}^{-1}\text{ cm}^{-2}\text{ sr}^{-1}). \tag{3.6}$$

The n_e^2 and its distribution along the line of sight are unknown and can be expressed as the DEM to describe the unknown density of the emitting hot plasma,

$$\xi(T) = n_e^2 \frac{ds}{dT} \quad (\text{cm}^{-5}\ \text{K}^{-1}), \tag{3.7}$$

where n_e is the electron density (cm^{-3}), ds is the differential height in the solar atmosphere (cm), and dT is the differential electron temperature (K). The variable transformation is made in order to determine the plasma density in terms of temperature and to reflect the contribution function's, $G_{ul}(\lambda,T)$), dependence on temperature. The temperature distribution along the line of sight is not known. However, it is assumed to be a monotonic relationship where there is a unique temperature at each altitude. The DEM, $\xi(T)$, is a measure of the abundance of plasma along the line of sight that contributes to the emitted radiation in a temperature range [Craig and Brown, 1976]. The DEM is also a description of the multi-temperature electron distribution of the solar corona, as the corona consists of many coronal loops each filled with different temperature plasma. The unknown DEM contains information about the density and temperature structure of the corona. By estimating the electron density at every temperature and assuming a constant pressure ($p=n_eT$), a known DEM would provide a temperature and density model of the solar corona as a function of height [Warren et al., 1998a].

The solar emission line radiance (Equation 3.6) is then expressed as the convolution of a known kernel (contribution function, $G_{ul}(\lambda,T)$) with a function, $\xi(T)$, which is to be determined;

$$I(\lambda_{ul}) = \int_T G_{ul}(\lambda,T)\xi(T)dT \quad (\text{ph}\ \text{s}^{-1}\ \text{cm}^{-2}\ \text{sr}^{-1}). \tag{3.8}$$

Equation 3.8 combines the assumed properties of the solar atmosphere ($G_{ul}(\lambda,T)$) with the unknown line-of-sight electron density of emitting hot plasma ($\xi(T)$), to compute the radiance of a solar emission line [Warren et al., 2001].

The DEM of the quiet-Sun is different than a DEM of a solar flare because flare plasma is hotter than quiet-Sun plasma and emits more short wavelength radiation, such as soft X-rays. The magnitude of a DEM profile represents the abundance of the solar

plasma squared as a function of temperature multiplied by $\frac{ds}{dT}$, and the peak of the DEM profile represents the temperature of the bulk of solar plasma that is involved in the emission process. Two quiet-Sun DEMs are presented in Figure 3.1. The 'Warren' DEM was derived from using several quiet-Sun emission line radiances from the chromosphere to the corona observed from instruments aboard SOHO and inverting Equation 3.8 to calculate a DEM [Warren, 2005]. The contribution function was calculated from the CHIANTI 4.1 atomic physics database [Dere et al., 1997; Young et al., 2003], the ionization balance of Mazzotta et al. [1998], and the coronal abundances of Meyer [1985]. The 'D&Y' DEM was derived the same way as the 'Warren' DEM, but using quiet-Sun chromosphere and coronal emission line radiances observed from Skylab [Vernazza and Reeves, 1978], the CHIANTI 3.2 atomic physics database [Dere et al., 1997; Landi et al., 2002], and the coronal abundances of Feldman et al. [1992]. Both quiet-Sun DEM profiles have a peak near 1 MK, which is the temperature of the bulk of the coronal plasma and represents the quiet-Sun coronal emission temperature.

Several solar flare DEM profiles are described by Acton et al., [1999]. Four DEM profiles from one of these flares are derived by Dere and Cook [1979] using the electron densities of the 9 August 1973 M2 solar flare and using several soft X-ray emissions observed by instruments aboard Solrad 9 and Skylab. Figure 3.1 also shows four DEM profiles obtained during the M2 solar flare, where each of the four DEM profiles are one-minute apart, beginning at the time of the soft X-ray peak irradiance. As the flare progresses in time and the flare plasma begins to cool, the DEM profile peaks at cooler and cooler temperatures; the 1553 UT DEM peaks near 12.6 MK, the 1554 UT DEM peaks near 10 MK, the 1555 UT DEM peaks near 7.9 MK, and the 1556 UT DEM peaks near 6.3 MK. The solar flare DEM profiles peak from 6.3-12.6 MK, which are the temperatures of the bulk of the plasma at each time and represents the solar flare emission temperature. The solar flare DEM profiles peak at higher temperatures than do the quiet-Sun DEMs because the flare plasma is hotter than the quiet-Sun plasma, and the flare DEM profiles peak at lower values because the abundance of flare plasma is less than the abundance of quiet-Sun coronal plasma.

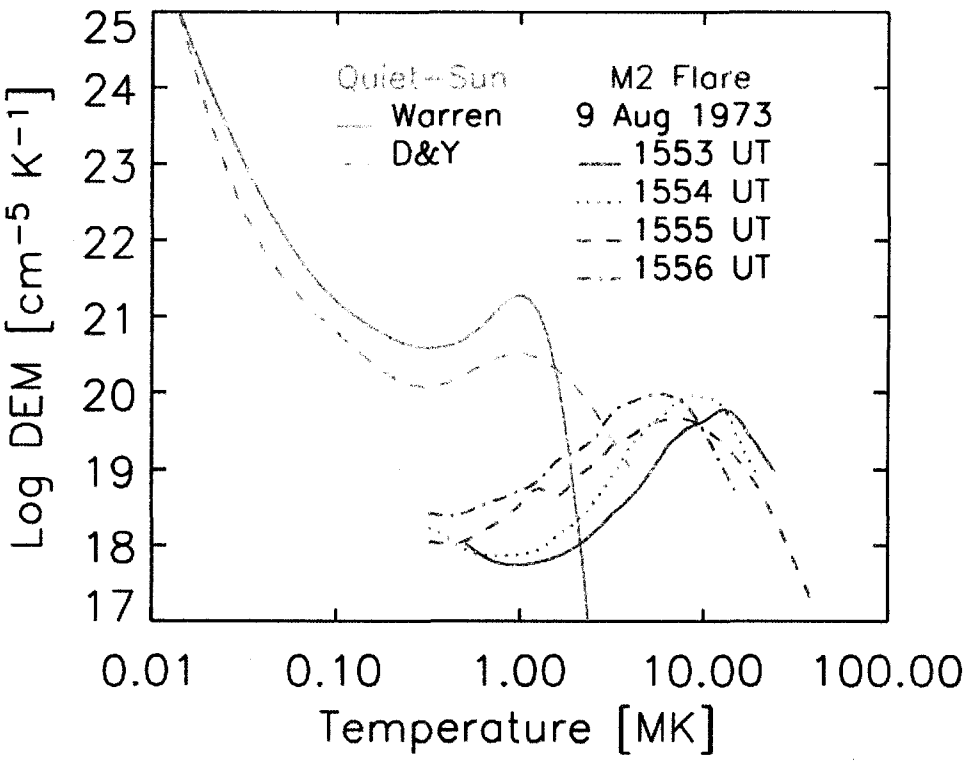

Figure 3.1 Quiet-Sun and solar flare DEM profiles. The two quiet-Sun DEM profiles are determined from Warren [2005] (—), and Dere et al. [1997] and Young et al. [2003] (D&Y) (---). Both quiet-Sun DEM profiles have a peak near 1 MK, which is the temperature of the bulk of the coronal plasma and represents the quiet-Sun coronal emission temperature. The four DEM profiles during the 9 August 1973 M2 solar flare are determined by Dere and Cook [1979]. Each of the four DEM profiles are one-minute apart and begin at the time of the soft X-ray peak irradiance, 1553 UT (—), 1554 UT (---), 1555 UT (····), and 1556 UT (-·-). The solar flare DEM profiles peak at higher temperatures than do the quiet-Sun DEMs because the flare plasma is hotter than the quiet-Sun plasma, and the flare DEM profiles peak at lower values because the abundance of flare plasma is less than the abundance of quiet-Sun coronal plasma.

3.2. Solar Irradiance

Solar irradiance measured at Earth is defined as the radiance emitted in all directions from the solar disk to the Earth.

$$F(\lambda) = 4\pi \frac{\pi R_s^2}{4\pi R^2} \langle I(\lambda) \rangle = \frac{\pi R_s^2}{R^2} \langle I(\lambda) \rangle \quad (\text{ph s}^{-1}\ \text{cm}^{-2}), \tag{3.9}$$

where R_S (km) is the radius of the Sun, R (km) is the Sun-Earth distance, and $\langle I(\lambda) \rangle$ is the disk averaged radiance which accounts for center-to-limb variations;

$$\langle I(\lambda) \rangle = \frac{2\pi I(\lambda)}{\pi R_s^2} \int_0^{R_s} \frac{I(\lambda, r)}{I(\lambda)} r dr \quad (\text{ph s}^{-1}\ \text{cm}^{-2}\ \text{sr}^{-1}). \tag{3.10}$$

In this equation, $I(\lambda)$ is the radiance of optically thin solar emission lines as defined in Equation 3.8, which is the disk center radiance, and $I(\lambda,r)$ is the radiance at a distance, r, away from the center, where r is the radial distance from the center to the limb. The assumptions are made that the disk averaged radiance only varies along r, the emitting region of the corona is a thin, spherical shell, and no radiation comes from the limb. If $\frac{I(\lambda,r)}{I(\lambda)}=1$, then the brightness would be independent of the emission region position on the Sun, but $\frac{I(\lambda,r)}{I(\lambda)}$ varies as $\frac{1}{\cos(\theta)}$ in the emitting region, where θ is referred to as the heliospheric angle, and θ=0 at disk center and $\theta=\frac{\pi}{2}$ at the solar limb. Substituting into Equation 3.10 gives,

$$\langle I(\lambda) \rangle = \frac{2\pi I(\lambda)}{\pi R_s^2} \int_0^{\pi/2} \frac{1}{\cos(\theta)} R_s^2 \cos(\theta)\sin(\theta) d\theta \quad (\text{ph s}^{-1}\ \text{cm}^{-2}\ \text{sr}^{-1}), \tag{3.11}$$

where a change in variable is made to reflect the dependence on the heliospheric angle,

$$r = R_s \sin(\theta) \tag{3.12}$$

$$dr = R_s \cos(\theta) d\theta. \tag{3.13}$$

Reducing and solving, Equation 3.11 is expressed as

$$\langle I(\lambda) \rangle = 2I(\lambda) \quad (\text{ph s}^{-1}\ \text{cm}^{-2}\ \text{sr}^{-1}), \tag{3.14}$$

where the disk averaged radiance is twice the radiance of optically thin emission lines as defined in Equation 3.8, now including center-to-limb variations. Substituting the disk averaged radiance (Equation 3.14) into the solar irradiance (Equation 3.9),

$$F(\lambda) = \frac{\pi R_s^2}{R^2} 2I(\lambda) \quad (\text{ph s}^{-1}\ \text{cm}^{-2}), \tag{3.15}$$

results in the full-disk solar irradiance measured at Earth from an optically thin emission line at wavelength, λ. The computed DEMs in this work are effective DEMs averaged over the solar disk because the XPS instruments observe the full solar disk irradiance when they observe a solar flare. For the purpose of the research described here, solar flare irradiance is treated through Equations 3.15 and 3.16 as if it distributed across the full solar disk, even though a typical solar flare originates from a local area on the Sun that is smaller than the full solar disk. If the temperature dependent DEM is known, then the solar spectrum can be determined through Equations 3.8 and 3.15. The solar flare plasma DEM, however, is unknown. A DEM is varied until the emission line radiance produces a spectrum that reproduces the XPS photodiode signals. A full explanation of this procedure is found in Section 3.4.

3.3. XPS Photodiode Signal

The solar irradiance from Equation 3.15 is convolved with the XPS photodiode sensitivities (Figures 2.2 and 2.3) to produce a model current i for photodiode k through the equation

$$i_k = \int S_k(\lambda) F(\lambda) q_e A_k d\lambda \quad (\text{A}), \tag{3.16}$$

where $S_k(\lambda)$ is the sensitivity (electron photon^{-1}) of each photodiode k, $F(\lambda)$ is the irradiance calculated from Equation 3.15 at wavelength λ (Å), q_e is the charge of an electron (C electron^{-1}) and A_k is the area (cm^{-2}) of the photodiode k. Equations 3.8, 3.15 and 3.16 are used together in an algorithm to determine spectra of solar flare observations.

3.4. Solar Flare Retrieval Algorithm

The algorithm described here iterates a DEM profile until a solar flare spectrum is produced from Equation 3.15 that reproduces the observed XPS photodiode solar flare current signals from Equation 3.16. The four parameters; XPS diode flare measurements, XPS diode flare measurement uncertainties, initial flare temperatures (T), and initial flare log DEMs, were input to a Levenberg-Marquardt [Levenberg, 1944; Marquardt, 1963] least-squares minimization algorithm to solve for the unknown log DEM values. The iterative technique calculates the solar irradiance based on a DEM profile as a function of temperature; this irradiance in turn is convolved with the XPS photodiode sensitivities to produce a model current. A deviate is calculated for each XPS photodiode channel and a χ^2 value is calculated from the sum of all squared deviates. The DEM profile is adjusted and the iteration continues until the χ^2 value is minimized. The spectrum used to minimize χ^2 in the final iteration is retrieved from the algorithm and is inferred to be the solar flare spectrum. Figure 3.2 outlines how the algorithm functions, and Sections 3.4.1 and 3.4.2 describe the individual steps of the algorithm.

3.4.1. Levenberg-Marquardt Least-Squares Minimization

The solar flare spectral analysis algorithm uses a Levenberg-Marquardt technique to solve a least squares problem by adjusting a set of five parameters to produce a DEM profile that leads to an X-ray spectrum whose observation then reproduces the XPS measurements. The Levenberg-Marquardt technique iteratively searches for the best fit model current values that reproduce the XPS measured current values. The best fit is achieved when the weighted squared difference between the model current and measured current is minimized.

The Levenberg-Marquardt method performs an optimal interpolation using the Taylor series method and the gradient (or steepest decent) method [Marquardt, 1963]. The interpolation is based on the maximum neighborhood in which the truncated Taylor series gives an adequate representation of the nonlinear model [Marquardt, 1963]. A nonlinear least squares fitting algorithm computes estimates of parameters that will

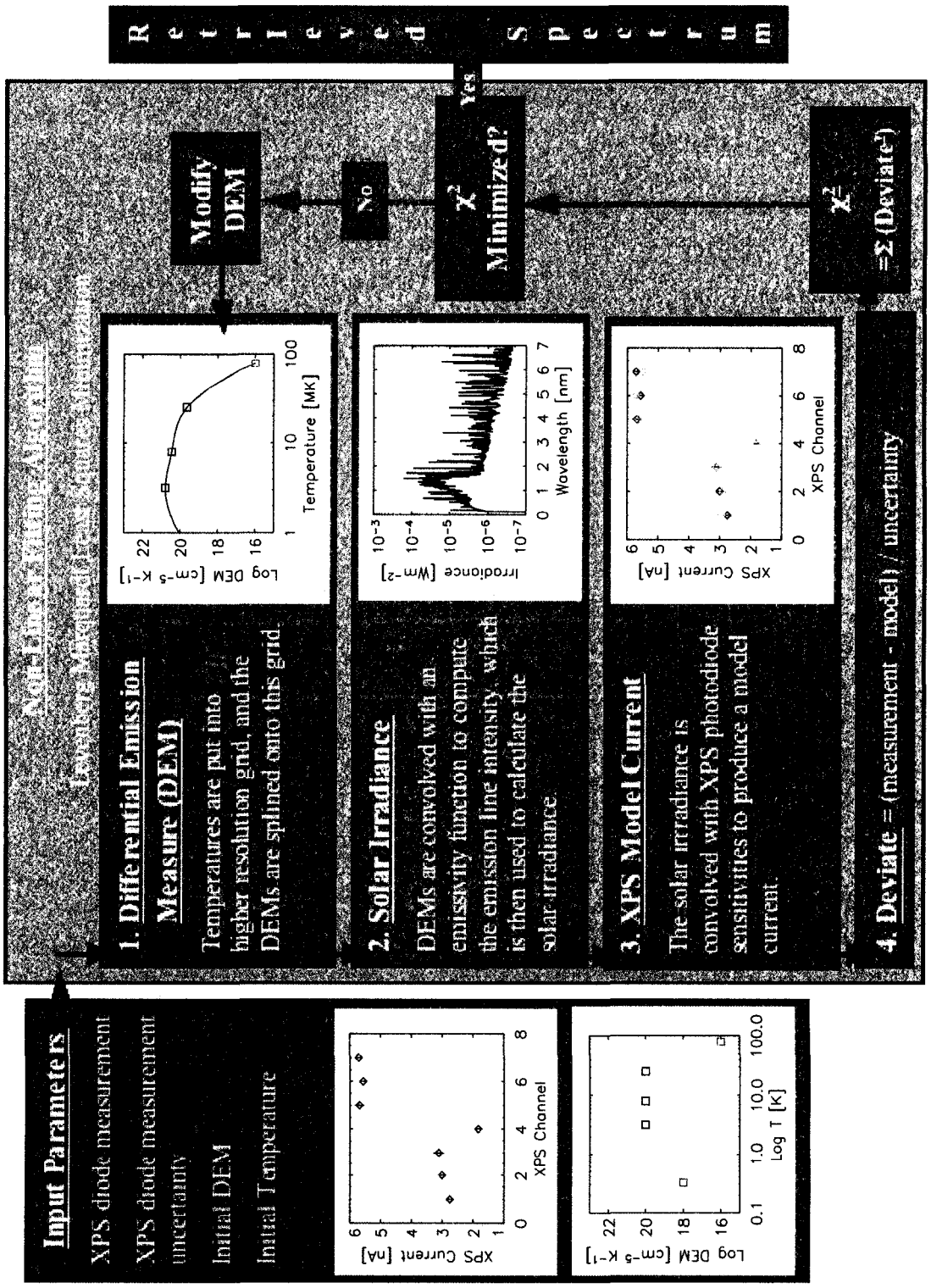

Figure 3.2 Solar flare retrieval algorithm.

$$\phi = \sum_{i=1}^{n} \left[\frac{Y_i - \hat{Y}_i}{\sigma_i} \right]^2, \tag{3.17}$$

minimize the expression where Y_i is a measured value, $\hat{Y}_i$ is a model value, and σ_i is the measurement uncertainty [Marquardt, 1963]. The 'model' is defined from all Equations between 3.1-3.16 that describe the DEM, irradiance and model current calculations. Specifically, the 'model' is summarized through Equations 3.8, 3.15 and 3.16 and repeated here,

$$I(\lambda_{ul}) = \int_T G_{ul}(\lambda,T)\xi(T)dT \quad (\text{ph s}^{-1}\ \text{cm}^{-2}\ \text{str}^{-1}), \tag{3.8}$$

$$F(\lambda) = \frac{\pi R_s^2}{R^2} 2I(\lambda_{ul}) \quad (\text{ph s}^{-1}\ \text{cm}^{-2}), \tag{3.15}$$

$$i_k = \int S_k(\lambda)F(\lambda)q_e A_k d\lambda \quad (\text{A}). \tag{3.16}$$

The flare spectrum of individual observations (Equation 3.15) is determined by interpreting the XPS observations with this 'model' that calculates theoretical spectra from the initial DEM values.

First, the initial temperature and log DEM values are defined with a coarse resolution grid of only five prescribed points. The temperatures are interpolated onto a high resolution grid equally spaced on a log scale and the log DEM values are interpolated onto this grid in the form of a cubic function (step 1 in Figure 3.2). The DEMs are represented as a series of knots that can be controlled by varying the position and magnitude of the initial DEM values. The magnitude of each knot is the base-10 logarithm to make the DEM positive definite. Second, the radiance of a solar emission line is calculated (Equation 3.8) by convolving the DEM with a function related to the emissivity of the atomic transition producing that emission (first part of step 2 in Figure 3.2). The solar emission line radiance is then used to calculate the solar irradiance as described in Equation 3.15 (second part of step 2 in Figure 3.2). Next, the solar irradiance is convolved with the XPS photodiode sensitivities to produce a model current for each XPS detector channel as described in Equation 3.16 (step 3 in Figure 3.2).

Finally, the calculated model current is compared to the XPS measured current through a deviate (step 4 in Figure 3.2) defined as

$$\frac{O_k - E_k}{\sigma_k}, \tag{3.18}$$

where O_k is the XPS measured current of each photodiode k, E_k is the calculated model current of each photodiode k, and σ_k is the uncertainty of the XPS measured current of each photodiode channel. The sum of the squared deviates produces a normalized χ^2 defined as

$$\chi^2 = \sum_{k=1}^{n} \left[\frac{O_k - E_k}{\sigma_k} \right]^2. \tag{3.19}$$

The Levenberg-Marquardt technique minimizes the χ^2 value. If the χ^2 is not minimized, the magnitudes of the log DEMs are modified and the iteration continues. However, if the χ^2 is minimized, meaning the sum of the weighted squared differences between the model and data are minimized, the resulting spectrum is retrieved and convolved with the XPS photodiode sensitivities a final time to produce the best fit model current values. This retrieved spectrum represents the inferred solar flare spectrum. Recall that the measured currents have the background current subtracted so this algorithm solves only for the flare irradiance.

3.4.2. Initial Parameters

Four parameters were input to the solar flare retrieval algorithm; XPS photodiode flare measurements, XPS photodiode flare measurement uncertainties, initial flare temperatures and initial flare log DEMs. The known XPS flare measurements and their uncertainties were described in Chapter 2. An initial flare DEM profile based on prior knowledge must be defined. The initial DEM profile is a 2-D grid of five initial temperatures (0.3, 3.2, 7.9, 25, 79 MK) and five initial log DEM (18, 20, 20, 20, 16) parameters that takes into account the multi-temperature nature of solar flare plasma. Non-isothermal plasma must be considered when determining solar flare spectra because the coronal DEMs constantly change as the plasma is heated and then cools [Acton et. al., 1999]. Plasma temperatures between 0.3-79 MK are responsible for the irradiance

observed by the XPS and therefore are the bounds on the temperature grid described here. The bounds of the log DEM grid were set at 18 and 16 after several preliminary DEM profiles were retrieved from the algorithm following analysis of quiet-Sun and flare DEM.

The 2-D grid of initial temperatures and log DEM values was chosen after several different grids of various temperature and DEM spacings were analyzed. Originally, 19 1-D arrays of varying temperatures between 0.3-79 MK and 20 1-D arrays of varying log DEMs between 16 and 24 were constructed for five different cases. A different number of initial parameters were used in each case in order to determine which initial parameter case provided the most robust results. Robust results are achieved when the retrieved total 0.1-7 nm flare irradiance has the smallest random uncertainty for a parameter case, and the smallest average χ^2 value.

Table 3.1 shows the five different parameter cases. Nine initial parameters were used in case 1, eight initial parameters were used in case 2, seven initial parameters were used in case 3, six initial parameters were used in case 4, and five initial parameters were used in case 5. In all five cases, the parameter endpoints were held fixed and not allowed to vary during the iteration of the solar flare retrieval algorithm. Therefore, only the middle seven, six, five, four or three parameters were allowed to vary during each respective case, thus solving for either seven, six, five, four, or three unknown DEM values. Similar temperatures and log DEM values were used in each grid in order to directly compare analysis results of each case.

Each of the original 19 1-D arrays of varying temperatures and each of the 20 1-D arrays of varying log DEMs were input to the algorithm for all five parameter cases, along with the XPS photodiode flare measurements and uncertainties for the 21 April 2002 X1.5 flare. A 19x20 array of χ^2 values and a 19x20 array of 0.1-7 nm flare irradiance values were determined for each parameter case. The average and standard deviation (1σ) of the χ^2 and 0.1-7 nm flare irradiance distributions were calculated and are shown in Table 3.1. A χ^2 value that represents a good fit can be obtained for all five configurations, meaning that any of the five input parameter cases will reproduce model

Table 3.1 The average and standard deviation (1σ) of the χ^2 and 0.1-7 nm flare irradiance distributions for the 21 April 2002 X1.6 flare resulting from 19 varying temperatures and 20 varying log DEM values for five different input parameter cases. Parameter case 1 provides the most robust 0.1-7 nm flare irradiance results, as it is the flare irradiance that is used to determine the thermospheric NO density enhancement.

Parameter Case	Number of input parameters	χ^2		0.1-7 nm Flare Irradiance [mWm^{-2}]	
		Average	1σ	Average	1σ
1	5 (2 fixed, 3 variable)	6.28	1.33	2.50	0.13
2	6 (2 fixed, 4 variable)	6.66	1.99	2.54	0.14
3	7 (2 fixed, 5 variable)	6.41	1.07	2.53	0.17
4	8 (2 fixed, 6 variable)	8.28	3.32	2.53	0.17
5	9 (2 fixed, 7 variable)	7.08	2.23	2.54	0.18

currents that deviate from the XPS measured currents by only 14-16%. However, it is most important that the algorithm provide robust 0.1-7 nm flare irradiance results, as it is the flare irradiance that is used to determine the thermospheric NO density enhancement.

Parameter case 1 provides the most robust 0.1-7 nm flare irradiance results because it provides the smallest 1σ value of the distribution in flare irradiance, meaning the 0.1-7 nm flare irradiance varies by only 13% for all inputs of this parameter case. Parameter case 1 also provides the smallest average χ^2 value, indicating that using five input parameters where the two endpoints are fixed and the three middle parameters are allowed to vary gives the best agreement between model and measured currents. Varying three input parameters equates to solving for three unknown DEM values. As shown in Figures 2.4 and 2.5, and described in Section 2.1, there are three significant photodiode quiet-Sun spectral bandpasses, 0.1-7 nm, 7-10 nm, and 17-21 nm for the SEE XPS, and 0.1-7 nm, 7-10 nm, and 17-25 nm for the SORCE XPS. Since there are only three unique XPS photodiode spectral bandpasses, only three photodiode channels are required for use in the algorithm to resolve a spectrum by interpreting XPS observations of flares. The SEE and SORCE XPS photodiode measurements were input separately to the algorithm. Seven SEE XPS photodiode measurements and uncertainties were originally used as input to the algorithm. It was then determined that only three unique photodiode channels were required and subsequently only three SORCE XPS photodiode measurements and uncertainties were used as input. Therefore, the solar flare spectral algorithm was run with either seven or three initial XPS photodiode flare measurements and corresponding measurement uncertainties, depending on if the flare was observed by SEE or SORCE.

The XPS photodiodes measure current from mostly a narrow range of flare plasma temperatures as shown in Figure 3.3; temperatures of 3.2 to 25 MK with the peak response near 7.9 MK. These three temperatures were chosen as the initial varying temperatures to the algorithm. The photodiodes are less sensitive between 0.3 and 3.2 MK and between 25 and 79 MK. Therefore, setting initial DEM values in these ranges does not provide realistic results because the photodiodes do not measure current in

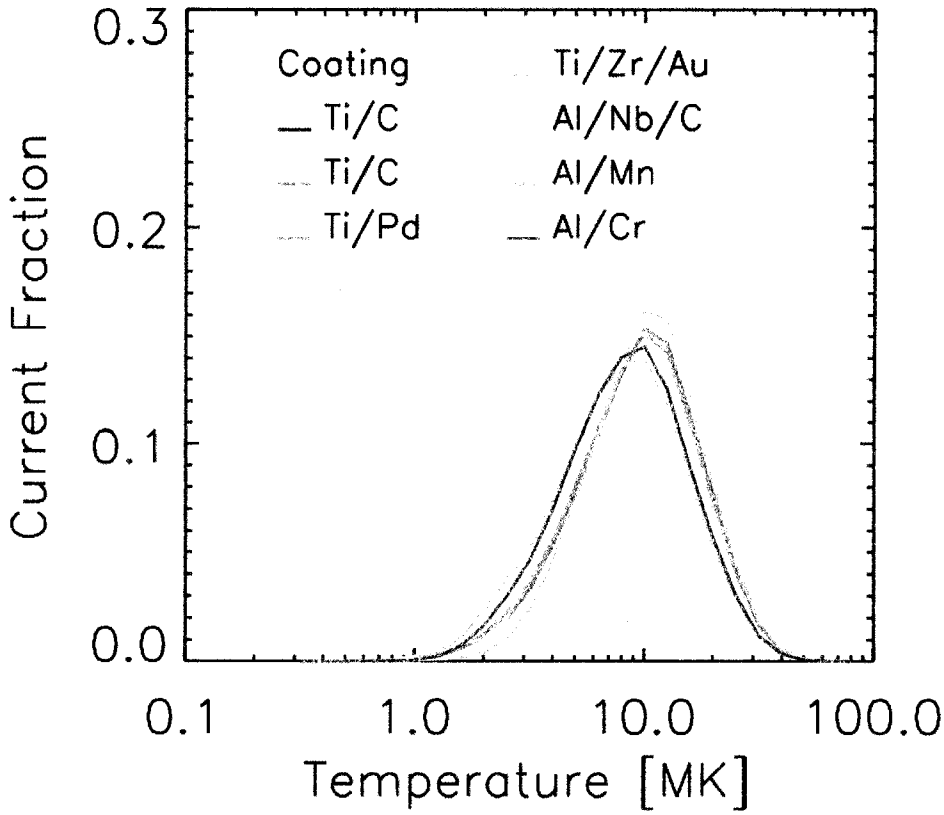

Figure 3.3 The XPS photodiodes measure current from mostly a narrow range of flare plasma temperatures. Most of the photodiode current comes from temperatures of 3.2 to 25 MK with the peak response near 7.9 MK. This photodiode response is for the 21 April 2002 X1.6 flare and the photodiode response of most of the 118 flares is similar.

these temperature ranges. This photodiode response is for the 21 April 2002 X1.6 flare and the photodiode response of most of the 118 flares is similar. However, if a retrieved flare DEM indicates flare plasma in the cooler temperature range of 0.3 to 3.2 MK or in the hotter temperature range of 25 to 79 MK, then the XPS photodiodes do measure currents in those temperature ranges. The photodiode current fraction for the 26 February 2002 C6.3 flare in Figure 3.4 shows a XPS current response in these cooler and hotter temperature regions. Photodiode responses such as this are similar to only a few of the 118 observed flares.

The coolest temperature of 0.3 MK is set at an arbitrary log DEM value of 18 to maintain a downward slope from the hotter peak temperature of the DEM profile, and the hottest temperature of 79 MK is set at an arbitrary log DEM value of 16 to maintain a downward slope from the peak temperature of 7.9 MK. The chosen initial temperatures, (0.3, 3.2, 7.9, 25, 79 MK), the chosen initial log DEM values (18, 20, 20, 20, 16), and the individual XPS photodiode solar flare measurements and uncertainties were used to determine all 118 flare spectra. The algorithm was run one time per flare; therefore, it was run a total of 118 times.

3.5. Algorithm Results

The solar flare spectral analysis algorithm was run for all flares observed by the XPS to determine the spectrum of each flare observation. The results of four solar flares are presented in detail in Sections 3.5.1-3.5.4, where each of the featured flares represents a different flare classification (C, M, X, and very large X). The random and systematic uncertainties of the retrieved solar flare spectra are presented in Section 3.5.5. The algorithm retrieves unique flare irradiances for wavelengths between 0.1-7 nm for X, M and C-class flares as described in Section 3.5.6. Section 3.5 concludes with comparisons of retrieved flare irradiances to the observed GOES flare irradiances in Section 3.5.7.

3.5.1. 5 June 2002 C3.4 Solar Flare

SEE XPS channel #2 (Ti/C) detected a flare enhancement on 5 June 2002 that was 20% times greater than the background observations. Figure 3.5 shows the observed

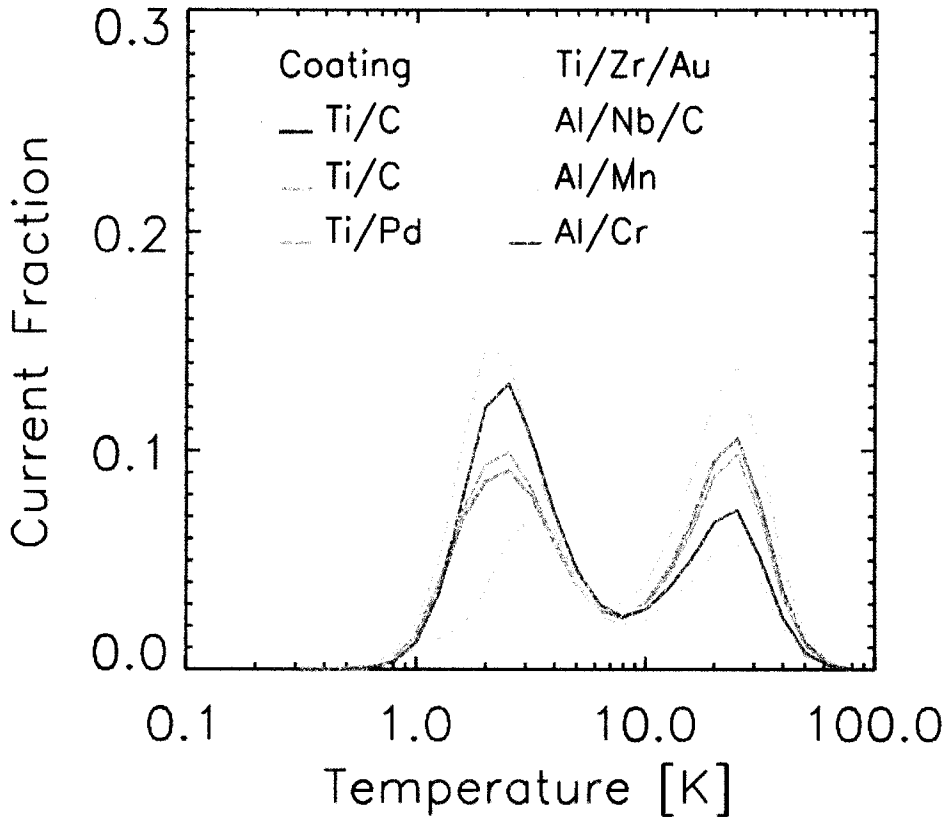

Figure 3.4 If a retrieved flare DEM indicates flare plasma in the cooler temperature range of 0.3 to 3.2 MK or in the hotter temperature range of 25 to 79 MK, then the XPS photodiodes measure current in those temperature ranges. This photodiode response is for the 26 February 2002 C6.3 flare, and the photodiode response of a few of the 118 flares is similar.

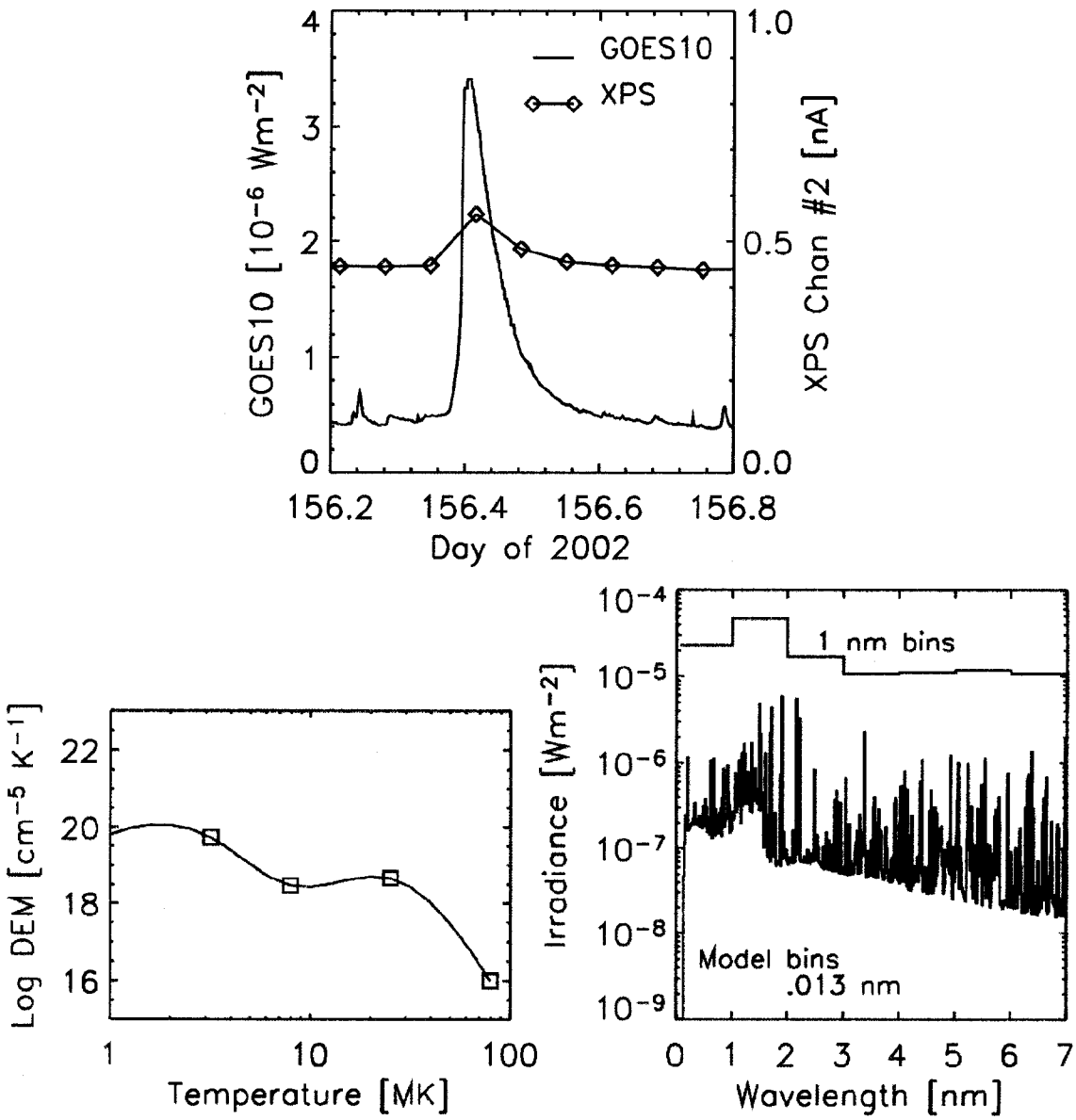

Figure 3.5 [Top] SEE XPS channel #2 first observed the 5 June 2002 C3.4 flare (0959 UT) 19 minutes after GOES-10 (0.1-0.8 nm) observed the peak of the flare (0940 UT), and observed the effects over the next 5 hours. [Left] The best fit C3.4 flare DEM profile. [Right] The retrieved C3.4 flare spectrum between 0.1-7 nm. Most of the soft X-ray irradiance comes from the 1-2 nm range, which begins to dominate the solar soft X-ray spectrum.

XPS channel #2 response during the flare along with the GOES-10 0.1-0.8 nm irradiance. The low duty cycle of the XPS is evident compared to the continuous GOES-10 observations; however, all SEE channels observed this flare enhancement. SEE XPS channel #2 first observed the C3.4 flare (0959 UT) 19 minutes after GOES-10 observed the peak of the flare (0940 UT), and observed the effects over the next 5 hours. Model results are given in Table 3.2, which shows the model current compared to the measured current and the absolute uncertainty of each photodiode channel for the flare observation.

Figure 3.5 showed the best fit DEM profile obtained through the iteration process. A quiet-Sun DEM profile has a temperature peak near 1 MK (Figure 3.1) while the DEM profile in Figure 3.5 peaked near temperatures of 2 and 20 MK, which indicates the C3.4 flare plasma is hotter than the quiet-Sun plasma. The magnitude of the temperature peak at 2 MK is 7% greater than the magnitude of the temperature peak at 20 MK, which signifies that most of the flare plasma is at 2 MK. The four boxes on the DEM profile represent four of the initial temperature parameters that were input to the algorithm, and the corresponding final log DEM values after the iteration. Figure 3.5 also showed the retrieved C3.4 flare spectrum between 0.1-7 nm in both the high resolution binning used in this modeling as well as 1 nm binning commonly used in atmospheric modeling. Most of the soft X-ray irradiance comes from the 1-2 nm range, which begins to dominate the solar soft X-ray spectrum. The increase in the 1-2 nm range is mostly due to the emergence of highly ionized iron emission lines in the solar corona at temperatures of 3.2 MK.

3.5.2. 22 March 2002 M1.8 Solar Flare

The flare enhancement on 22 March 2002 was 2 times greater than the background observations, as detected by SEE XPS channel #2 (Ti/C). All SEE channels observed this flare enhancement and Figure 3.6 shows the observed XPS channel #2 response during the flare along with the GOES-10 0.1-0.8 nm irradiance. SEE XPS channel #2 first observed the M1.8 flare (1146 UT) 35 minutes after GOES-10 (0.1-0.8 nm) observed the peak of the flare (1111 UT), and observed the effects over the next 3 hours.

Table 3.2 Model currents, measured currents, and absolute uncertainties for each photodiode channel during the 5 June 2002 C3.4 solar flare.

XPS Channel	Filter Coating	Measured Current [nA]	Absolute Uncertainties [nA]	Model Current [nA]
1	Ti/C	0.10	0.11	0.12
2	Ti/C	0.12	0.11	0.12
5	Ti/Pd	0.12	0.44	0.13
6	Ti/Zr/Au	0.07	0.27	0.07
7	Al/Nb/C	0.28	0.31	0.24
9	Al/Mn	0.26	0.15	0.27
10	Al/Cr	0.26	0.16	0.23

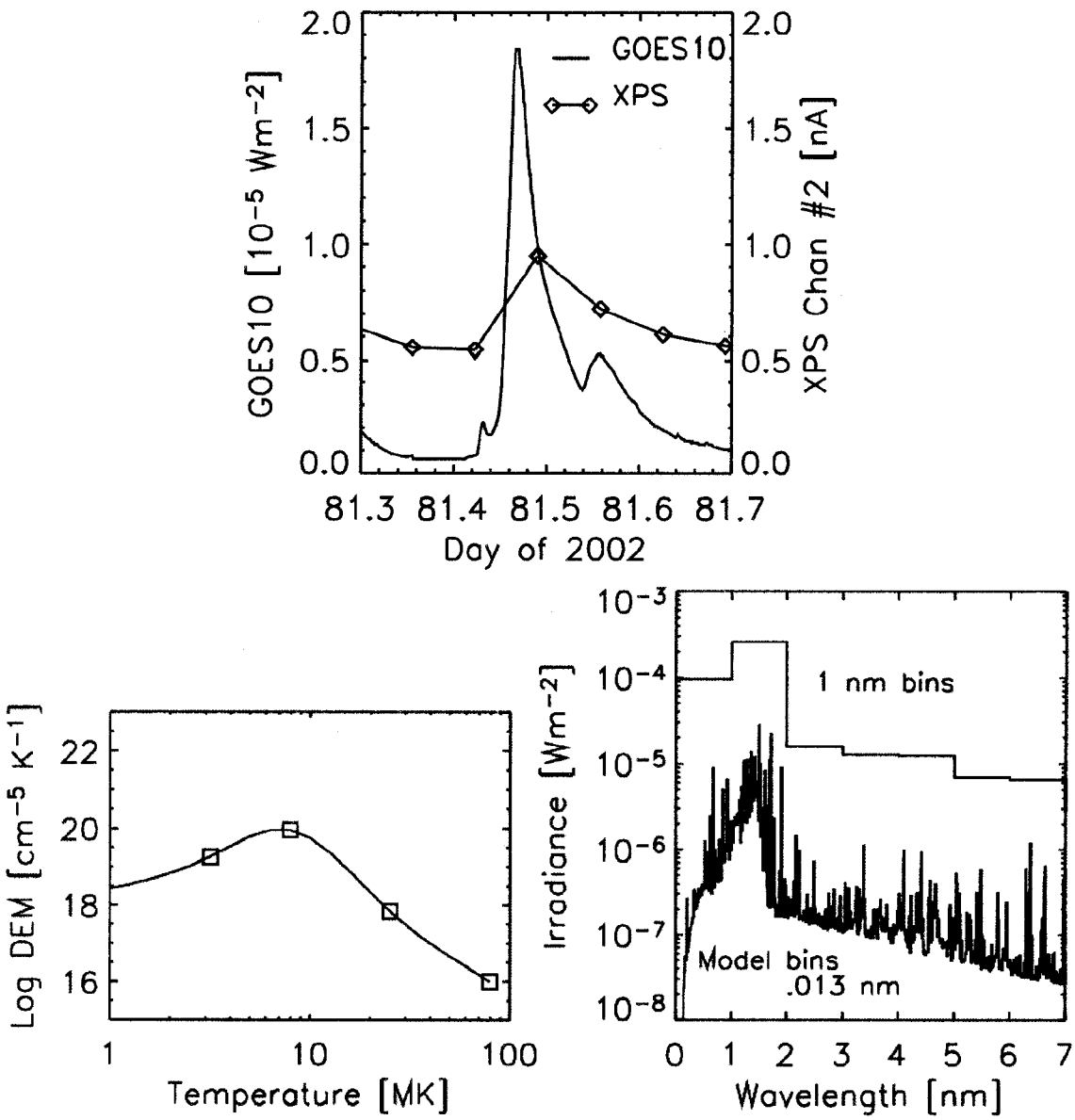

Figure 3.6 [Top] SEE XPS channel #2 first observed the 22 March 2002 M1.8 flare (1146 UT) 35 minuets after GOES-10 (0.1-0.8 nm) observed the peak of the flare (1111 UT), and observed the effects over the next 3 hours. [Left] The best fit M1.8 flare DEM profile. [Right] The retrieved M1.8 flare spectrum 0.1-7 nm. Most of the soft X-ray irradiance comes from the 1-2 nm range, which dominates the solar soft X-ray spectrum.

Table 3.3 shows the model current compared to the measured current and the absolute uncertainty of each photodiode channel for the flare observation.

Figure 3.6 showed that the best fit DEM profile peaks at 7 MK, which indicates that the bulk of the M1.8 flare plasma is at a hotter temperature than the quiet-Sun and C3.4 DEM profiles. The M1.8 DEM profile has a similar shape as the M2 flare DEM described previously in Figure 3.1, but peaks at a cooler temperature because the M1.8 DEM is found for an observation that was 35 minutes after the peak of the flare, while the M2 flare DEM was obtained during and immediately following the flare peak. The flare plasma cooled in the 35 minutes since the peak of the flare was observed by GOES-10. Figure 3.6 also showed the retrieved M1.8 flare spectrum, which indicates most of the soft X-ray irradiance comes from the 1-2 nm range, which dominates the solar soft X-ray spectrum. The magnitude of the 1-2 nm flare irradiance is six times greater than the C3.4 flare 1-2 nm irradiance because there is more flare plasma at temperatures equal to and greater than 3.2 MK, at which temperature the emergence of highly ionized iron emission lines in the solar corona becomes dominant.

3.5.3. 21 April 2002 X1.6 Solar Flare

SEE XPS channel #2 (Ti/C) detected a flare enhancement on 21 April 2002 that was 5 times greater than the background observations. All SEE channels observed this flare enhancement, and Figure 3.7 shows the observed XPS channel #2 response during the flare. SEE XPS channel #2 first observed the X1.6 flare (0213 UT) 27 minutes after GOES-10 observed the peak of the flare (0146 UT), and observed the effects over the next 7 hours. The integrated current response over the course of the flare is approximately equal to the integral current over the previous 24-hour period. This is significant for the Earth's atmosphere because it suggests that this large flare deposited as much 0.1-7 nm energy during 7 hours as the Sun normally deposits during a full day. This result has implications for the photochemistry of the lower thermosphere.

Table 3.4 shows the model current compared to the measured current and the absolute uncertainty of each photodiode channel for the observation. The best fit DEM profile in Figure 3.7 peaks near 3 and 15 MK. The log DEM magnitude at these peaks is

Table 3.3 Model currents, measured currents, and absolute uncertainties for each photodiode channel during the 22 March 2002 M1.8 solar flare.

XPS Channel	Filter Coating	Measured Current [nA]	Absolute Uncertainties [nA]	Model Current [nA]
1	Ti/C	0.37	0.12	0.44
2	Ti/C	0.41	0.12	0.43
5	Ti/Pd	0.44	0.33	0.46
6	Ti/Zr/Au	0.23	0.22	0.28
7	Al/Nb/C	0.95	0.31	0.90
9	Al/Mn	0.88	0.14	0.86
10	Al/Cr	0.89	0.15	0.85

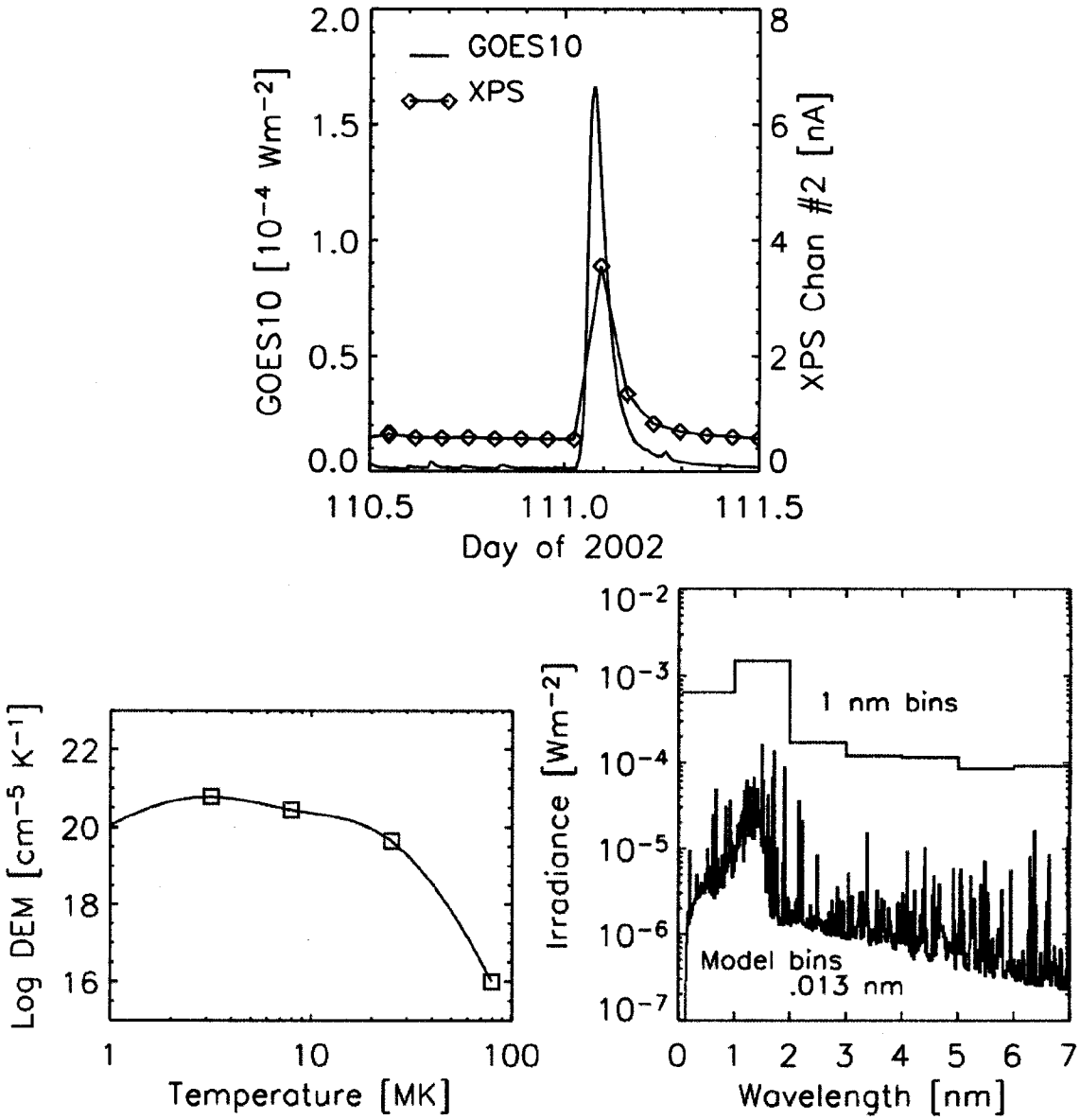

Figure 3.7 [Top] SEE XPS channel #2 first observed the 21 April 2002 X1.6 flare (0213 UT) 27 minutes after GOES-10 (0.1-0.8 nm) observed the peak of the flare (0146 UT), and observed the effects over the next 7 hours. [Left] The best fit X1.6 flare DEM profile. [Right] The retrieved X1.6 flare spectrum between 0.1-7 nm. Most of the soft X-ray irradiance comes from the 1-2 nm range, which dominates the solar soft X-ray spectrum.

Table 3.4 Model currents, measured currents, and absolute uncertainties for each photodiode channel during the 21 April 2002 X1.6 solar flare.

XPS Channel	Filter Coating	Measured Current [nA]	Absolute Uncertainties [nA]	Model Current [nA]
1	Ti/C	2.76	0.12	2.93
2	Ti/C	3.00	0.12	2.90
5	Ti/Pd	3.11	0.33	3.10
6	Ti/Zr/Au	1.84	0.21	1.83
7	Al/Nb/C	5.69	0.32	5.65
9	Al/Mn	5.57	0.15	5.72
10	Al/Cr	5.71	0.16	5.49

higher than the magnitudes of the quiet-Sun, C3.4 and M1.8 flare DEM profiles, indicating that the X1.6 flare released more flare plasma at a range of hot temperatures. Figure 3.7 also showed the retrieved X1.6 flare spectrum. Again, most of the soft X-ray irradiance comes from the 1-2 nm range, which dominates the solar soft X-ray spectrum. The magnitude of the 1-2 nm flare irradiance is six times greater than the M1.8 flare 1-2 nm irradiance and 40 times greater than the C3.4 flare 1-2 nm irradiance. This is due to the increased flare plasma at temperatures equal to and greater than 3.2 MK, at which temperature the emergence of highly ionized iron emission lines becomes dominant.

3.5.4. 28 October 2003 X18 Solar Flare

SORCE XPS channel #3 (Al/Sc/C) detected a flare enhancement on 28 October 2003 that was 15 times greater than the background observations. All SORCE XPS channels observed this flare several times during the duration of the flare, and Figure 3.8 shows the observed XPS channel #3 response during the flare along with the GOES-10 irradiance. SORCE XPS channel #3 observed the X18 flare (1112 UT) 3 minutes after GOES-10 (0.1-0.8 nm) observed the peak of the flare (1109 UT), and observed the effects over the next hour. Again, the integrated current response over the course of the flare is approximately equal to the integral current over the previous 24-hour period, which suggests that this very large flare deposited as much 0.1-7 nm energy in an hour as the Sun normally deposits during a full day.

Table 3.5 shows the model current compared to the measured current and the absolute uncertainty of each photodiode channel for the observation. Figure 3.8 shows the best fit DEM profile that is obtained. The X18 DEM profile peaks near 3 and 15 MK but at larger magnitudes than does the X1.6 DEM profile, indicating the X18 flare plasma is hotter than the X1.6 flare plasma. The 1-2 nm X18 flare irradiance is five times greater than the X1.6 flare irradiance, because more flare plasma at temperatures equal to and greater than 3.2 MK lead to the emergence of more spectral lines in the 1-2 nm as is shown in the retrieved flare spectrum Figure 3.8.

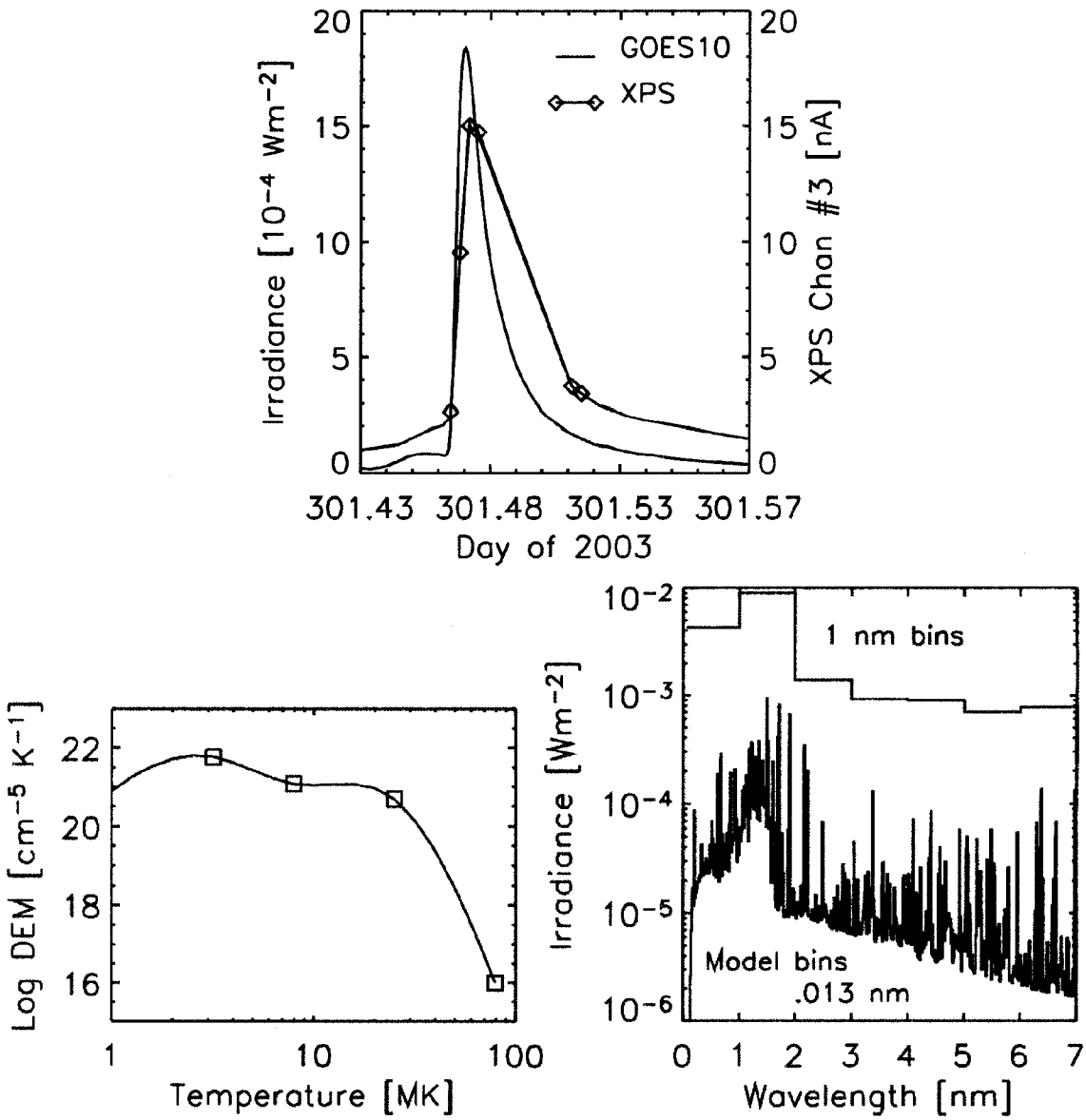

Figure 3.8 [Top] SORCE XPS channel #3 observed the 28 October 2003 X18 flare (1112 UT) 3 minutes after GOES-10 (0.1-0.8 nm) observed the peak of the flare (1109 UT), and observed the effects over the next hour. [Left] The best fit X18 flare DEM profile. [Right] The retrieved X18 flare spectrum between 0.1-7 nm. Most of the soft X-ray irradiance comes from the 0.1-2 nm range, which dominates the solar soft X-ray spectrum.

Table 3.5 Model currents, measured currents, and absolute uncertainties for each photodiode channel during the 28 October 2003 X18 solar flare.

XPS Channel	Filter Coating	Measured Current [nA]	Absolute Uncertainties [nA]	Model Current [nA]
2	Ti/C	6.82	0.12	6.51
3	Al/Sc/C	14.8	0.18	14.8
6	Ti / Mo / Au	3.48	0.15	4.32

3.5.5. Uncertainty of Results

The random error component of the uncertainty of the retrieved solar flare spectra and DEM comes from two sources: the photodiode measurement uncertainty and the numerical method uncertainty. As previously discussed, various spacings for the temperature and log DEM grid were used until the most robust configuration was determined. Several different input configurations were tried in the algorithm resulting in several retrieved spectra representing the inferred solar flare spectrum. The average and standard deviation (1-σ) 0.1-7 nm flare irradiance distributions for the 21 April 2002 X1.6 flare resulting from 19 varying temperature and 20 varying log DEM values were calculated using various implementations of the chosen parameter case 1 configuration. Parameter case 1 uses five input parameters where the endpoints remained fixed and the three middle parameters are allowed to vary.

The 0.1-7 nm irradiance was found to vary by 5% (one standard deviation). The random average diode measurement uncertainty is approximately 5%. Thus, the total root mean squared random error component of the uncertainty of the inferred solar flare spectrum is approximately 7%. This uncertainty is in addition to the systematic error of the photodiode calibration, which ranges from 5%-10% [Woods et al., 1999; 2005b] and is variable with wavelength. There are also uncertainties in the model, which are difficult to quantify, that can come from such sources as uncertainties in assumed properties of the solar atmosphere. The uncertainties in the results of the 21 April 2002 flare are similar for all observed flares.

3.5.6. Uniqueness of Solution

The uniqueness of the flare retrieval algorithm results was determined by retrieving several spectra after randomly varying the initial photodiode measurement parameters by small amounts. The retrieved model current values for the 21 April 2002 X1.6 flare (Table 3.4) are perturbed by values up to 45% of the retrieved model current, and are generated from a random number function. The random number function provides normally-distributed numbers with a mean of zero and a standard deviation of one. Each

random number generated was scaled according to the uncertainty of each photodiode measurement and added to the model current. The perturbed model currents were then used as the initial parameters to the algorithm from which a different DEM, solar flare spectrum, and model current were retrieved. The model current values were randomly perturbed and input to the algorithm 1000 times to determine how well the original retrieved flare spectrum was reproduced.

Figure 3.9 shows histograms of the retrieved 0.1-2 nm and 0.1-7 nm irradiances of all 1000 samples from the iterations of the algorithm using perturbed values of the model current. The irradiance distributions in Figure 3.9 are well centered about a mean irradiance, suggesting the flare spectrum is of good precision. Even as the initial model current values are perturbed, most of the 0.1-2 nm irradiance is concentrated near 1.9 mW m^{-2} and most of the 0.1-7 nm irradiance is concentrated near 2.5 mW m^{-2}. The 0.1-2 nm irradiance distribution has a standard deviation of 0.09 mW m^{-2} (5% of the mean) and the 0.1-7 nm irradiance distribution has a standard deviation of 0.14 mW m^{-2} (5% of the mean). The error calculated in each plot is the standard deviation of the distribution divided by the average irradiance of the distribution. Both errors are small indicating a robust solution for these wavelength ranges. Figure 3.9 shows that most of the 0.1-7 nm solar flare irradiance comes from the 0.1-2 nm range and that the algorithm retrieves a stable and unique flare irradiance for wavelengths between 0.1-7 nm. Therefore, all retrieved solar flare spectra are presented for wavelengths less than 7 nm. Figure 3.10 shows a histogram of the retrieved 7-20 nm flare irradiances of all 1000 samples of the algorithm. Here, the irradiance is not well centered near a mean value and is spread out throughout the distribution. This irradiance distribution has a larger error of 29% with a standard deviation of 0.24 mW m^{-2}, indicating a non-unique solution. Therefore, retrieved solar flare spectra are not presented for wavelengths greater than 7 nm. The irradiance distribution results for a C and M-class flare are similar to that of the X-class flare. Unique 0.1-2 and 0.1-7 nm flare irradiances are retrieved with errors greater than for X-class flares because M-class and especially C-class flares are closer to the background photodiode current measurements.

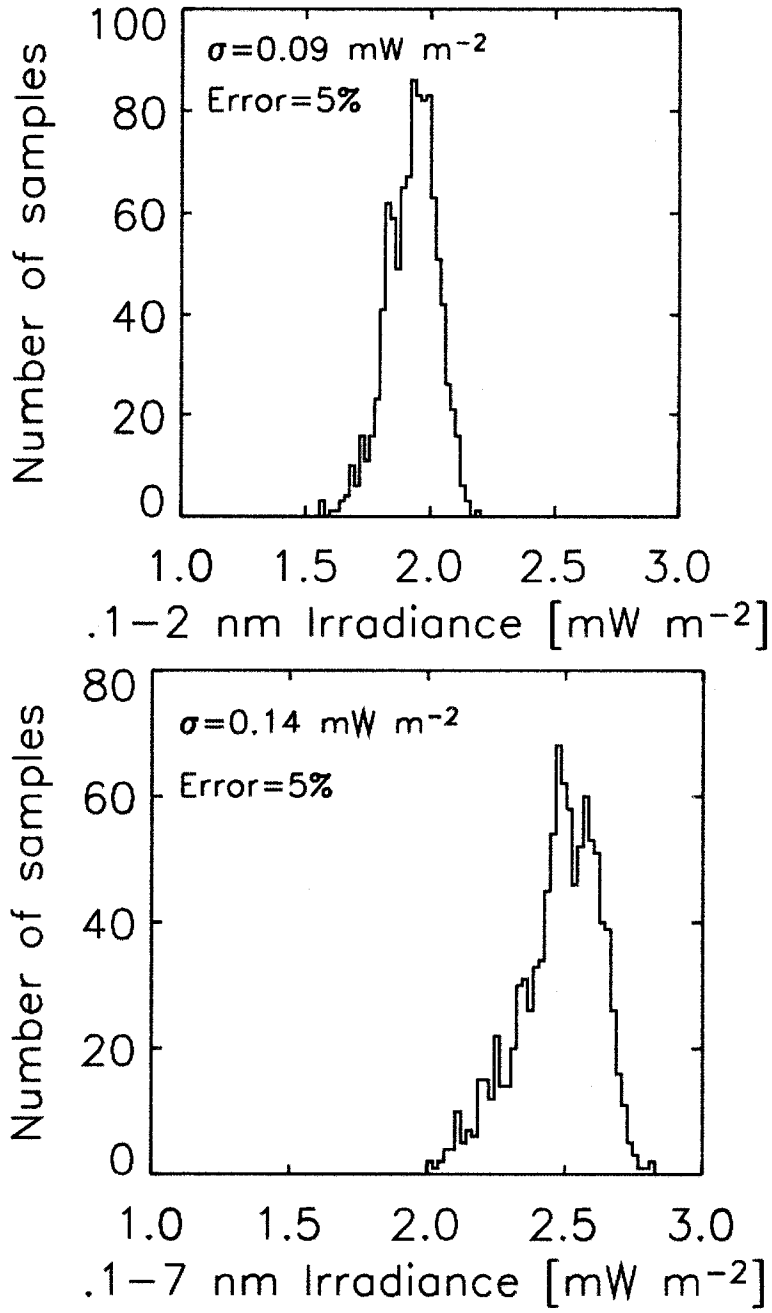

Figure 3.9 Histograms of retrieved 0.1-2 and 0.1-7 nm irradiance for 1000 samples of perturbed initial photodiode model currents iterations reproducing the 21 April 2002 X1.6 flare spectrum. The algorithm retrieves a unique flare irradiance for wavelengths between 0.1-7 nm.

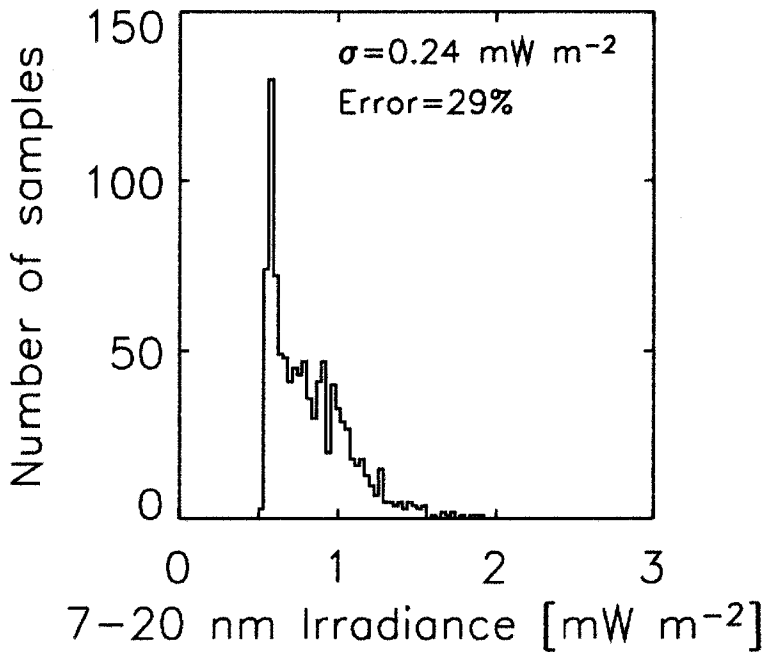

Figure 3.10 Histogram of retrieved 7-20 nm irradiance for 1000 samples of perturbed initial photodiode model current iterations reproducing the 21 April 2002 X1.6 flare spectrum. The algorithm does not retrieve a unique flare irradiance for wavelengths between 7-20 nm.

3.5.7. Comparisons to GOES Irradiance

Since there are no spectral measurements of the irradiance during a flare that are coincident with the observations described in the preceding sections, it is not possible to fully validate these results. One partial validation, however, is to compare the 0.1-0.8 nm flare irradiances obtained in this work with those observed by the GOES XRS. The GOES-10 irradiance was calculated for each of the 118 flare observations from the best fit DEM results. A routine provided by Warren [2006] was used that takes emission measures and temperatures as input to produce an expected GOES-10 irradiance based on the properties of the XRS instrument [Hanser and Sellers, 1996]. Each temperature in the grid and the appropriately scaled corresponding DEM for that temperature was input into this routine to yield an irradiance, and the results were summed. This routine compares each input temperature to a table of temperatures computed by integrating the GOES-10 transfer function over a CHIANTI 5.1 [Dere et al., 1997; Landi et al., 2006] spectral model assuming coronal abundances of Feldman et al. [1992] and ionization balances of Mazzotta et al. [1998]. This routine would be analogous to the GOES_FLUXES.PRO routine from the SOLARSOFT software database [Freeland and Bentley, 2000] if one existed that incorporated the most recent version of the CHIANTI atomic database for emission lines. In order to avoid confusion from small variations between different GOES satellite calibrations, only GOES-10 reported observations and the calculated irradiances from the GOES-10 transfer function were used. This routine does not include a normalization factor of 0.7 by which the GOES-10 XRS data could be multiplied to bring the data in line with data from earlier XRS instruments [Hanser and Sellers, 1996].

Figure 3.11 compares the calculated 0.1-0.8 nm irradiance to the observed GOES-10 0.1-0.8 nm irradiance for all 118 solar flares. The solid line represents perfectly matched XPS and XRS results. The calculated irradiances of dimmer M-class and C-class flares are in good agreement with the observed irradiances. Results for brighter M-class and X-class flares are in less agreement with calculated irradiances up to a factor of 2 less than the GOES observed irradiances. The calculated irradiances were computed with the

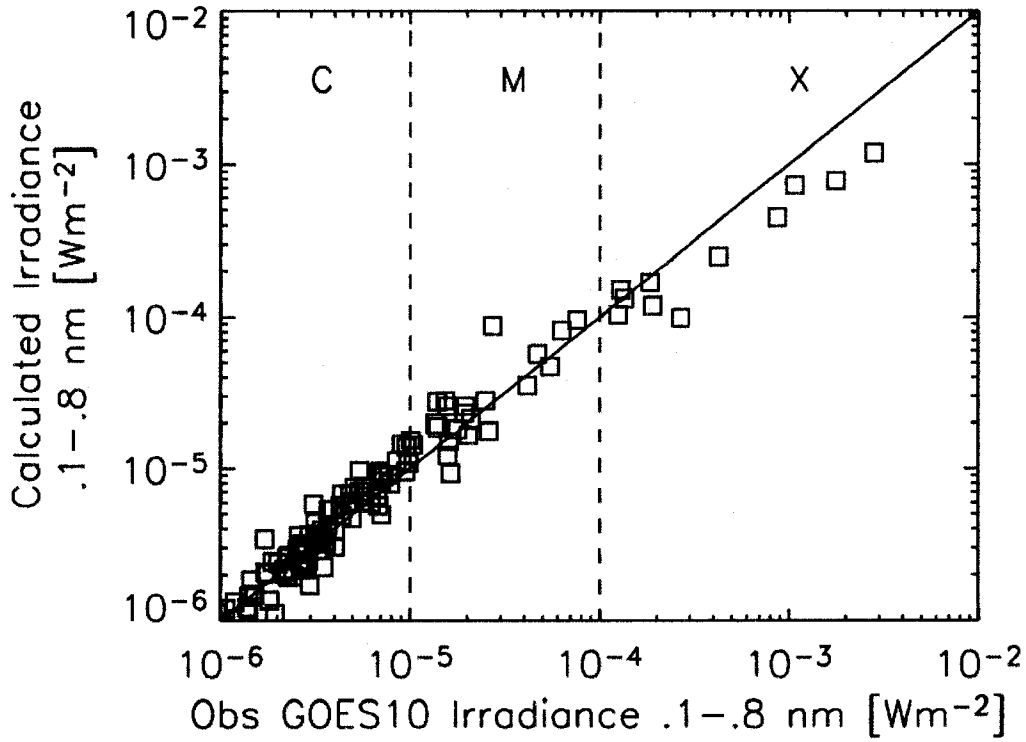

Figure 3.11 The calculated XPS 0.1-0.8 nm irradiance compared to the GOES-10 0.1-0.8 nm irradiance observed at the time of the XPS observation. The calculated irradiances of dimmer M-class and C-class flares are in good agreement with the observed irradiances. Results for brighter M-class and X-class flares are in less agreement with calculated irradiances that are up to a factor of 2 less than the GOES observed irradiances.

same coronal abundances and ionization balances as used in the described algorithm; however, different atomic models were used. The differences between the APED and CHIANTI spectral models are likely to be small. Overall, the agreement between the XPS and GOES results is good. If the calculated 0.1-0.8 nm irradiances were multiplied by the normalization factor of 0.7 [Hanser and Sellers, 1996; Hill et al., 2005], there would be lesser agreement of the dimmer flares with the observed GOES-10 XRS data and the brighter flares would be a factor of 3 less than the observed GOES-10 irradiance.

Figure 3.12 displays the retrieved XPS 0.1-7 nm integrated irradiance relative to the simultaneously observed GOES-10 0.1-0.8 nm irradiance for all 102 flares observed by SEE and the 16 flares observed by SORCE. The XPS 0.1-7 nm irradiance was calculated at the time when the XPS observes the flare, which is rarely at the peak of the flare. Table 2.1 listed the XPS flare observation time compared to the peak time of all 102 flares observed by SEE, and Table 2.2 listed the XPS flare observation time compared to the peak time of the 16 flares observed by SORCE. These tables also listed the XPS 0.1- 0.8 nm, 0.1-2 nm and 0.1-7 nm irradiances of all flares. The range of 0.1-7 nm is chosen because it is a bandpass used by both SNOE [Bailey et al., 2000; 2001; 2005], SEE [Woods et al., 2003; 2005a], and SORCE [Woods et al., 2005b], and most of the flare photodiode signal comes from wavelengths between 0.1-7 nm. Returning to Figure 3.12, the flare 0.1-7 nm irradiance is well correlated with the shorter wavelength irradiance observed by GOES. A best fit line is shown that has an equation of $Y = (220 \pm 0.2)x10^{-2} * X^{(800 \pm 0.2)x10^{-3}} + (7.6 \pm 1.1)x10^{-7}$ Wm^{-2}. The solid line is near linear, and provides a way to correlate observed GOES flare irradiances with the 0.1-7 nm flare irradiance. Figure 3.12 also shows the range of 0.1-7 nm quiet-Sun irradiance over the six month period in 2002 and the fall of 2003 as measured by the XPS, and is represented by grey hash marks. M-class flares produce a 0.1-7 nm irradiance approximately equal in magnitude to the quiet-Sun irradiance, thus doubling the irradiance, while smaller X-class flares (X1-X5) calculated at the time of the XPS observation provide 2-3 times the energy of the quiet-Sun 0.1-7 nm irradiance, and

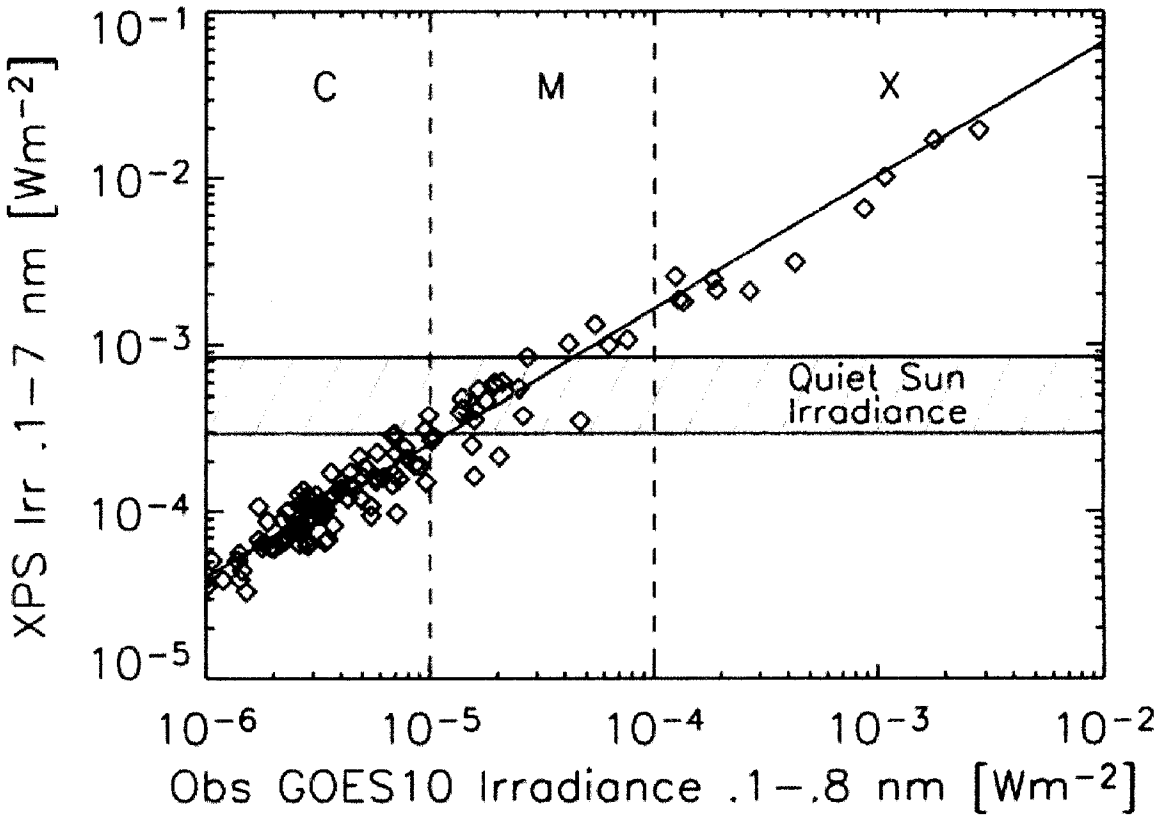

Figure 3.12 XPS irradiance between 0.1-7 nm for the 102 flares observed by all SEE XPS channels and the 16 flares observed by all SORCE XPS channels. The range of quiet-Sun irradiance is represented by grey hash marks. The total 0.1-7 nm irradiance of smaller X-class flares (X1-X5) calculated at the time of the XPS observation provides 2-3 times the energy of the quiet-Sun 0.1-7 nm irradiance, and the total 0.1-7 nm irradiance of larger X-class flares (X5-X30) provides 7-22 times the energy of the quiet-Sun 0.1-7 nm irradiance.

larger X-class flares (X5-X30) provide 7-22 times the energy of the quiet-Sun 0.1-7 nm irradiance.

Figure 3.13 displays the retrieved XPS 0.1-2 nm integrated irradiance relative to the simultaneously observed GOES-10 0.1-0.8 nm irradiance for all flares. The flare 0.1-2 nm irradiance is also well correlated with the shorter wavelength irradiance observed by GOES. A best fit line is shown that has an equation of $Y = (260 \pm 0.6)x10^{-2} * X^{(800 \pm 0.4)x10^{-3}} + (9.8 \pm 5.8)x10^{-7}$ Wm^{-2}. Again, the solid line is near linear and provides a way to correlate observed GOES flare irradiances with the 0.1-2 nm flare irradiance. C-class flares produce a 0.1-2 nm irradiance approximately equal in magnitude to the quiet-Sun irradiance, thus doubling the irradiance, while M-class flares provide up to 4.5 times the energy of the quiet-Sun 0.1-2 irradiance. Smaller X-class flares (X1-X5) calculated at the time of the XPS observation provide 7-13 times the energy of the quiet-Sun 0.1-2 nm irradiance, and larger X-class flares (X5-X30) provide 27-75 times the energy of the quiet-Sun 0.1-2 nm irradiance. There is little difference (less than a factor of 1.3) between the 0.1-2 nm irradiance and 0.1-7 nm irradiance provided from the 102 flares observed by SEE and less than a factor of 1.4 between the 0.1-2 nm irradiance and 0.1-7 nm irradiance provided from the 16 flares observed by SORCE. This shows that most of the 0.1-7 nm irradiance during solar flares comes from the 0.1-2 nm wavelength range.

3.6. Solar Flare Soft X-ray Energy Deposition

Solar flares enhance the soft X-ray irradiance in the 0.1-2 nm range, as was shown in Figures 3.5-3.8. Most of the excess 0.1-2 nm irradiance comes from 1-2 nm, thus solar flares deposit most of their energy between 100-110 km in the thermosphere where 1-2 nm photons are absorbed. The magnitude and spectral shape of the solar irradiance determines at which altitudes the solar energy is deposited, and the atmospheric constituents at those altitudes determine the absorption rate of the solar irradiance. The atmospheric absorption rate is the change in solar irradiance with respect to altitude,

$$\frac{df(\lambda,z)}{dz} = \sum_k n_k(z)\sigma_k^a(\lambda)f(\lambda,z), \quad (\mathrm{W\ m^{-3}}) \tag{3.20}$$

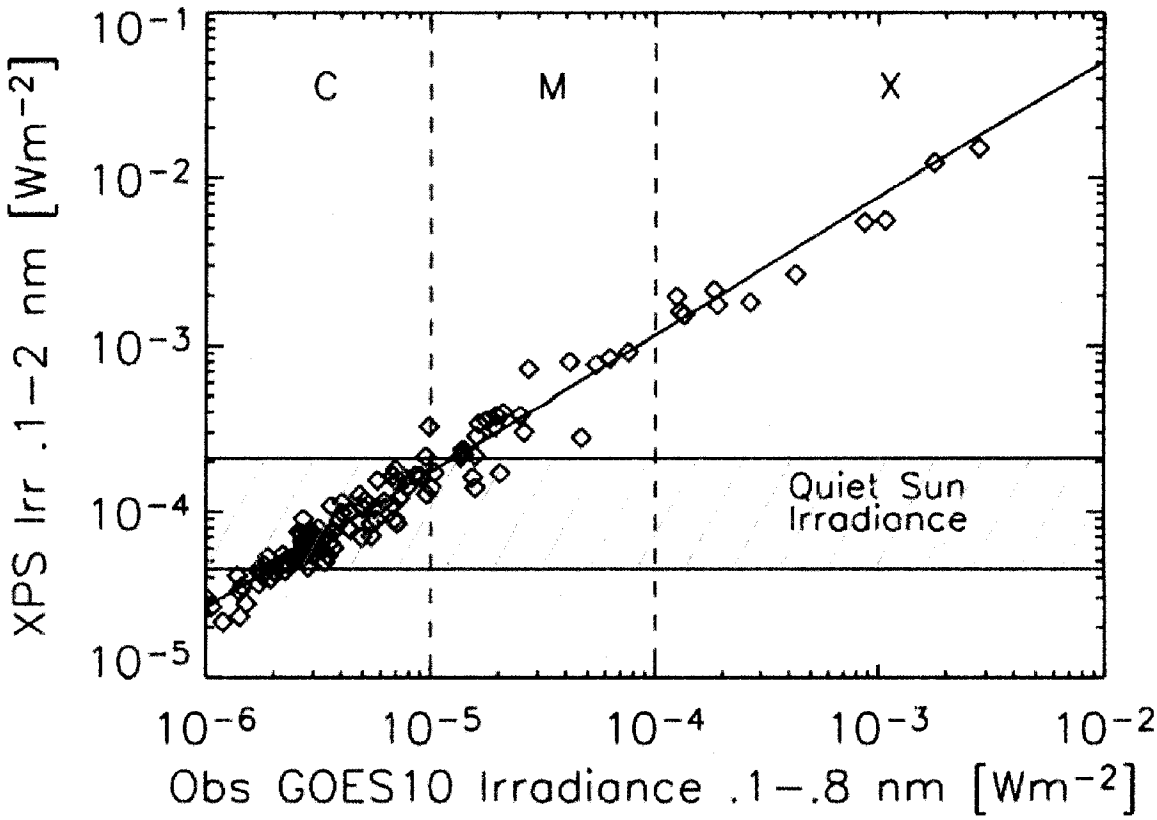

Figure 3.13 XPS irradiance between 0.1-2 nm for the 102 flares observed by all SEE XPS channels and the 16 flares observed by all SORCE XPS channels. The range of quiet-Sun irradiance is represented by grey hash marks. The total 0.1-2 nm irradiance of smaller X-class flares (X1-X5) calculated at the time of the XPS observation provides 7-13 times the energy of the quiet-Sun 0.1-2 nm irradiance, and the total 0.1-2 nm irradiance of larger X-class flares (X5-X30) provides 27-75 times the energy of the quiet-Sun 0.1-2 nm irradiance.